Title

Design of Materials for Energy Conversion, Storage and CO2 Capture

Author

Freyman, Megan

Publication Date

2022

UNIVERSITY OF CALIFRONIA
SANTA CRUZ

Design of Materials for Energy Conversion, Storage and CO_2 Capture

A dissertation submitted in partial satisfaction of
the requirements for the degree of

DOCTOR OF PHILOSOPHY

in

CHEMISTRY

by

Megan C. Freyman

September 2022

The Dissertation of Megan Freyman is approved:

Professor Yat Li, Advisor and Chair

Professor Scott Oliver

Professor Ilan Benjamin

Peter F. Biehl
Vice Provost and Dean of Graduate Studies

Table of Contents

List of Figures

List of Tables

Abstract

Design of Materials for Energy Conversion, Storage and CO_2 Capture

Megan C Freyman

I will discuss the design of functional materials for energy conversion, storage, and CO_2 capture projects. Chapter 1 introduces two different methods, 3D printing and freeze casting, to provide a desired structure to a material. Two different approaches of 3D printing will be explored: stereolithography and direct ink writing. We will also look at freeze casting as a method to introduce a templated structure, based on the formation of ice crystals, to a material. We will then discuss common drying methods coupled with these techniques to preserver the desired structure.

Chapter 2 focuses on the development of a conductive 3D printable living ink containing *Shewanella Oneidensis* MR-1, for use as an organic matter oxidizing anode in a microbial fuel cell to generate bioelectricity. The capability of printing living and functional 3D bacterial structures could open new possibilities in design and fabrication of microbial devices as well as fundamental research on the interactions between different bacterial strains, electrode materials, and surrounding environments.

In the second project shown in Chapter 3, I extend the synthetic capability to the high resolution direct-ink-write printing of resorcinol-formaldehyde based

materials. Highly conductive carbon scaffolds with well-defined porous structures can be derived from these 3D printed polymer materials via a combination of freeze drying and carbonization processes. 3D printed carbon structures can be implemented as a host material for lithium metal for use as an anode in solid-state batteries to improve their cyclability, safety and energy density.

I will present some preliminary results on using cellulose-derived carbon materials for CO_2 capture in Chapter 4. The goal is to improve the understanding of the inherent structure and composition of the cellulose-carbon materials interplay with their CO_2 capture ability. The cellulose material will be used without chemical modifications to the starting cellulose material. CO_2 capture will be achieved through the inherit surface functional groups and structure which can be introduced via freeze casting.

In Chapter 5 I will present an intensive literature review to show the current state of reactive capture technologies. Carbon dioxide (CO_2) capture and CO_2 conversion have traditionally been treated as distinct application areas with non-overlapping research programs. However, the integration of capture and conversion processes presents an opportunity to eliminate energy penalties, costs, and logistical hurdles inherent in the separation of CO_2 from mixed gas streams, regeneration of the capture material/solvent, compression of CO_2, and transport to a conversion facility. By integrating the two processes, which we term "reactive capture", CO_2 can be separated from a mixed gas stream and converted to valuable products using process steps that eliminate sorbent regeneration, CO_2 compression, and transportation.

This dissertation is dedicated to my parents, Jeannine Freyman and Robert Freyman.

For all the love, encouragement, and patience they have given me.

Acknowledgements

I would like to thank my thesis advisor Professor Yat Li. Yat I am very glad I was able to join your lab five years ago. You are a very kind and patient advisor. Thank you for all your guidance during these five years on many different projects. I am sure I will need more advice it in the future.

I would like to thank my dissertation committee Professor Scott Oliver and Professor Ilan Benjamin. Thank you very much for your guanidine during my Ph.D. I would also like to thank Karen Meece for all her help.

I have had the privilege to work about both UCSC and Lawrence Livermore National Lab (LLNL) during my time as a PhD student. I would like to thank my LLNL advisor Dr. Sarah Baker for her words of wisdom and help during my three years at LLNL. I have learned from you how important collaboration is in science. Thank you very much for all the help with the reactive capture perspective and advice and encouragement on other projects. I would like to thank Dr. April Sawvel for helping me keep life in perspective. I would also like to thank Dr. Simon Pang for all his time, help and advice for many things. I would like to thank you for all of your guidance and help on the CO_2 Capture project and the Reactive Capture perspective. Thank you for teaching me how to better communicate my ideas and be a better scientist.

For the work conducted in Chapter 2 I would like to thank my co-author Dr. Tianyi Kou for his help in designing and conducting of the microbial fuel cell experiments. I would like to thank Dr. Shawnwen Wang for his help in writing the paper. I would also like to thank Dr. Ben Abrams for taking SEM images and talking about Husky dogs. I would like to thank Dr. Tom Yuzvinsky for his help designing the experiments for the confocal microscope and the taking of images and reminding me not to have my mood be tied to experiments. I would like to thank Prof. Jin Zhang and his lab for use of the UV-Vis. Thank you for always letting me into your lab!

For the work conducted in Chapter 3 I have many people at LLNL to thank. I would like to thank Dr. Marissa Wood for allowing me to work on the project and advice and help on other projects. Thank you for always taking my phone calls and text message for my endless supply of questions about science and life in general. I would like to thank Dr. Cheng Zhu for all his knowledge about 3D printing of any carbon material under the sun. I would like to thank Dr. Art Nelson for capturing the XPS spectra and for being a wealth of knowledge. I would like to thank everyone else involved with this project at LLNL.

For The work conducted in Chapter 4 on CO_2 capture. I would like to thank Dr. Elwin Hunter-Sellars (I think I spelled your name, right?) for help with BET. I would like to thank Dr. Nathan Ellebracht for all your advice with cellulose.

The work in Chapter 5 on the survey of reactive capture literature is a very collaborative work and I have many people to thank. In addition to Prof. Yat Li, Dr. Sarah Baker, Dr Simon Pang on the LLNL and UCSC side, I would like to thank Dr Eric Duoss of LLNL. I would also like to thank our collaborators at NREL: Dr. Dwarak Ravikumar, Dr. Jenny Huang and Dr. Joshua Schaidle. Thank you, Dr. Joshua Schaidle, also for your kind words of encouragement during my PhD. It was a pleasure to work with you and everyone at NREL and I hope to again in the future. I would also like to thank Jeannette Yusko and Janelle Cataldo of LLNL for their extraordinary work on designing the figures used in this chapter. I would like again thank Jeannette Yusko for all her patients with the back and forth of redesigns on these figures it was always a pleasure to work with you.

I would like to thank my lab mates past and present at UCSC. Tianyi Kou, Bin Yao, Dan Bulmahn thank you very much for all your guidance and welcoming me to the lab. Mingpeng Chen and Shanwen Wang it was a pleasure to go on the PhD journey together thank you for your support. Andre Luiz Martins de Freitas it was a pleasure to get to meet and work with you during your time at UCSC. Dun Lin, Anica Pinongcos, and Ella Davidi I am very glad to have gotten to know you during my time at the lab.

I have many people who have helped and supported me during my PhD. I would like to thank my cohort at UCSC you are all wonderful people, and I am very happy to have had to opportunity to meet and work with you. To the ‘Ladies of the First Floor’ Thank you for everything. Thank you, Anna Johnston, for always letting me stay at your house and hang out in your lab. Thank you, Vivien Cherrette, for calling and talking walks in the woods with me. I would like to thank Jacquie Chisholm for being a friend. I would like to thank Dr. Buddhinie Jayathilake for everything, all your kindness, knowledge and patients. Thank you for always looking out for me. I would like thank Dr. Maira Ceron Hernandez for all her help both in lab and out and advice during these many years, thank you, thank you, thank you. Thank you, Eder Valenzuela, for reminding me to have fun in life. I would like to thank Dr. Swetha Chandrasekaran for all her help and guidance, with a drop of the hat being able to let me know how to fix any synthesis. I would like to thank Dr. Marcus Worsley as well for his help and advice both in science and in cooking. I would like to thank Dr. Fang Qian for all her help and knowledge, you always know the solution to any problem. Dr. Anthony Varni for his encouragement and reminders that it will be okay. Thank you, Mitra Hosseini, as well for your encouragement and advice. I would like to thank Alyssa Troksa, for her help and support both in and out of the lab, always knowing where to find even the most lost item and for great chats. Thank you, Matt Worthington, for keeping me on my toes in the lab and at the climbing gym. Thank you, Tara Ruchonnet, for being a friend in and out of work. Thank you, Cameron Cornell, for starting the journey at LLNL with me. Thank you to Samantha Ruelas for being a calm presence in the lab and talking about Diva Brides. I would like to thank Lisa Palmer for always looking out for me, since I was an intern. I would like to thank Dr. Yong Han for taking a chance on an undergraduate summer intern and introducing me to LLNL, truly thank you Yong. I would like to thank Dr. Jinkyu Han for helping me to become a more independent scientist. I would like to thank Dr. Tijana Grove and her lab at Virginia Tech for allowing me to conducted undergraduate research with them, laying the foundation for the work I am able to do today.

I would like to thank Lucas Jaffe for his support. Thank you for cooking dinner (especially spaghetti). Thank you for always making sure there is dessert even if you can’t eat it. Thank you for always making sure we watch good TV shows. Thank you going on adventures with me. Thank you for being there.

Lastly, I would like to thank my parents, Jeannine Freyman and Robert Freyman. Thank you for always taking my calls even when they are late at night. Thank you for mailing food from Virginia to me. Thank you for always supporting me and telling me when I am making wrong decisions. Thank you for listening to me. Thank you for everything.

This dissertation includes reprints of the previously published material:

Chapter 2:

Megan C Freyman., Tianyi Kou., Shanwen Wang, and Yat Li. **3D printing of living bacteria electrode**. Nano Research. 2020; **13:** 1318-1323.

LLNL-TH-837512

This work was performed under the auspices of the U.S. Department of Energy by Lawrence Livermore National Laboratory under Contract DE-AC52-07NA27344.

1 Introduction

1.1 Designing Materials

When designing a material, it is important to think about the final application the material is being built for. The structure and chemical composition need to be considered, both for how they will influence each other and how they will affect the end goal performance. There is a feedback loop between the material chemical characteristics and structure (**Figure 1.1**). The chemical composition influences the structure and vice-versa. Iterating is a critical part of achieving a goal material. By using these building blocks we can carefully optimize the material for the desired application to further improve technology.

When building a material there are two opportunities to influence the performance: during initial formulation and manipulations after ‘curing’ the final part. The ‘curing steps’ which we are going to focus on for this work are carbonization and ionic crosslinking for curing 3D printed part. We will explore two methods to introduce structure to a material during formulation: templating through freezing and direct ink write 3D printing. We will then look at KOH etching and washing a post carbonized carbon material as a way to introduce further porosity and surface modifications to a material.

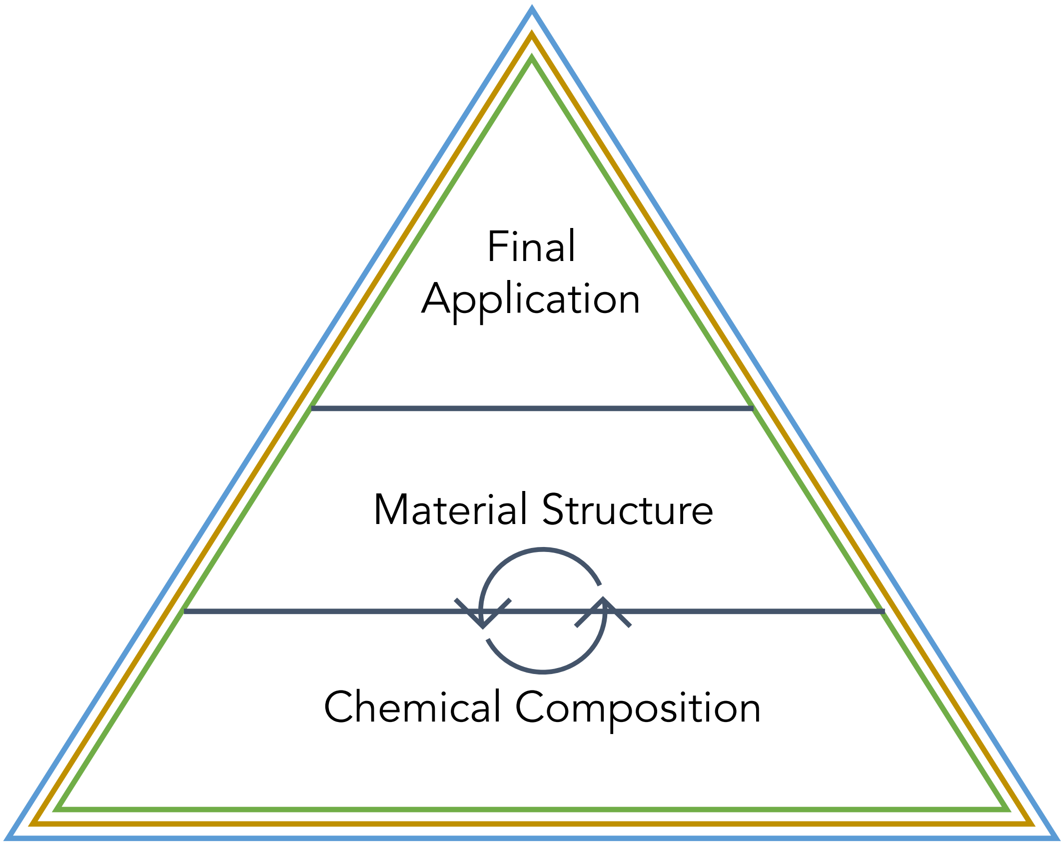

Figure 1.1 Philosophy on Materials Development

1.2 Overview of 3D Printing

Additive manufacturing (AM) or 3D printing is defined as: “the process of joining materials to make objects from 3D model data layer upon layer, as opposed to subtractive manufacturing methodologies, such as traditional machining”[1]. There are many different methods of additive manufacturing or 3D printing each with their own unique features, and material needs. 3D printing has advantages over other manufacturing methods as it reduces waste, and can be used to introduce a desired inherent structure to a finished parts.[2] The designed structure can aid in different functionality of the final part depending on the material the part is made of including (but not limited to): strengthening the final part, and opening up of porosity to help improve diffusion of gas or liquid. During 3D printing the desired part design is first built often using a CAD software. This part is the sliced into layers by software, this sliced file can then be converted to a G-Code file which can be read by the 3D printer. The printer will then build the part layer-by-layer.[3] This process is shown in **Figure 1.2**. This method of building up the part layer by layer is shared by all different methods of 3D printing.

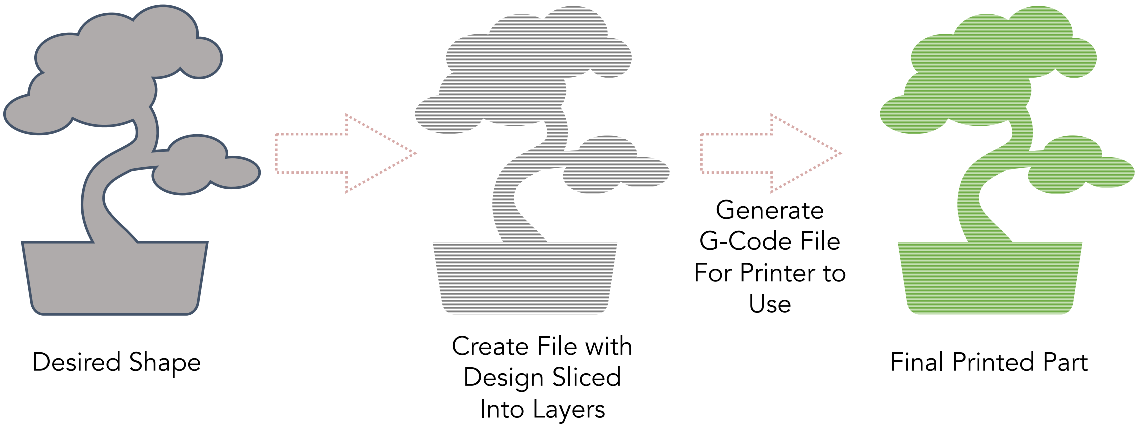

Figure 1.2 Introduction of Part Design to 3D Printer

Figure 1.3, reproduced from Gao et al.[4] shows the different 3D printers and software available at the time the review was written in 2015. This is a very interesting figure as it shows the type of materials which are being used (mainly plastics and metals) by commercial areas. On the left it also shows the timeline of development for these 3D printer devices from 1986 to 2014. It can be seen that initially these machines started out just in industry, then closer to 2014 more machines were devolved for hobbyist users.[4] While 3D printing is not yet used ubiquitously in industry, it is gaining a foothold, Boeing is currently using 3D printed parts inside of their aircraft.[5] With further demonstration of the integrity of printed parts under a variety of conditions and a reformatting of manufacturing process 3D printing is set to find an industrial future. A limiting factor of 3D printing is the time it takes for buildup of layers and limits to size of the build based on machine size constraints. These size constraints can come from the platform on which the material is being built and the range of motion of the print head. The time problem of building layers is at the intersection of the mechanical aspects of the machine and the properties of the material which you are using to build the part. Both are complicated problems to solve to scale up and diversify the uses of 3D printing. 3D printing embodies the philosophy capture in **Figure 1.1**, how the formulation of the ink will affect the functionality of the final part as well as the printing process. In addition, attention needs to be paid to how the structure imparted by 3D printing will affect the final performance of the part.

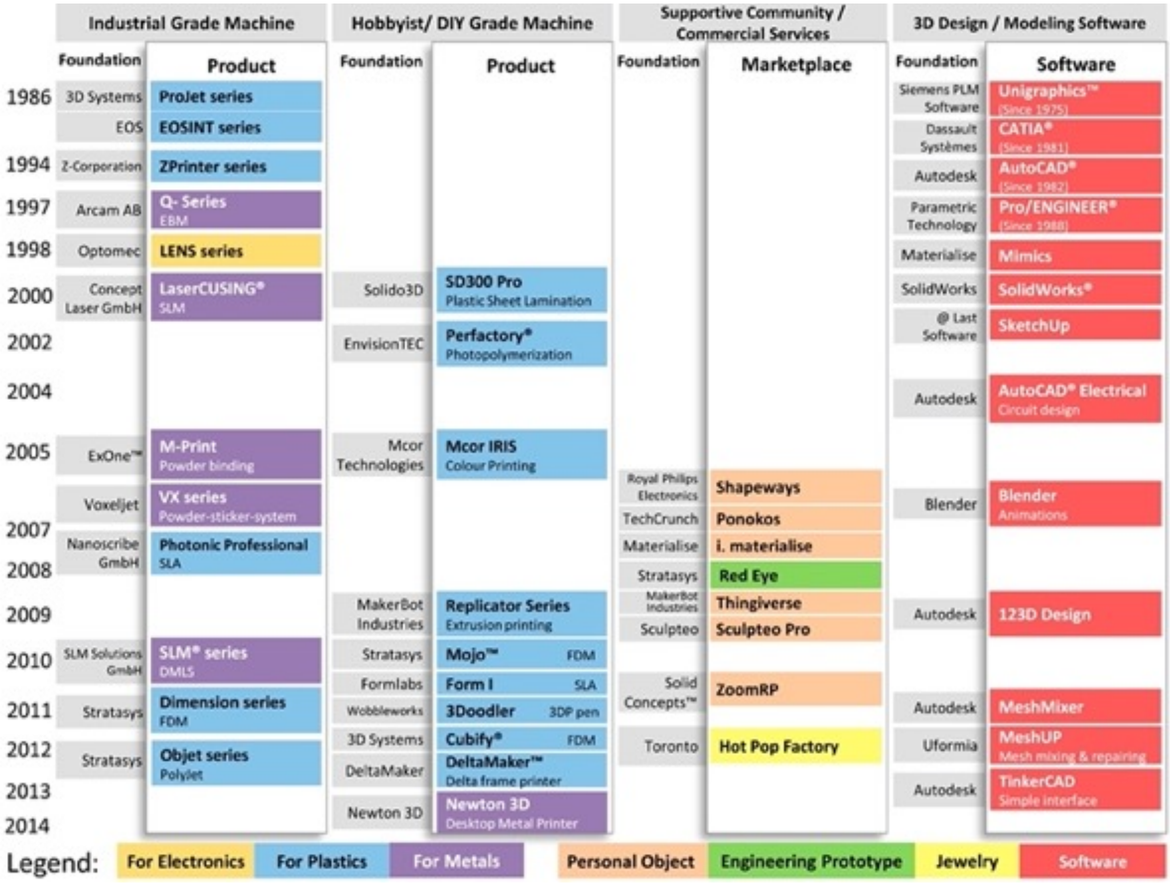

Industrial Grade Machine

Year	Foundation	Product
1986	3D Systems	ProJet series
	EOS	EOSINT series
1994	Z-Corporation	ZPrinter series
1997	Arcam AB	Q- Series EBM
1998	Optomec	LENS series
2000	Concept Laser GmbH	LaserCUSING® SLM
2002		
2004		
2005	ExOne™	M-Print Powder binding
	Voxeljet	VX series Powder-sticker-system
2007 2008	Nanoscribe GmbH	Photonic Professional SLA
2009		
2010	SLM Solutions GmbH	SLM® series DMLS
2011	Stratasys	Dimension series FDM
2012	Stratasys	Objet series PolyJet
2013		
2014		

Hobbyist/ DIY Grade Machine

Foundation	Product
Solido3D	SD300 Pro Plastic Sheet Lamination
EnvisionTEC	Perfactory® Photopolymerization
Mcor Technologies	Mcor IRIS Colour Printing
MakerBot Industries	Replicator Series Extrusion printing
Stratasys	Mojo™ FDM
Formlabs	Form I SLA
Wobbleworks	3Doodler 3DP pen
3D Systems	Cubify® FDM
DeltaMaker	DeltaMaker™ Delta frame printer
Newton 3D	Newton 3D Desktop Metal Printer

Supportive Community / Commercial Services

Foundation	Marketplace
Royal Philips Electronics	Shapeways
TechCrunch	Ponokos
Materialise	i. materialise
Stratasys	Red Eye
MakerBot Industries	Thingiverse
Sculpteo	Sculpteo Pro
Solid Concepts™	ZoomRP
Toronto	Hot Pop Factory

3D Design / Modeling Software

Foundation	Software
Siemens PLM Software	Unigraphics™ (Since 1975)
Dassault Systèmes	CATIA® (Since 1981)
Autodesk	AutoCAD® (Since 1982)
Parametric Technology	Pro/ENGINEER® (Since 1988)
Materialise	Mimics
SolidWorks	SolidWorks®
@ Last Software	SketchUp
Autodesk	AutoCAD® Electrical Circuit design
Blender	Blender Animations
Autodesk	123D Design
Autodesk	MeshMixer
Uformia	MeshUP Mesh mixing & repairing
Autodesk	TinkerCAD Simple interface

Legend: For Electronics | For Plastics | For Metals | Personal Object | Engineering Prototype | Jewelry | Software

Figure 1.3 Figure Showing the different Scale and Methods of 3D Printers and Software. Reproduced With Permission Copyright 2015, Elsevier [4]

1.2.1 Types of 3D Printing

There are currently many different types of the 3D printing in use today, spanning a diverse range of feature sizes from nanometer to construction scale parts.[6,7] There are two general methods for how 3D printing can build up layers: through the melting or joining material together to generate the layers, or through curing of a soft or liquid material to build the part.[8] I would like to focus on two techniques, stereolithography, which cures photosensitive resin to build up layers and direct ink write printing, which builds up layers of curable ink.

1.3 Stereolithography Printing

Stereolithography printing emerged in the 1980's and is one of the oldest forms of 3D printing. **Figure 1.4** shows the simplified diagram of how stereolithography printing works. A Ultra-Violet (UV) light source is used to selectively cure a photosensitive resin.[9]

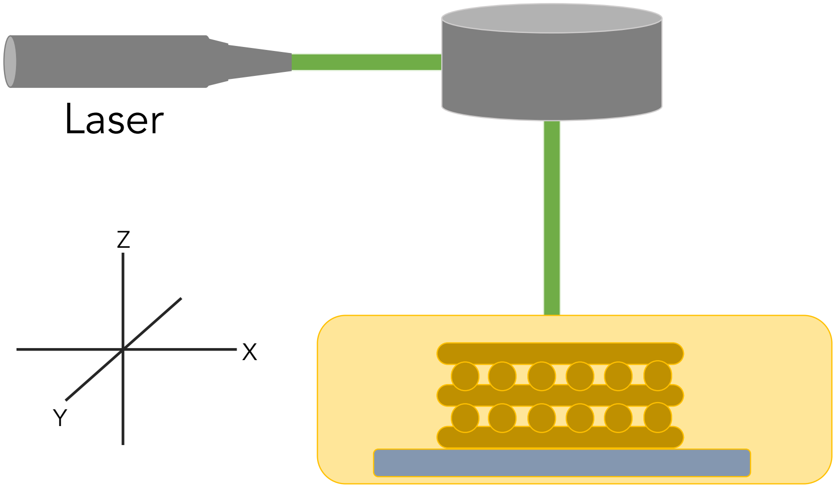

Figure 1.4 Simplified Diagram of Stereolithography Printing System

Huang et al. has discussed four different types of stereolithography, shown in Error! Reference source not found., these categories are: scanning, projection, continuous, and volumetric.[9]

In the scanning method a laser beam is scanned over the resin bath, curing the resin as it moves. The laser can move in the X-Y direction while the stage (holding the resin bath) moves in the Z-Direction. This method however can introduce optical distortion to the beam and effect the final printed part. Different methods were introduced which have a fixed beam while the stage (and the resin bath) move in the X,Y and Z direction, helping to solve the optical distortion problem.[9] Standard scanning stereolithography methods utilize one laser, however a second scanning technique called two-photon polymerization exists which can be used to achieve sub 100 nm resolution. High resolution is achieved through using two femtosecond lasers which can produce very narrow feature sizes.[9,10] This technique has been demonstrated to produce parts at the nanometer feature scale with applications in a variety of fields such as: microoptics, electronics and biomedical.[10]

Projection stereolithography utilizes masks to project images onto a layer of curable resin, forming the desired shape/pattern, another layer of curable resin is introduced and cured using the desired mask. Following the diagram presented in **Figure 1.4** the mask would be projected onto the print stage/resin layer which would then move in the Z-direction. This allows for a full layer of the part to be cured at once. However it is time intensive to utilize these masks to build up these layers (Error! R eference source not found.).[9] Projection micro stereolithography (PμSL) is an attractive projection technique which can produce parts with resolution between 0.6 μm and 30 μm. This technique utilizes a digital micromirror device (DMD) to project the masks on to the resin. This technique has be used to produce complicated microstructures with a variety of materials, with applications in biomedical, optical, aerospace and robotics industries.[11]

Continuous stereolithography is like projection stereolithography except the interface between resin and light source is through some type of glass or oxygen permeable window at the bottom of the resin tank, rather than at the air-resin interface, at the top of the resin tank. Subsequently the projected image is through the bottom of the resin tank (in the Z-direction) the stage/build platform is above the resin tank and will be lowered in the Z-direction where the image will be projected at this window-resin interface. As the part is built and cured the build platform will raise up (Z-direction) and out of the resin tank. In this process as photopolymerization is prevented between the window and the resin by creating an ‘oxygen-containing dead zone’.[9] This method has the ability to decrease the print time necessary compared to standard projection stereolithography (Error! Reference source not found.).

A very exciting recent development is volumetric printing. In this method, 2D images are projected onto a photosensitive resin from multiple angles, when these images intersect, they form a 3D image and cure the resin. This method does not require a stage or supports and produces a fully formed part in-situ in the viscous resin bath. [12] This method has the potential to have orders of magnitude faster manufacturing time (Error! Reference source not found.).[9,12]

Table 1.1 Four different methods of Stereolithography Printing and Their Corresponding Parameters. Reproduced form Huang et al.[9]

Stereolithography	Printing Speed	System Resolution	Printable Size	Light source
Scanning	Scanning speed: hundreds to thousands of millimeters per second	A few microns (~100 nm for 2PP system)	From tens to hundreds of millimeters	UV light (Fs laser source for 2PP)
Projection	Tens of millimeters per hour	A few microns (typically greater than 5 microns)	Tens of millimeters	UV/Visible light
Continuous	Hundreds of millimeters per hour	A few microns (typically greater than 5 microns)	Tens of millimeters Tens of millimeters	UV/Visible light
Volumetric	Greater the 10^5 mm^3 per hour	80 ~ 300 microns	From tens to hundreds of millimeters	UV light

Stereolithography printing has specific requirements for feedstock materials to ensure the achievement of a final 3D printed part with the desired functionality. Prints are subject to defects such as steps forming in the surface of the part as a result of layer build up and distortion or merging of desired features. Parameters of a desirable resin feedstock include: (1) The part must be able to photopolymerized at the desired wavelength needed for the stereolithography printer, following a desirable polymerization rate to achieve a good resolution print. (2) Any component which is added to the polymer resin must not disrupt the light source and effect the curing. (3)

The resin must have a desirable viscosity to produce a clean print. (4) After printing most materials will need to be post cured to produce a final part with the desired functionality. It is important that the resin used does not suffer from further distortion (such as shrinkage or warping) during the final processing or curing method. [13]

1.4 Direct Ink Write (DIW) Printing

DIW is a 3D printing method which can use a wide variety of materials. If the material is flowable and curable it is likely that it can be printed.[14] The principle of generating the part is still the same, a design is created and converted to G-Code (**Figure 1.2**) then using the printer is built layer by layer to a finished part. In a DIW printer system the print platform can be fixed and the print head moves in X,Y and Z directions to build the part, or the stage and the print head can both move in X,Y and Z directions. **Figure 1.5a** shows a simplified schematic of a DIW system. Fundamentally DIW printers are very similar, what gives them their versatility is the ability for the end user to build highly customizable inks which using DIW printing can be endowed with a desirable architecture. DIW printing normally gives feature sizes, on the order of millimeter to micron, the feature size is a direct result of the size of nozzle through which the ink can be successfully extruded.[14] DIW methods have the ability to print multiple materials in the same part. Multimaterial printing can be achieved through printing of material with separate print head for each ink or a print head which has incorporated microfluidic devices to achieve a core shell design.[15] **Figure 1.5b** shows different methods for which the ink can be extruded in a DIW device, pneumatic pressure, piston, and screw.[16]

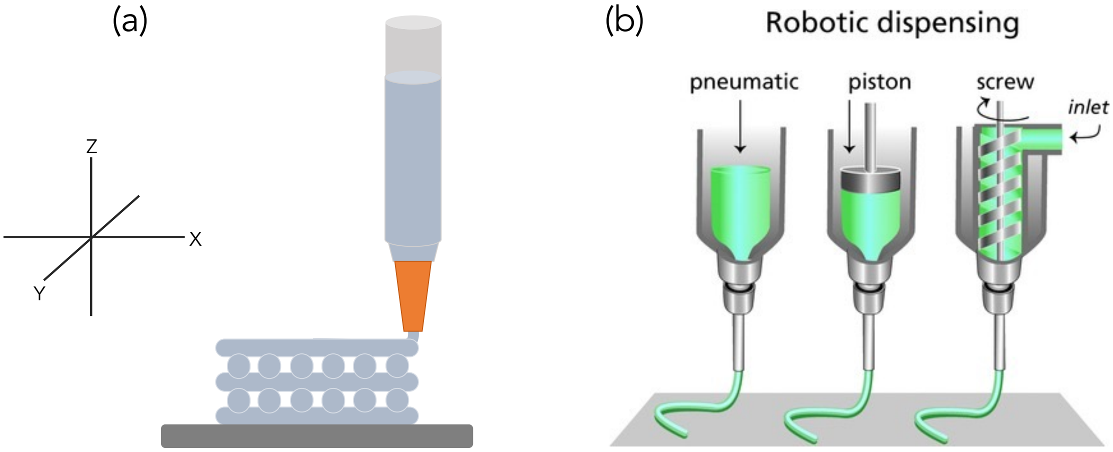

Figure 1.5 Simplified Schematic of DIW 3D Printing. (a) schematic of printing part. (b) Schematic of different extrusion methods. Reproduced With Permission Copywrite John Wiley and Sons 2013.[16]

Because of the variety of different types of ink which can be printed DIW printing can be applied to many different fields. I would like to focus on their application in two different fields: energy storage, and printing of living microbes.

1.5 DIW Printing of Energy Storage Materials

3D printing has been demonstrated for printing of cathodes, anodes and solid electrolyte in battery and energy storage devices.[17] In addition to ink jet printing, the DIW technique is the most widely used technique when applied to energy storage devices due to the wide range of inks which can be used.[18] The structural control provided by DIW printing allows for tuning of porosity which can improve the ionic diffusion, optimize the energy and power density.[17,19] There are some drawbacks to 3D printing of energy storage device materials. The layer by layer building of the part and in the introduction of further porosity can decrease the mechanical strength compared to a part which is manufactured using traditional methods.[18] In addition any material not only must perform as desired for the energy storage application but must also be able to be printed. This can lead to a delicate balance between maintaining the desired functionality of the material and introducing other components, such as viscosifiers to improve printability, which may decrease conductivity or effectively dilute the active component of the ink. The most common way for DIW to be implemented in an energy storage device is the through the printing of an electrode. There are a wide variety of inks demonstrated in literature[18,19] Most commonly a conductive carbon additive is used, in addition to the desired metal, such as $Li_4Ti_5O_{12}$ for lithium-ion batteries, additional additives such as Pluronic F127 or cellulose can be added to aid printability, the ratio of these components can be tuned with the solvent to perfect the printability of the ink. Post processing, such as carbonization, or UV-curing, will be dependent on the ink formulation and the desired final performance of the printed part. [18,19]

1.6 DIW for Printing Living Materials

The ability to directly print living microorganisms in a living bioink, has applications in a wide variety of fields: including medical, bioremediation, bioenergy and bioproduction of desirable materials. It is desirable to be able to embed living cells or microbes into a matrix to help provide protective environment, and a method of immobilization. DIW 3D printing can also help create distinct distributions of the living microbe or cells inside the of the living part.[20,21] The ability to concentrate functional cells or microbes into a substrate allows for the harnessing of the living cell or microbes innate ability and a way to couple different types of microbes together to achieve a dual functional device.[20] When building a living ink for DIW printing, not only must the printability be considered but the survivability of the living microbe or cell. The living microbe or cell must be compatible with the ink components, and the method used to cure the printed ink must maintain the vitality of the living component. Common materials used to generate living inks include: agarose solution, Pluronic F-127, hyaluronic acid and κ-carrageenan, alginate, nanocellulose and polyethylene glycol diacrylate (PEGDA).[22] Microalgae has been embedded in an alginate, methyl cellulose ink for use as a way to generate oxygen in medical applications. Biophotovoltaics were generated through the incorporation of cyanobacteria in a ink based with bionic mushroom, polysiloxane, graphene nanoribbon based ink.[20]

1.7 Freeze Casting

Another method to introduce internal structure is through freeze casting. In freeze casting a desired component is incorporated into a solvent, liquid or in a gel, this is then introduced to a cold plate or fully submerged in a cold component like liquid nitrogen. Through freezing of the solvent or surrounding gel an ice template is introduced. The frozen solvent commonly removed through sublimation. **Figure 1.6** is reproduced from Gurlo *et al.*, shows a schematic of the freeze casting process and outlines the current progress in freeze casting, showing materials used, different pore structures which can be formed and then final applications.[23] After removing the frozen solvent the desired templated material is left behind for post processing.[23-25] A variety of materials have been templated using freeze casting including: ceramics, polymers, biomacromolecules, metals and carbon nanomaterials.[23] During freeze casting intrinsic and extrinsic methods can be used to modify the pore structure. Intrinsic modifications are through adding something to the freezing matrix which will manipulate the pore formation. This can be done through secondary additives, manipulation of the starting particle size, and the concentration of the desired material in the solution.[26] Extrinsic modification methods are through the application of an external force to the freezing matrix.[25]

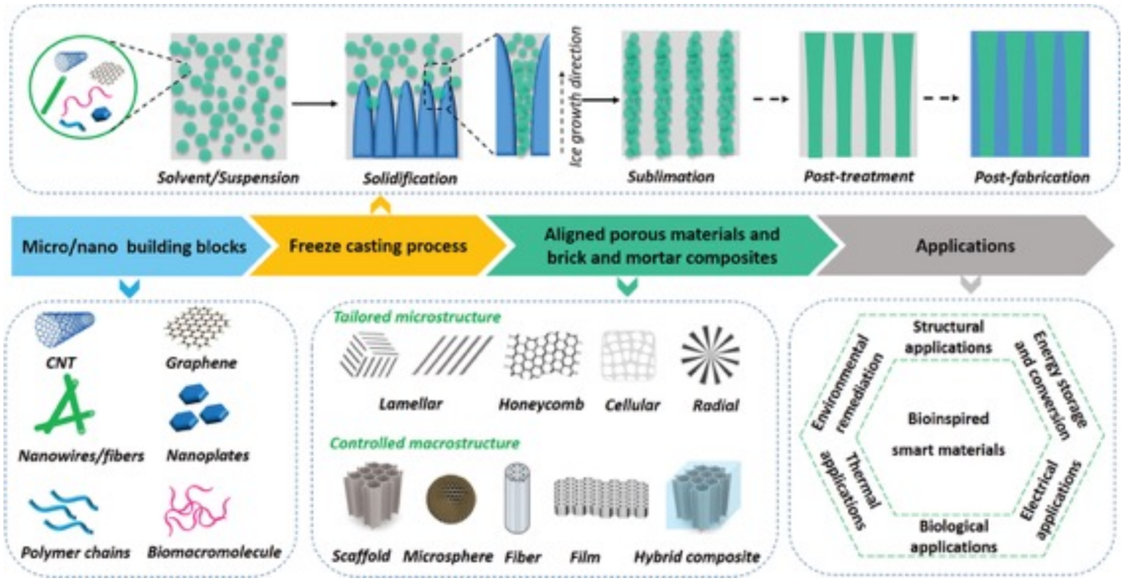

Figure 1.6 Overview of Freeze Casting Process from Starting Material to Final Application. Reproduced With Permission Copyright John Wiley and Sons 2020. [23]

1.8 Drying Methods

There are three major methods to remove solvent from a final 3D printed or freeze-dried part: super critical drying, freeze drying or ambient air drying. Super critical dying is not as suited to freeze dried parts as component to be dried must be in a liquid solvent. In supercritical drying a solvent is chosen which is miscible with a liquid gas, a common combination is acetone and liquid CO_2. The acetone is replaced with liquid CO_2 at low temperature. The temperature is then ramped under pressure transition the liquid CO_2 to gas, after which the gaseous CO_2 is vented. This method for extraction of the solvents mitigates the formation of capillary interactions during drying, helping to preserve the structural integrity of the material.[27] In freeze dying, a frozen solvent is removed from the part through sublimation, also preventing pore collapse due to a lack of capillary forces. This method is well suited for freeze casted parts. In ambient air drying the part is left exposed to the atmosphere for the solvent to be removed. This method is cheaper as it does not require any specialized equipment. However, there is a risk of pore collapse during the drying process. To slow the drying speed a solvent with a higher vapor pressure can be used, or a humid environment can be maintained around the part. [27]

1.9 References

1. Technologies, A.C.F.o.A.M., and Terminology, A.C.F.o.A.M.T.S.F.o. 2012; **Standard terminology for additive manufacturing technologies**, (Astm International).
2. Ngo, T.D., Kashani, A., Imbalzano, G., Nguyen, K.T.Q., and Hui, D. **Additive manufacturing (3D printing): A review of materials, methods, applications and challenges**. Composites Part B: Engineering. 2018; **143:** 172-196.
3. Bhuvanesh Kumar, M., and Sathiya, P. **Methods and materials for additive manufacturing: A critical review on advancements and challenges**. Thin-Walled Structures. 2021; **159:** 107228.
4. Gao, W., Zhang, Y., Ramanujan, D., Ramani, K., Chen, Y., Williams, C.B., Wang, C.C.L., Shin, Y.C., Zhang, S., and Zavattieri, P.D. **The status, challenges, and future of additive manufacturing in engineering**. Computer-Aided Design. 2015; **69:** 65-89.

5. Najmon, J.C., Raeisi, S., and Tovar, A. 2019; **2 - Review of additive manufacturing technologies and applications in the aerospace industry**. In Additive Manufacturing for the Aerospace Industry, F. Froes and R. Boyer, eds. (Elsevier), pp. 7-31.

6. Lim, S., Buswell, R.A., Le, T.T., Austin, S.A., Gibb, A.G.F., and Thorpe, T. **Developments in construction-scale additive manufacturing processes**. Automation in Construction. 2012; **21:** 262-268.

7. Behera, D., Chizari, S., Shaw, L.A., Porter, M., Hensleigh, R., Xu, Z., Zheng, X., Connolly, L.G., Roy, N.K., Panas, R.M., et al. **Current challenges and potential directions towards precision microscale additive manufacturing – Part IV: Future perspectives**. Precision Engineering. 2021; **68:** 197-205.

8. Bikas, H., Stavropoulos, P., and Chryssolouris, G. **Additive manufacturing methods and modelling approaches: a critical review**. The International Journal of Advanced Manufacturing Technology. 2016; **83:** 389-405.

9. Huang, J., Qin, Q., and Wang, J. **A Review of Stereolithography: Processes and Systems**. Processes. 2020; **8:** 1138.

10. Zhou, X., Hou, Y., and Lin, J. **A review on the processing accuracy of two-photon polymerization**. AIP Advances. 2015; **5:** 030701.

11. Ge, Q., Li, Z., Wang, Z., Kowsari, K., Zhang, W., He, X., Zhou, J., and Fang, N.X. **Projection micro stereolithography based 3D printing and its applications**. International Journal of Extreme Manufacturing. 2020; **2:** 022004.

12. Kelly, B.E., Bhattacharya, I., Heidari, H., Shusteff, M., Spadaccini, C.M., and Taylor, H.K. **Volumetric additive manufacturing via tomographic reconstruction**. Science. 2019; **363:** 1075-1079.

13. Manapat, J.Z., Chen, Q., Ye, P., and Advincula, R.C. **3D Printing of Polymer Nanocomposites via Stereolithography**. Macromolecular Materials and Engineering. 2017; **302:** 1600553.

14. Saadi, M.A.S.R., Maguire, A., Pottackal, N.T., Thakur, M.S.H., Ikram, M.M., Hart, A.J., Ajayan, P.M., and Rahman, M.M. **Direct Ink Writing: A 3D Printing Technology for Diverse Materials**. Advanced Materials. **n/a:** 2108855.

15. Truby, R.L., and Lewis, J.A. **Printing soft matter in three dimensions**. Nature. 2016; **540:** 371-378.

16. Malda, J., Visser, J., Melchels, F.P., Jüngst, T., Hennink, W.E., Dhert, W.J.A., Groll, J., and Hutmacher, D.W. **25th Anniversary Article: Engineering Hydrogels for Biofabrication**. Advanced Materials. 2013; **25:** 5011-5028.

17. Zeng, L., Li, P., Yao, Y., Niu, B., Niu, S., and Xu, B. **Recent progresses of 3D printing technologies for structural energy storage devices**. Materials Today Nano. 2020; **12:** 100094.

18. Chang, P., Mei, H., Zhou, S., Dassios, K.G., and Cheng, L. **3D printed electrochemical energy storage devices**. Journal of Materials Chemistry A. 2019; **7:** 4230-4258.

19. Zhang, F., Wei, M., Viswanathan, V.V., Swart, B., Shao, Y., Wu, G., and Zhou, C. **3D printing technologies for electrochemical energy storage**. Nano Energy. 2017; **40:** 418-431.

20. Wangpraseurt, D., You, S., Sun, Y., and Chen, S. **Biomimetic 3D living materials powered by microorganisms**. Trends in Biotechnology. 2022; **40:** 843-857.

21. Schaffner, M., Rühs, P.A., Coulter, F., Kilcher, S., and Studart, A.R. **3D printing of bacteria into functional complex materials**. Science Advances. 2017; **3:** eaao6804.

22. Rodrigo-Navarro, A., Sankaran, S., Dalby, M.J., del Campo, A., and Salmeron-Sanchez, M. **Engineered living biomaterials**. Nature Reviews Materials. 2021; **6:** 1175-1190.

23. Shao, G., Hanaor, D.A.H., Shen, X., and Gurlo, A. **Freeze Casting: From Low-Dimensional Building Blocks to Aligned Porous Structures—A Review of Novel Materials, Methods, and Applications**. Advanced Materials. 2020; **32:** 1907176.

24. Liao, W., Zhao, H.-B., Liu, Z., Xu, S., and Wang, Y.-Z. **On controlling aerogel microstructure by freeze casting**. Composites Part B: Engineering. 2019; **173:** 107036.

25. Nelson, I., and Naleway, S.E. **Intrinsic and extrinsic control of freeze casting**. Journal of Materials Research and Technology. 2019; **8:** 2372-2385.

26. Li, W.L., Lu, K., and Walz, J.Y. **Freeze casting of porous materials: review of critical factors in microstructure evolution**. International Materials Reviews. 2012; **57:** 37-60.

27. Wang, Z., Tian, M., Yu, J., Jiao, J., Yang, C., Pei, L., Yan, C., and Fang, C. **Recent advances of 3D compressible carbon assemblies: A review of synthesis, properties and applications in energy and environment**. Journal of Environmental Chemical Engineering. 2021; **9:** 106269.

2 3D Printing of Living MFC Anode

2.1 Abstract

The capability of preparing 3D printable living inks provides a unique way to harness the activity of microbes and use them in functional devices. Here we demonstrate the incorporation of the living bacteria Shewanella Oneidensis MR-1 (S. Oneidensis MR-1) directly into an ink used for creating 3D printed structures. Significantly, S. Oneidensis MR-1 survives the 3D printing process by showing prominent activity in degrading the methyl orange azo dye. Through the addition of carbon black to this ink, we further demonstrate the direct printing of a living microbial fuel cell (MFC) anode. To our knowledge, this is the first report on implementing 3D printed bacteria structure as a living electrode for an MFC system. The capability of printing living and functional 3D bacterial structure could open up new possibilities in design and fabrication of microbial devices as well as fundamental research on the interaction between different bacterial strains, electrode materials, and surrounding environments.

2.2 Introduction

A diverse range of bacteria can utilize electricity to generate valuable products or treat pollutants. For example, fermentation with lactic acid-producing bacteria is a desired method to commercially produce lactic acid.[1] Methanotrophic bacteria can be harnessed to convert methane to valuable products, such as bioplastics.[2] Sulfate-reducing bacteria (SRB) have been used to treat sulfate containing wastewater from industries such as mining, textiles, and tanneries.[3,4] Fe(III) reducing microbe, strain GS-15, were found to reduce uranium (VI) to insoluble uranium (VI) helping to sequester its sediment.[5] Among them, *S. Oneidensis* MR-1 is one of the most widely studied bacteria strains. It is most well-known for its capability of treating wastewater by oxidizing organic pollutants, the electrons produced from this process are then display on the outer surface of the bacteria cell.[6] These electrons can be directly used for reduction reactions such as reducing graphene oxides to graphene.[7] When *S. Oneidensis* MR-1 are contacted with an electrode in a microbial fuel cell, these electrons can be collected for generating bioelectricity. Furthermore, it can couple with a photoelectrode [8] or photoelectrochemical system to generate not only bioelectricity but also chemical fuels.[9-11] These electro-microbiological reactions occur at the surface interface between bacteria, electrode, and surrounding solution.[12] Increasing the interfacial area of the electrode is favorable for boosting the performance of the desired bacteria.[8,13]

Recently, a 3D printing technique, namely direct ink writing (DIW), has been used to engineer 3D structures with bacteria. For example, Lehner *et al.* reported a facile and gentle printing of living E. coli bacteria directly embedded in an alginate-based hydrogel as a demonstration of printing living materials.[14] Qian *et al.* reported a novel method to produce a living bioink, using freeze-dried yeast cells, to help concentrate cells in the 3D printed structure, achieving a record high cell density.[15]

When preparing the ink for printing of the living cells we had to focus on the curing method for the final part. Common methods for curing DIW printed parts include change in pH to promote catalyzed crosslinking,[16] UV light curing of a photo sensitive crosslinker[17] and drying to remove solvent to create a stable final part,[18] and ionic cross linking through the exchange of a monovalent ion for a divalent ion.[19] *S. Oneidensis* MR-1 thrives in a neutral pH range, a strong change in pH to catalyze a printed ink to crosslink would kill the microbe. High energy light from UV curing of a photo sensitive crosslinker would also kill the microbe, and the removal of solvent to dry a printed part would desiccate the microbe again resulting in death. We chose to use an alginate ink which has a gentle ionic curing method which can be done at neutral pH, without the need for UV light, or drying to remove excesses solvent. For the alginate crosslinking is achieved using calcium salt which displaces sodium in the alginate which then links the two polymer segments together at negative COO^- groups.[14]

In this work, using DIW we aim to create a 3D porous bioelectrode, with good control of its geometry, porosity, and dimensions, to enable efficient mass transport of culture medium/electrolyte and/or the synthesized products, using *S. Oneidensis* MR-1 as a model bacteria for this system. Significantly, using a living electrical conducting ink, we demonstrate, for the first time, a 3D printed bacteria structure which can be used as a living anode for MFC. Electrochemical measurements revealed that there is a good charge transfer between the *S. Oneidensis* MR-1 and the electrode surface.

Long-term operation of the MFC device showed stable current generation up to at least 93 hrs.

2.3 Experimental

2.3.1 Bacteria Culture

Tryptic soy broth (TSB) growth media was inoculated with *S. Oneidensis* MR-1. It was allowed to grow for 24 hrs aerobically in a shaking 25 °C water bath. Before use all growth flasks and media were sterilized in an autoclave at 250 °C for 30 mins.

2.3.2 Bacteria Ink Preparation and Printing

Bacteria growth solution (10 mL) was mixed with of sodium alginate (1 g), and of sigma cellulose (3 g). The solids were mixed together first before the addition of the TSB culture. The mixing beaker was sterilized using 70% ethanol solution and by flame. This mixture was then put into a 5 mL sterile syringe and loaded into a 3D printer. The print stage was cleaned with 70% ethanol solution before printing. The 3D structures were printed using 0.016” printing tips at a write speed of 250 mm/min. The final printed part was 20 x 20 mm and 2 mm in height. The final filament was approximately 0.5 mm thick with about 1 mm spacing between filaments. The printed parts were cured by dropping CaCl2 • $2H_2O$ (0.88 M) solution directly onto the printed part and allowing it to sit for 10 mins.

2.3.3 Methyl Orange Degradation Experiment

The 3D printed bacteria structure was placed in a 100 mL beaker, sterilized using 70% ethanol and by flame, with a 1:1 volume ratio of Methyl Orange (MO) dye solution and sterile lysogeny broth (LB) growth media for a total of 10 mL. Every 2 h a 1.5 mL sample was taken from the beaker and centrifuged at 8,000 rpm for 10 mins on an Eppendorf 5415C Centrifuge. UV-Vis measurements were then taken from the samples at a scan rate of 4800 nm/min from 800 to 200 nm. After 8 h (1 cycle), the 3D printed bacteria structure was washed with sterile LB Media and then placed in a fresh MO-LB mixture solution. This process was repeated for 4 cycles.

2.3.4 Preparation and Printing of MFC Living Anode

MFC living anode ink was prepared by mixing of sodium alginate (0.039 g), sigma cellulose (0.108 g), acetylene carbon black (0.418 g) and TSB *S. Oneidensis* MR-1 growth solution (5 mL) (see bacteria culture section). All dry ingredients were mixed before the addition of TSB growth solution. This mixture was then put into a sterile 5 mL syringe and loaded into a 3D printer. The print stage was cleaned with 70% ethanol solution before printing. The 3D structures were printed using 0.033" printing tips at a write speed of 70 mm/min, the printed parts were allowed to sit in the $CaCl_2 \cdot 2H_2O$ (0.88 M) solution for 20 mins. The cured printed part is 2 x 2 cm and 2 mm in height, the filament thickness is approximately 0.8 mm and again 1 mm apart. A solid block living anode was made as a control sample using the same ink formulation and curing procedure as the 3D printed living anode. The ink was spread into a 2.2 x 2.2 cm square that was 5 mm thick, the anode was then cured using $CaCl_2$ • $2H_2O$ (0.88 M). The cell density used of the growth solution used to make the solid anode was similar to that of used to make the 3D printed structures.

2.3.5 MFC Measurements

A living anode was fabricated by attaching a platinum wire to the 3D printed bacteria structure. This electrode was then placed into a two-chamber MFC device outfitted with a cation exchange membrane and a carbon cloth cathode. The anode chamber was sterilized using 70% ethanol solution before use. The 9 ml anode chamber was filled with LB broth growth media, the 9 ml cathode chamber was filled with 0.05 M ferricyanide in phosphate buffer (K_2HPO_4 18.2 g L^{-1}, KH_2PO_4 2.56 g L^{-1}, $K_3Fe(CN)_6$ 15.6 g L^{-1}). LB broth growth media was used instead of TSB broth because the phosphate salt present in TSB growth solution could pull the calcium out of the printed part used for curing, adversely affecting the stability of the 3D printed structure. The power density measurements were performed by attaching the MFC device to the following resistors: 1 MΩ, 510 kΩ, 180 kΩ, 82 kΩ, 51 kΩ, 20 kΩ, 10 kΩ, 5.1 kΩ, 3.9 kΩ, 1 kΩ, 0.5 kΩ, 0.2 kΩ, 0.05 kΩ. The MFC device remained attached to the resistor until the voltage stabilized, a pseudo staircase pattern was produced. The power density was the calculated at each resistor. Electrochemical impedance data was collected using electrochemical workstation (CHI 660D) in a two-electrode configuration with frequency range from 100 kHz to 0.1 Hz at zero potential with a perturbation of 5 mV.

2.3.6 MFC Stability Test

An MFC device was connected to the resistor which corresponds to the peak power density, and the device current was monitored as a function of time. When the device current dropped almost to the baseline and the ferricyanide solution in the cathode chamber became colorless, the LB broth and 0.05 M ferricyanide in phosphate buffer solutions in the anode and cathode chambers respectively were replaced with new solution. This was continued for 5 cycles over a 93 hr period.

2.3.7 Materials Characterization

Confocal microscopy images (Leica SP5 Confocal Microscope) were collected for the 3D printed bacteria structures stained with Live/Dead BacLight Bacterial Viability dye (Thermo Fisher Scientific). Scanning electron microscopy (SEM) images were collected for the 3D printed bacteria structures/anodes using a Hitachi S-4800 II SEM. The parts were printed using a Hyrel 30M printer. UV-Vis measurements were carried out on an Agilent Technologies Cary 60 UV-Vis Spectrometer.

2.4 Shewanella Oneidensis MR-1 Vitality Characterization

Error! Reference source not found. shows the final 3D printed living structure. Error! Reference source not found.**a-b** show confocal microscope images from the edge o f the 3D printed living structure, with fluorescence on and off respectively. Green fluorescence is attributed to living *S. Onediensis* MR-1 with intact membranes while red/orange color is attributed to *S. Onediensis* MR-1 with broken membranes.[20]

Background fluorescence seen in Error! Reference source not found.**b** is attributed to the TSB growth solution used in the cultivation of the *S. Onedensis* MR-1. The confocal microscope images give a good indication that the *S.* Onedensis MR-1 survives the 3D printing processes. The lower images, Error! Reference source not found.**c-e** qualitatively demonstrate the mechanical stability of the living 3D printed lattice.

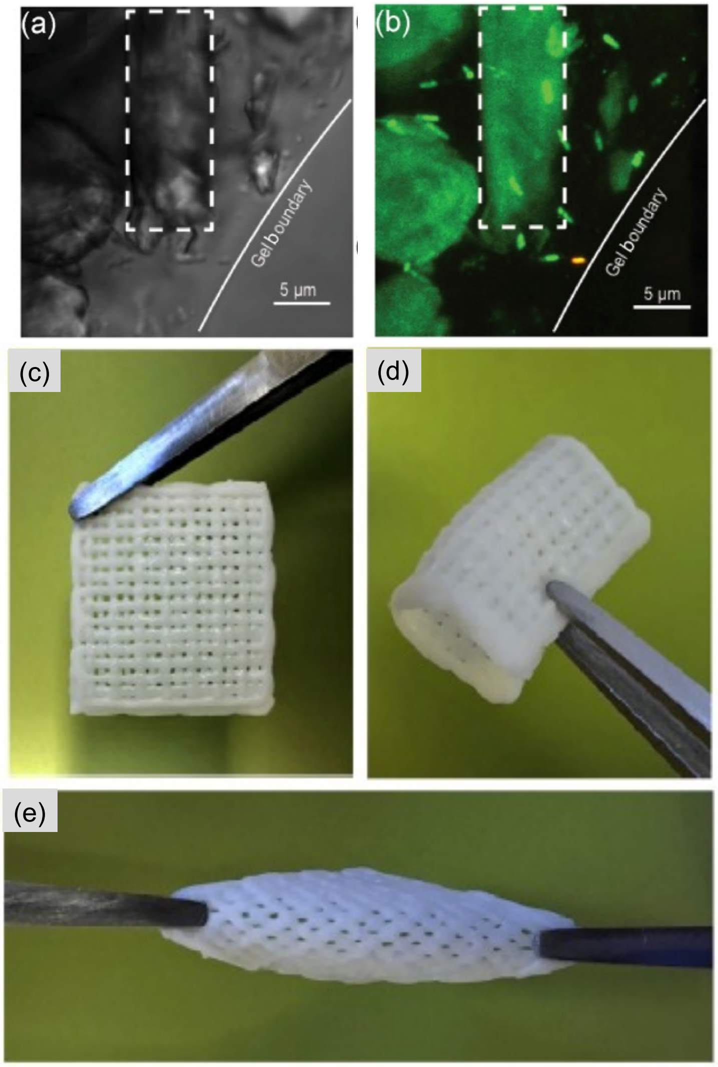

Figure 2.1 Shows the vitality of the microbes and qualitative structural characterization.(a) – (b) confocal microscope image collected from the edge of the living structure with fluorescent live/dead dye, (a) is with fluorescence off (b) is with fluorescence on, green micro-rods show living bacteria, red/orange micro-rods show dead bacteria (c) – (e) Show digital images demonstrating the mechanical stability of the 3D printed living structures.

Furthermore, we wanted to ensure that the gel did not inhibit *S. Oneidensis* MR-1's function and its ability to interact with the surrounding environment. It has been previously demonstrated in literature that *S. oneidensis* MR-1 can degrade methyl orange dye (destroying the orange color) by splitting the N=N bond.[21] The living 3D structure were incubate with methyl orange dye to demonstrate that they microbes could retain functionality within the 3D printed lattice. **Error! Reference source not found.** shows digital images of vials of MO dye before and after exposure to the 3D living lattice for 8 h, there is a clear decolorization of the solution indicating a degradation of the MO dye in solution. The degradation of the MO dye was monitored using UV-vis monitoring the UV-vis peak centered around 450 nm with measurements being taken every 2 h. To test the long-term vitality of the *S. Oniedensis* MR-1 in the 3D printed lattice, long term recycling tests of the gels with methyl orange dye were conducted. During these tests a living lattice was placed in a solution of LB media and MO dye. This was then monitored for 8 hs with UV-Vis samples being taken every 2h hour. The sample was stored overnight in the LB-MO solution. The spent LB-MO solution would turn colorless, the solution would be removed, the same living 3D lattice would be washed with sterile LB media and placed in a new solution of MO dye and LB media, this process was repeated for 4 cycles. The stability is shown in the 3D bar graph in **Error! Reference source not found.**. Cycle 3 shows faster degradation of the methyl orange dye. This was attributed to an increase in the number of *S. Oniedensis* MR-1 living in the gel. A control sample of a 3D printed lattice made from the same material but lacking *S. Oniedensis* MR-1 was also printed and allowed to incubate with the methyl orange dye, there was no degradation seen in the MO dye peak at 450 nm. This is good indication that the degradation of MO dye is the result of the *S. Oneidensis* MR-1 and not of a component in the 3D living structure. Based on these results there is good evidence to indicate that the *S. Oneidensis* MR-1 survives the printing process and when embedded in the alginate-cellulose based ink can function and interact with the surrounding environment.

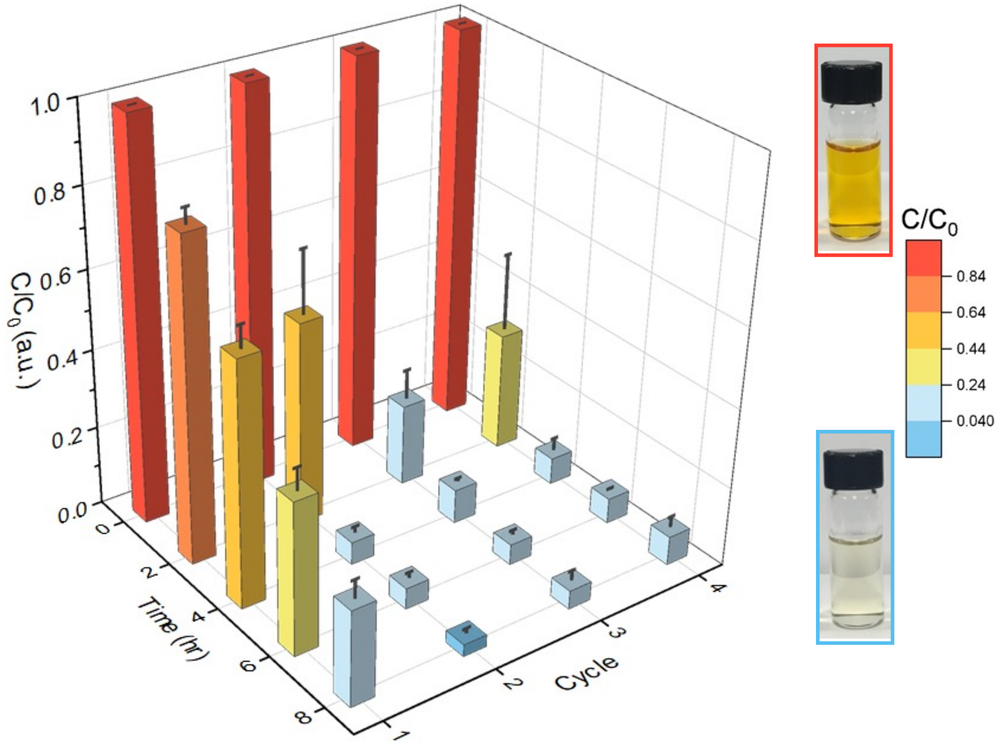

Figure 2.2. Shows a 3D bar graph of the methyl orange (MO) dye degradation over four cycles. C/C$_0$ is the normalized MO dye degradation concentration over 8 h, over 4 cycles. The optical images show vials MO dye before and after being exposed to the 3D living structure.

2.5 Testing of MFC Device

2.5.1 Performance of 3D Printed MFC Anode Compared to Bulk Anode

Following the success of embedding live and functional *S. Oneidensis* MR-1 in the 3D printed structure, we took a step further by turning the entire 3D printed bacteria structure into a living anode for MFCs. We modified the original alginate-nanocellulose to make a living conductive ink appropriate for use as an electrode through the addition of acetylene carbon black. In Error! Reference source not found. the top digital images show the 3D printed living structure, and then the 3D printed living MFC anode, the final image shows the living anode loaded inside of the microbial fuel cell. First is the anode chamber which is filled with LB growth media, followed by a cation exchange membrane and then the cathode chamber with a carbon cloth cathode filled with a ferricyanide solution in phosphate buffer.

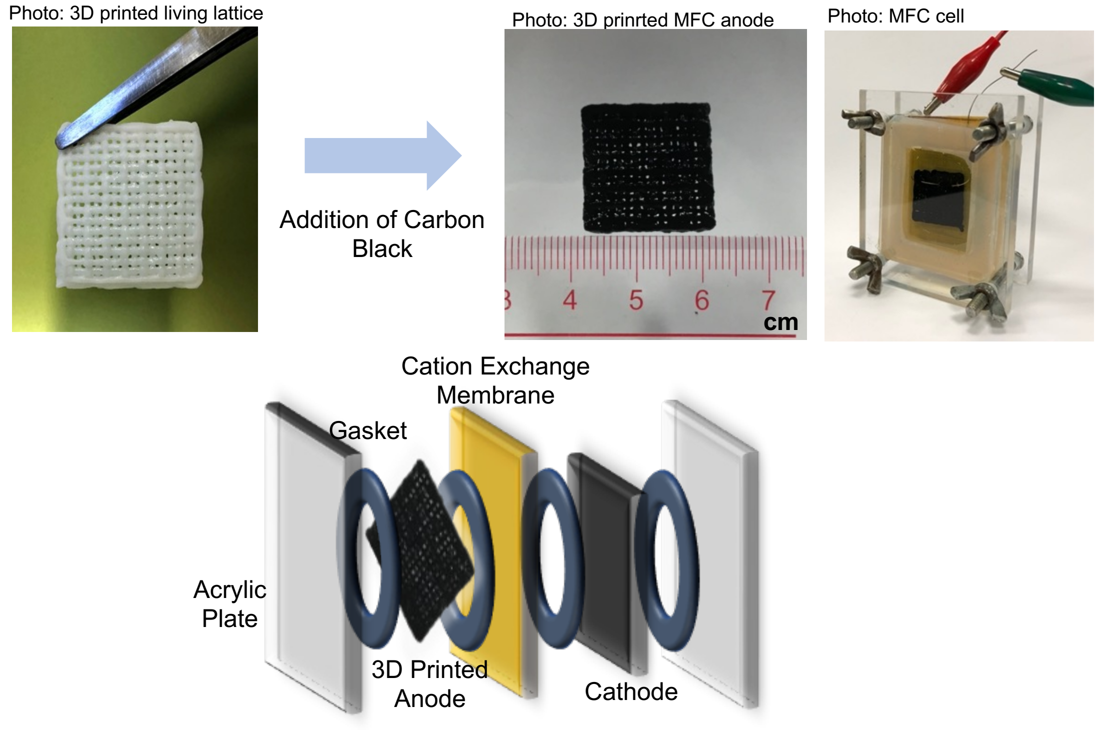

Figure 2.3 Incorporation of acetylene carbon black to living ink to create a conducive 3D printed living MFC anode. The first left most optical image shows the starting 3D printed living structure followed by the 3D printed living MFC anode after the incorporation of acetylene carbon black and the subsequent incorporation into the MFC device. The bottom diagram shows the MFC device with acrylic plates sandwiching the anode chamber containing the 3D printed living MFC anode in a chamber which will be filled with sterile LB media, separated from the cathode chamber by a cation exchange membrane, the cathode chamber contains a carbon cloth cathode the chamber was then filled with ferricyanide phosphate buffer electrolyte.

Power density measurements were conducted using the MFC device shown in **Error! Reference source not found.**. This was done by attaching the resistors listed in the experimental information, the power density plots can be seen in **Error! Reference source not found.**. The blue curve in **Error! Reference source not found.a** corresponds to the 3D printed living anode showing a peak power density of 8.5 W/m^3 normalized to the anode chamber volume, 9 mL. which is in line with the peak power density reported previously on carbon cloth-based anodes.[22-24] Yang et al. achieved a power density of 17 W/m^3 for an anode chamber with a volume of 9 mL,[24] and Hou et al. achieved power density of 4.1 W/m^3 for a 7 mL anode chamber volume.[23] A solid block MFC anode similar in dimensions to the 3D printed anode was made with the same bacteria ink material. This solid block anode was tested in the exact same manner and in the same MFC cell as the 3D printed anode but achieved a considerably lower power density of 3.5 Wm^{-3} (**Figure *2.4*b**). The enhanced power density of the 3D printed anode compared to the solid anode is believed to be due to the increased electrolyte accessible surface area of the 3D printed anode. Furthermore, we believe that the 3D printed structure could facilitate the charge transfer between electrode and electrolyte compared to a solid bulk electrode, because of its relatively open structure.

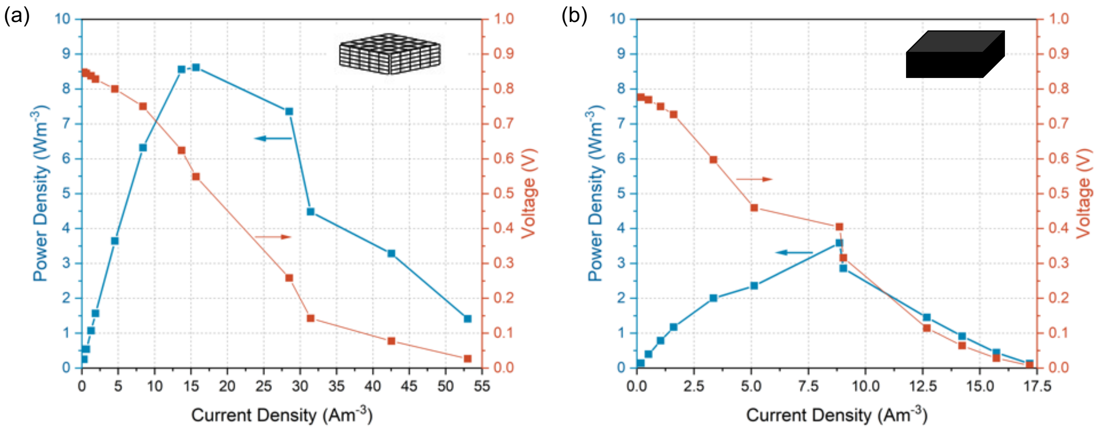

Figure 2.4 Power Density and Polarization Curves for Microbial Fuel Cell. (a) The blue curve corresponds to the power density plot of the 3D printed living MFC anode, the red curve shows the polarization curve. (b) Shows the power density curve in blue and polarization curve in red of a solid living MFC anode similar in dimensions and composition as the 3D printed living MFC anode.

2.5.2 Investigation of Improved Power Density of 3D Printed MFC Anode

Electrochemical Impedance Spectroscopy (EIS) was conducted to further evaluate the difference in performance between the 3D printed living anode and the bulk living anode. Nyquist plots obtained from a 3D printed anode (red curve) and a solid block anode (black curve). Dots corresponding to experimental data, the fitted curve (solid line) is calculated based on the equivalent circuit illustrated in the inset show in **Error! Reference source not found.**. R_Ω represents the Ohmic resistance of the electrode. C is a capacitor and CPE is a constant phase element. Rct,1 and Rct,2 are charge transfer resistances. W is the Warburg diffusion element. The Ohmic resistance

(R_Ω) of the 3D printed anode (12.5 Ω) and the solid block anode (15.6 Ω) are comparable. This is expected because they were made of the same materials and tested in the same cell. Yet, there is a significant difference in the charge transfer resistance (R_{ct}) between the 3D printed and solid block living anode. Jiang et al. demonstrated recently that the diffusion mediated charge transfer can significantly influence the performance of an MFC device, with the soluble diffusion mediators making a significant contribution to the overall charge transferred from the *S. Oneidensis* MR-1 cell to the electrode.[25] Therefore, there are two charge transfer resistances which could be the result of the direct charge transfer from S. Oneidensis MR-1 to the anode surface and the charge transfer through diffusion mediated extracellular electron shuttle.[24-26] The collective R_{ct} ($R_{ct,1} + R_{ct,2}$) is significantly higher for the solid anode (177.1 W) compared to the 3D printed anode (70.7 W). The improved charge transfer in the 3D printed anode compared to the solid anode can be attributed to better diffusion and higher surface area of the 3D printed anode.

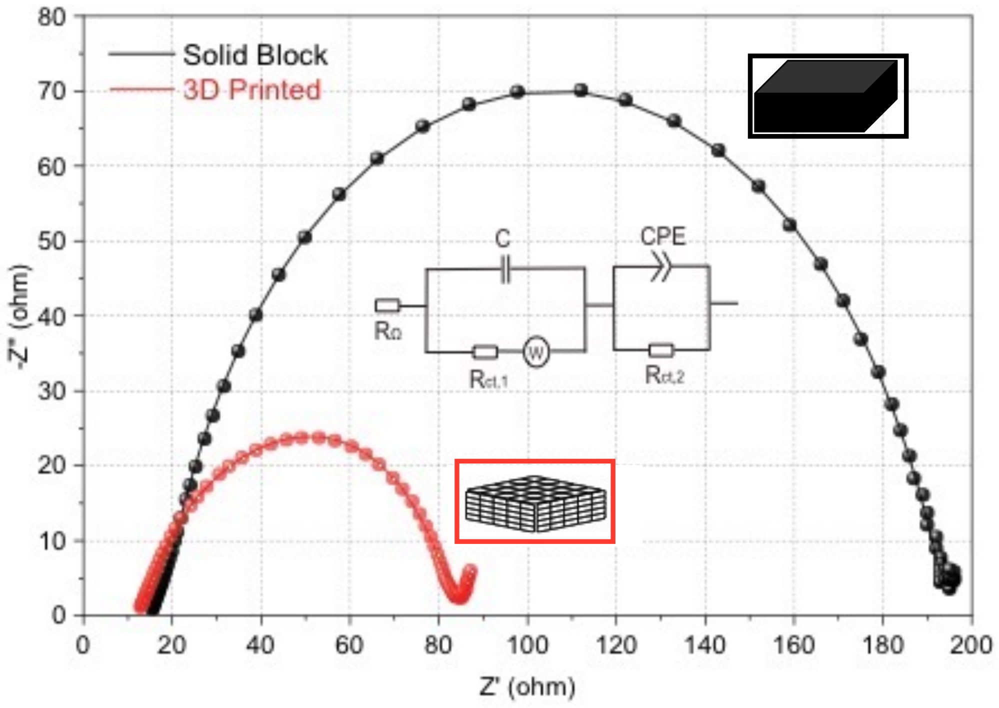

Figure 2.5 Nyquist plots obtained from a living 3D printed anode (red curve) and a solid block living anode of similar size and composition (black curve). Dots correspond to experimental data, while the solid fitted curve is calculated based on the inserted equivalent circuit. In this circuit R_{Ω} represents the Ohmic resistance of the electrode, C is a capacitor and CPE is a constant phase element. $R_{ct,1}$ and $R_{ct,2}$ are charge transfer resistances. W is the Warburg diffusion element.

2.5.3 Stability Testing of MFC Device

Amperometric current–time measurements were performed on the MFC device to evaluate the long-term stability of 3D printed bacteria anode. **Error! Reference source not found.** shows the current–time curve recorded for an MFC device connected to a 5.1 kΩ resistor. The dashed lines in the plot in **Error! Reference source not found.** show where both the anode and cathode solutions were exchanged for the fresh solution, and this was done for 5 cycles. Notably, there is a slight increase in peak current from cycle 1 to 5, reaching a peak current density of ~ 9.23 μA/cm2 . The enhanced current was believed to be due to the increased concentration of bacteria. This was confirmed by the SEM analysis of the bacteria electrode before and after the stability test as shown in the SEM images labeled Start and End in **Error! Reference source not found.**. At the SEM image labeled 'Start' there are a small number of bacteria are embedded in the carbon structure before the stability test. In contrast, the bacteria number increases substantially at the 'End' of the stability test. This direct evidence shows that the bacteria embedded in the 3D living anode are not only alive and retain their properties, but also able to continue to grow in the anode. After reaching the peak current in each cycle, the current decreases gradually to the baseline, possibly due to the depletion of ferricyanide in the catholyte. By replacing both the anolyte and catholyte, the current can be restored, indicating the performance of 3D printed living anode is stable. With regular supplement of new growth medium and catholyte, this device produced electricity for up to at least 93 h.'

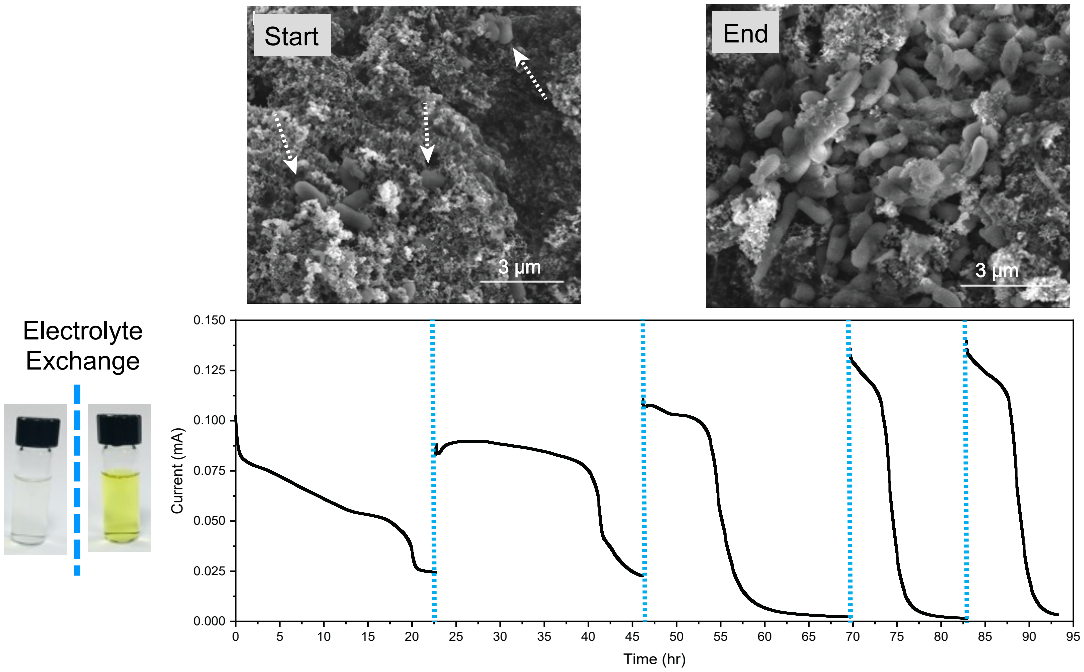

Figure 2.6 Current-time plot of the MFC device, blue dashed lines indicate solvent exchange of both catholyte and anolyte. SEM images show the living MFC anode at the start and end of the current time measurements.

2.6 Conclusion

In this work we have demonstrated for the first time the 3D printing of a living MFC anode. *Shewanella Oneidensis* MR-1 was directly embedded in a printable conductive ink. This work provides insight into the integration of living microbes into 3D functional biomaterial devices. The cured living ink acts as a protective hydrogel around the living microbes, hopefully able to provide a layer of protection to the living microbes inside from environmental toxins. The size and shape of the living anode can easily be tuned through printing parameters. The capability of directly printing living microbe electrodes could open up new possibilities in microbial technologies, biosensing and even fundamental research on the interactions between different bacterial strains.

2.7 References

1. Eş, I., Mousavi Khaneghah, A., Barba, F.J., Saraiva, J.A., Sant'Ana, A.S., and Hashemi, S.M.B. **Recent advancements in lactic acid production - a review**. Food Research International. 2018; **107:** 763-770.
2. Cantera, S., Muñoz, R., Lebrero, R., López, J.C., Rodríguez, Y., and García-Encina, P.A. **Technologies for the bioconversion of methane into more valuable products**. Current Opinion in Biotechnology. 2018; **50:** 128-135.
3. Liamleam, W., and Annachhatre, A.P. **Electron donors for biological sulfate reduction**. Biotechnology Advances. 2007; **25:** 452-463.
4. Kolmert, Å., and Johnson, D.B. **Remediation of acidic waste waters using immobilised, acidophilic sulfate-reducing bacteria**. Journal of Chemical Technology & Biotechnology. 2001; **76:** 836-843.
5. Lovley, D.R., Phillips, E.J.P., Gorby, Y.A., and Landa, E.R. **Microbial reduction of uranium**. Nature. 1991; **350:** 413-416.
6. Golitsch, F., Bücking, C., and Gescher, J. **Proof of principle for an engineered microbial biosensor based on Shewanella oneidensis outer membrane protein complexes**. Biosensors and Bioelectronics. 2013; **47:** 285-291.

7. Wang, G., Qian, F., Saltikov, C.W., Jiao, Y., and Li, Y. **Microbial reduction of graphene oxide by Shewanella**. Nano Research. 2011; **4:** 563-570.

8. Qian, F., Wang, H., Ling, Y., Wang, G., Thelen, M.P., and Li, Y. **Photoenhanced Electrochemical Interaction between Shewanella and a Hematite Nanowire Photoanode**. Nano Letters. 2014; **14:** 3688-3693.

9. Wang, H., Qian, F., and Li, Y. **Solar-assisted microbial fuel cells for bioelectricity and chemical fuel generation**. Nano Energy. 2014; **8:** 264-273.

10. Wang, H., Qian, F., Wang, G., Jiao, Y., He, Z., and Li, Y. **Self-Biased Solar-Microbial Device for Sustainable Hydrogen Generation**. ACS Nano. 2013; **7:** 8728-8735.

11. Qian, F., Wang, G., and Li, Y. **Solar-Driven Microbial Photoelectrochemical Cells with a Nanowire Photocathode**. Nano Letters. 2010; **10:** 4686-4691.

12. Lovley, D.R. **Electromicrobiology**. Annual Review of Microbiology. 2012; **66:** 391-409.

13. Wang, H., Wang, G., Ling, Y., Qian, F., Song, Y., Lu, X., Chen, S., Tong, Y., and Li, Y. **High power density microbial fuel cell with flexible 3D graphene–nickel foam as anode**. Nanoscale. 2013; **5:** 10283-10290.

14. Lehner, B.A.E., Schmieden, D.T., and Meyer, A.S. **A Straightforward Approach for 3D Bacterial Printing**. ACS Synthetic Biology. 2017; **6:** 1124-1130.

15. Qian, F., Zhu, C., Knipe, J.M., Ruelas, S., Stolaroff, J.K., DeOtte, J.R., Duoss, E.B., Spadaccini, C.M., Henard, C.A., Guarnieri, M.T., et al. **Direct Writing of Tunable Living Inks for Bioprocess Intensification**. Nano Letters. 2019.

16. Homan, K.A., Kolesky, D.B., Skylar-Scott, M.A., Herrmann, J., Obuobi, H., Moisan, A., and Lewis, J.A. **Bioprinting of 3D convoluted renal proximal tubules on perfusable chips**. Scientific reports. 2016; **6:** 1-13.

17. Melchels, F.P., Dhert, W.J., Hutmacher, D.W., and Malda, J. **Development and characterisation of a new bioink for additive tissue manufacturing**. Journal of Materials Chemistry B. 2014; **2:** 2282-2289.

18. Lam, C.X.F., Mo, X.M., Teoh, S.H., and Hutmacher, D.W. **Scaffold development using 3D printing with a starch-based polymer**. Materials Science and Engineering: C. 2002; **20:** 49-56.

19. Kuo, C.K., and Ma, P.X. **Ionically crosslinked alginate hydrogels as scaffolds for tissue engineering: Part 1. Structure, gelation rate and mechanical properties**. Biomaterials. 2001; **22:** 511-521.

20. 2004; **LIVE/DEAD® BacLight™ Bacterial Viability Kits**.

21. Cai, P.-J., Xiao, X., He, Y.-R., Li, W.-W., Chu, J., Wu, C., He, M.-X., Zhang, Z., Sheng, G.-P., Lam, M.H.-W., et al. **Anaerobic biodecolorization mechanism of methyl orange by Shewanella oneidensis MR-1**. Applied Microbiology and Biotechnology. 2012; **93:** 1769-1776.

22. Xiao, L., Damien, J., Luo, J., Jang, H.D., Huang, J., and He, Z. **Crumpled graphene particles for microbial fuel cell electrodes**. Journal of Power Sources. 2012; **208:** 187-192.

23. Hou, H., Li, L., Ceylan, C.Ü., Haynes, A., Cope, J., Wilkinson, H.H., Erbay, C., Figueiredo, P.d., and Han, A. **A microfluidic microbial fuel cell array that supports long-term multiplexed analyses of electricigens**. Lab on a Chip. 2012; **12:** 4151-4159.

24. Yang, Y., Liu, T., Zhu, X., Zhang, F., Ye, D., Liao, Q., and Li, Y. **Boosting Power Density of Microbial Fuel Cells with 3D Nitrogen-Doped Graphene Aerogel Electrode**. Advanced Science. 2016; **3:** 1600097.

25. Jiang, X., Hu, J., Fitzgerald, L.A., Biffinger, J.C., Xie, P., Ringeisen, B.R., and Lieber, C.M. **Probing electron transfer mechanisms in Shewanella oneidensis MR-1 using a nanoelectrode platform and single-cell imaging**. Proceedings of the National Academy of Sciences. 2010; **107:** 16806-16810.

26. Baron, D., LaBelle, E., Coursolle, D., Gralnick, J.A., and Bond, D.R. **Electrochemical Measurement of Electron Transfer Kinetics by Shewanella oneidensis MR-1***. Journal of Biological Chemistry. 2009; **284:** 28865-28873.

1. Eş, I., Mousavi Khaneghah, A., Barba, F.J., Saraiva, J.A., Sant'Ana, A.S., and Hashemi, S.M.B. **Recent advancements in lactic acid production - a review**. Food Research International. 2018; **107:** 763-770.
2. Cantera, S., Muñoz, R., Lebrero, R., López, J.C., Rodríguez, Y., and García-Encina, P.A. **Technologies for the bioconversion of methane into more valuable products**. Current Opinion in Biotechnology. 2018; **50:** 128-135.
3. Liamleam, W., and Annachhatre, A.P. **Electron donors for biological sulfate reduction**. Biotechnology Advances. 2007; **25:** 452-463.
4. Kolmert, Å., and Johnson, D.B. **Remediation of acidic waste waters using immobilised, acidophilic sulfate-reducing bacteria**. Journal of Chemical Technology & Biotechnology. 2001; **76:** 836-843.
5. Lovley, D.R., Phillips, E.J.P., Gorby, Y.A., and Landa, E.R. **Microbial reduction of uranium**. Nature. 1991; **350:** 413-416.
6. Golitsch, F., Bücking, C., and Gescher, J. **Proof of principle for an engineered microbial biosensor based on Shewanella oneidensis outer membrane protein complexes**. Biosensors and Bioelectronics. 2013; **47:** 285-291.
7. Wang, G., Qian, F., Saltikov, C.W., Jiao, Y., and Li, Y. **Microbial reduction of graphene oxide by Shewanella**. Nano Research. 2011; **4:** 563-570.
8. Qian, F., Wang, H., Ling, Y., Wang, G., Thelen, M.P., and Li, Y. **Photoenhanced Electrochemical Interaction between Shewanella and a Hematite Nanowire Photoanode**. Nano Letters. 2014; **14:** 3688-3693.

9. Wang, H., Qian, F., and Li, Y. **Solar-assisted microbial fuel cells for bioelectricity and chemical fuel generation**. Nano Energy. 2014; **8:** 264-273.

10. Wang, H., Qian, F., Wang, G., Jiao, Y., He, Z., and Li, Y. **Self-Biased Solar-Microbial Device for Sustainable Hydrogen Generation**. ACS Nano. 2013; **7:** 8728-8735.

11. Qian, F., Wang, G., and Li, Y. **Solar-Driven Microbial Photoelectrochemical Cells with a Nanowire Photocathode**. Nano Letters. 2010; **10:** 4686-4691.

12. Lovley, D.R. **Electromicrobiology**. Annual Review of Microbiology. 2012; **66:** 391-409.

13. Wang, H., Wang, G., Ling, Y., Qian, F., Song, Y., Lu, X., Chen, S., Tong, Y., and Li, Y. **High power density microbial fuel cell with flexible 3D graphene–nickel foam as anode**. Nanoscale. 2013; **5:** 10283-10290.

14. Lehner, B.A.E., Schmieden, D.T., and Meyer, A.S. **A Straightforward Approach for 3D Bacterial Printing**. ACS Synthetic Biology. 2017; **6:** 1124-1130.

15. Qian, F., Zhu, C., Knipe, J.M., Ruelas, S., Stolaroff, J.K., DeOtte, J.R., Duoss, E.B., Spadaccini, C.M., Henard, C.A., Guarnieri, M.T., et al. **Direct Writing of Tunable Living Inks for Bioprocess Intensification**. Nano Letters. 2019.

16. Homan, K.A., Kolesky, D.B., Skylar-Scott, M.A., Herrmann, J., Obuobi, H., Moisan, A., and Lewis, J.A. **Bioprinting of 3D convoluted renal proximal tubules on perfusable chips**. Scientific reports. 2016; **6:** 1-13.

17. Melchels, F.P., Dhert, W.J., Hutmacher, D.W., and Malda, J. **Development and characterisation of a new bioink for additive tissue manufacturing**. Journal of Materials Chemistry B. 2014; **2:** 2282-2289.

18. Lam, C.X.F., Mo, X.M., Teoh, S.H., and Hutmacher, D.W. **Scaffold development using 3D printing with a starch-based polymer**. Materials Science and Engineering: C. 2002; **20:** 49-56.

19. Kuo, C.K., and Ma, P.X. **Ionically crosslinked alginate hydrogels as scaffolds for tissue engineering: Part 1. Structure, gelation rate and mechanical properties**. Biomaterials. 2001; **22:** 511-521.

20. 2004; **LIVE/DEAD® BacLight™ Bacterial Viability Kits**.

21. Cai, P.-J., Xiao, X., He, Y.-R., Li, W.-W., Chu, J., Wu, C., He, M.-X., Zhang, Z., Sheng, G.-P., Lam, M.H.-W., et al. **Anaerobic biodecolorization mechanism of methyl orange by Shewanella oneidensis MR-1**. Applied Microbiology and Biotechnology. 2012; **93:** 1769-1776.

22. Xiao, L., Damien, J., Luo, J., Jang, H.D., Huang, J., and He, Z. **Crumpled graphene particles for microbial fuel cell electrodes**. Journal of Power Sources. 2012; **208:** 187-192.

23. Hou, H., Li, L., Ceylan, C.Ü., Haynes, A., Cope, J., Wilkinson, H.H., Erbay, C., Figueiredo, P.d., and Han, A. **A microfluidic microbial fuel cell array that supports long-term multiplexed analyses of electricigens**. Lab on a Chip. 2012; **12:** 4151-4159.

24. Yang, Y., Liu, T., Zhu, X., Zhang, F., Ye, D., Liao, Q., and Li, Y. **Boosting Power Density of Microbial Fuel Cells with 3D Nitrogen-Doped Graphene Aerogel Electrode**. Advanced Science. 2016; **3:** 1600097.

25. Jiang, X., Hu, J., Fitzgerald, L.A., Biffinger, J.C., Xie, P., Ringeisen, B.R., and Lieber, C.M. **Probing electron transfer mechanisms in Shewanella oneidensis MR-1 using a nanoelectrode platform and single-cell imaging**. Proceedings of the National Academy of Sciences. 2010; **107:** 16806-16810.

26. Baron, D., LaBelle, E., Coursolle, D., Gralnick, J.A., and Bond, D.R. **Electrochemical Measurement of Electron Transfer Kinetics by Shewanella oneidensis MR-1***. Journal of Biological Chemistry. 2009; **284:** 28865-28873.

3 Carbon Host Material for Lithium Metal for Use in Batteries

3.1 Abstract

Lithium-ion batteries are a desirable method to store energy. However, using traditional liquid electrolytes can lead to safety issues due to flammable components found in tradition liquid electrolytes. By using polymer electrolytes these flammable components are removed from the battery housing, creating a safter battery. Ideally lithium metal is used as anode material in lithium-ion batteries, due to its very high energy density when compared with other anode materials. Lithium metal though is not without drawbacks. Lithium metal forms dendrites during charging and discharging due to generation of hotspots on the lithium metal surface. These dendrites short the battery. To try and achieve a safe lithium-ion battery that has high energy density and good cyclability it is proposed to use a porous carbon material as a host for lithium metal to help provide a uniform electric field which can prevent the formation of lithium hotspots during battery cycling preventing the formation of lithium dendrites, coupled with a polymer electrolyte. When designing a carbon host material there are many considerations: (1) What is the interaction of lithium and the surface of the carbon? (2) How well does the polymer electrolyte coat the surface of the carbon material to ensure good conductivity? (3) What is the survivability of the carbon part under compression in the battery coin cell? This work discusses preliminary results of

designing a high-resolution direct ink write printed resorcinol-formaldehyde based carbon material for use as a carbon host material for lithium metal.

3.2 Introduction to Lithium Batteries

Lithium-ion batteries are a powerful tool to help change the way our society uses energy. With the worsening effects of climate change there is a necessity to move away from fossil energy sources. Lithium provides an great material to produce energy dense batteries due to its light weight, and easy of losing electrons.[1] In lithium batteries lithium ions travel from the anode to the cathode during discharging (or use), Error! R eference source not found.**a** shows a schematic illustration of a lithium ion battery. Lithium batteries normally use liquid electrolytes. However, these electrolytes contain flammable components which greatly decrease the safety of the battery. By utilizing polymer electrolytes these flammable components can be removed to help create a safer battery.[1] There are three different types of polymer electrolytes: Gel, liquid and solid polymer electrolytes.[2] Polymer electrolytes utilize ionic conductivity to transfer charge in the battery. They are composed of a host polymer, salt, aprotic solvent, and a filler. [2]

Lithium metal is a desirable anode material to utilize due to its energy density. While this is desirable for both liquid electrolyte batteries it is especially important for polymer electrolyte batteries as they have lower conductivity than traditional liquid electrolytes.[1,3] Lithium dendrites have a higher chance of formation after longer cycling and high current density.[4] Error! Reference source not found.**a** shows a schematic of a l ithium dendrite. In polymer electrolytes there are four growth mechanisms for lithium dendrites as proposed by Cao *et al.*: (1) dendrite growth at the tip which can penetrate through the soft polymer electrolyte, (2) lateral dendrite growth touching the sides of the electrode and the soft polymer electrolyte, (3) subsurface growth which eventually results in the protrusion of the a dendrite (somewhat like an iceberg, where majority is underneath the water surface), (4) redistribution of charge at the interface between the solid polymer electrolyte and the lithium metal.[5] To help mitigate these problems it is proposed to build a porous carbon host material which can help provide multiple lithium nucleation sites, and a more uniform electric field to help prevent the growth of lithium dendrites, (Error! Reference source not found.**c**).

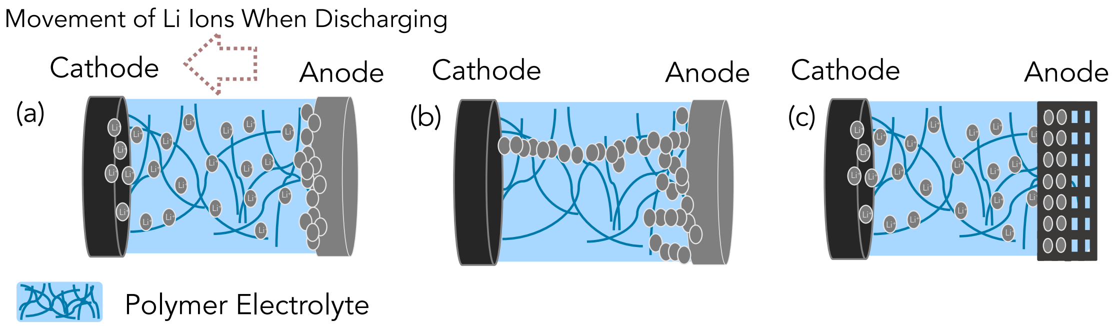

Figure 3.1 Diagram of Lithium Battery. (a) shows standard battery and movement of lithium ions. (b) Shows formation of lithium dendrites. (c) shows proposed carbon host materials.

3.3 Carbon Host Structures for Lithium Metal

Carbon is a desirable host material for lithium because it has good electrical conductivity, high surface area and tunable porosity, is chemically stable and light weight.[6] When designing carbon host materials for use in lithium metal batteries three critical aspects of the carbon material need to be addressed. (1) The interaction of the carbon host material with the lithium metal. (2) The interaction with the polymer electrolyte, and (3) the survivability of the part under compression. **Figure 3.2** shows a schematic of these traits.

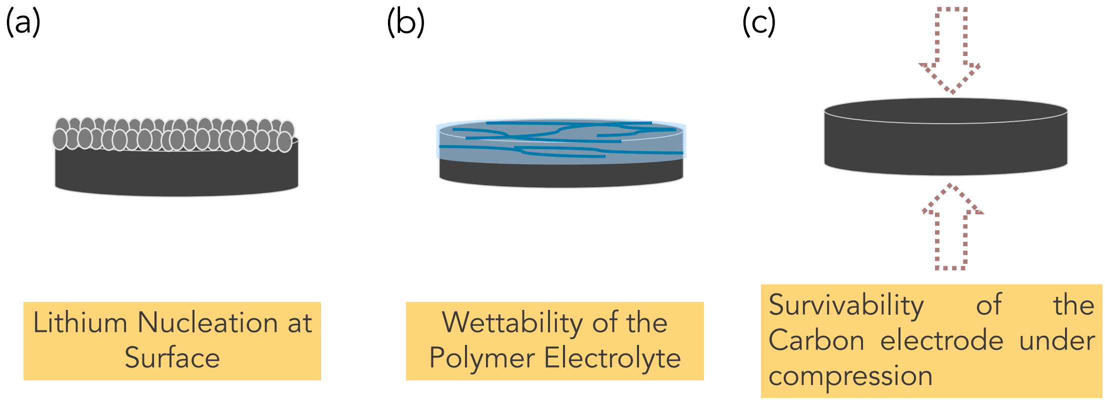

Figure 3.2 Diagram of Desirable Carbon Host Material Qualities. (a) Lithium nucleation and proper dispersion on surface during plating and striping of lithium metal. (b) Wettability of polymer electrolyte to surface of carbon to ensure good electrical connection. (c) Survivability of carbon part under compression when used in coin cell.

3.3.1 Lithium Interaction with Carbon Host Material

Lithium can be introduced to a host material through, electrodeposition, using molten lithium or a roll in method.[7] Lithium interacts are affected by two aspects of the carbon material: porosity and functional groups. By increasing the porosity and surface area more nucleation sites can be provided to the lithium which can help to prevent the growth of dendrites by facilitating more uniform distribution of lithium ions at the surface of the host material.[6,7] It has been demonstrated that the orientation of the pores matter to the longevity of the lithium battery. *Chen et al.* has demonstrated that carbon host materials with lower tortuosity (with vertically aligned pores) can help to lower the likely hood of lithium dendrite formation compared to randomly aligned pores.[8] To large of pores can lead to the generation of 'dead lithium', where lithium metal will build up and detach from the carbon host material. However, a large amount of nanopores can slow down the diffusion of the lithium ions in the carbon host material.[6] The framework and nucleation sites provided by the scaffold material can help maintain the geometric integrity of the electrode during striping and plaiting, helping to reduce swelling of the electrode due to nonuniform plating and striping.[7] Polar functional groups provide lithophilic sites in the carbon host material to help provide uniform nucleation of lithium.[7]

3.3.2 Polymer Electrolyte Interaction with Carbon Host Material

There are a wide variety of polymer electrolytes which can be used in lithium batteries, with many combinations. The chosen polymer electrolyte needs to be chemically combatable the desired electrode, carbon materials have an advantage as they are chemically stable in a variety of environments.[2] To achieve the best performance a polymer electrolyte needs to be evenly coated as a thin film on the electrode surface. There are many different methods to introduce the polymer electrolyte to the electrode including: drop casting, spin coating, dip casting, and in-situ polymerization.[2] The surface chemistry and surface structure of the carbon host material can greatly influence how evenly the polymer electrolyte coats the surface and adheres to the carbon electrode.

3.3.3 Structural Integrity of Carbon Host Material

In addition to a porous carbon structure which can play host to lithium metal the carbon material needs to have good survivability under compression. The carbon host material needs be able to maintain electrical contact with the current collector inside the battery. However, the thickness of the carbon host material needs to be minimal to maintain volumetric energy density. Coupling the formation of carbon aerogels with freeze casting can help to introduce ordered porosity while maintaining a compressible structure. DIW printing is also an attractive way to achieve a tunable structure that is easy to control the thickness of the part based on the numbers of layers printed. Graphene, carbon nanotubes and biobased polymers are common components used for compressible carbon. The van der Waals interactions and π-π interactions between graphene sheets help to facilitate the formation of 3D structures. Carbon nanotubes can be incorporated with other materials to help improve their mechanical and electrical properties provided by their sp^2 hybridization. Biobased polymers such as chitosan and nanocellulose are also used precursors to create pores carbon materials.[9] Resorcinol-formaldehyde (RF) is a particle free formulation which can be used as a precursor for a carbon aerogel formation in combination with many different types of carbon materials such as graphene, carbon nanotubes and cellulose.[10]

3.4 Resorcinol Formaldehyde (RF) Based Carbon

To work to achieve a thin tunable carbon host structure a resorcinol formaldehyde (RF) based particle free ink is an intriguing place to start. To achieve an optimal structure through direct ink write (DIW) 3D printing with a print head less than 200 µm it is easiest to work with a particle free ink. In resorcinol formaldehyde the reaction is polymerized through a base catalyzed condensation reaction, shown in **Figure 3.3**.[11] Carbonized RF parts have been demonstrated previously in energy storage devices and exhibit good conductivity. The porosity can be further modified through tuning ratio of RF to water. After carbonization the RF material can be further etched to introduce further porosity.[10] RF provides a versatile carbon material with good conductivity, it also provides a good starting point for an ink which can be further customized.

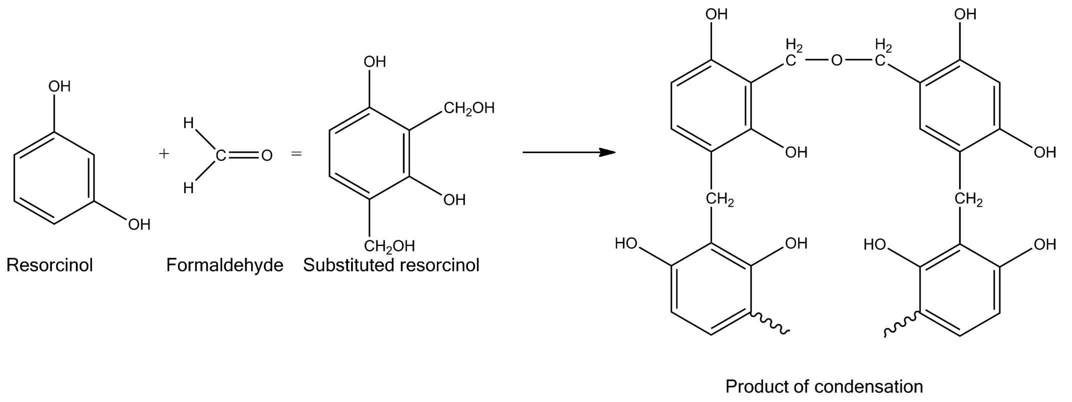

Figure 3.3 Condensation Reaction of Resorcinol Formaldehyde to Produce Final Polymer. Reproduced With permission Copyright Elsevier 2013.[11]

3.5 Experimental

3.5.1 Synthesis of Resorcinol- Formaldehyde (RF) printed part.

Water (7g), sodium carbonate (0.02g) were mixed together, before proceeding it was ensured that the sodium carbonate was fully dissolved in the water. Then resorcinol (0.4g) was added and stirred to fully dissolved, followed by the addition of formaldehyde solution (0.9g). Finally Pluronic F127 (3.5g) was added to aid in printability of the ink. The components were mixed 3 times using a Thinky mixer at 2,500 rpm at 2 min intervals. The ink was then loaded into a 10cc Nordson extrusion head. The ink was printed at a pressure of 20 psi using a 100 μm print head. Immediately after printing the final part was submerged in isooctane in a sealed jar. The part was cured in an 80 °C oven for 3 days. The isooctane was decanted, the part was submerged in acetone for one day at room temperature, this acetone was decanted and replaced with fresh acetone for one more day. Next the part was submerged in DI water for three days at room temperature with the water being exchanged at the end of each day. At the end of the third day the part was frozen with dry ice, after which it was placed on the freeze dryer for 2 days. After this part was carbonized under nitrogen at 800 ^{o}C for 2 h using a ramp rate of 2 ^{o}C min^{-1}.

3.5.2 KOH Etching of RF Carbon Part

After carbonization, the parts were KOH etched by soaking in 1 M KOH solution for 8 h. The part was then dried overnight in the 80 ^{o}C oven. The dried part was annealed under nitrogen at 800 ^{o}C for 1 h using a ramp rate of 5 ^{o}C min^{-1}. The part was cooled in the furnace under flowing nitrogen till room temperature, it was removed and immediately washed with DI water, followed by 3 washes with 0.5 M HCl, and then DI water till the pH was returned to neutral. After washing the part was again dried at 80 ^{o}C overnight before further use.

3.5.3 Characterization and Processing

SEM images were captured using an Apreo SEM in using 10 kV accelerating voltage. XPS spectra was collected using a PHI Quantum 2000 Scanning ESCA Microprobe, using Al Kα x-rays (1486.6 ev). Brunaur-Emmett-Teller (BET) data was collected using a Micromeritics Instrument *via* nitrogen porosimetry. BET surface area was calculated using points in the relative pressure range (p/p^{o}) from 0.01 to 0.07 based on Rouquerol *et al.*[12] RF ink was printed using a mechanical Gantry system. The final part was carbonized using a one-inch Lindberg Blue tube furnace under flowing nitrogen.

3.6 Preliminary Results of RF Printing

Figure 3.4a shows the optical microscope image of the pre-carbonized part. We can see that the diameter of the 100 μm print head is preserved following the freeze drying of the RF part. It is evident in the image that there is distortion of the filament with a thinner diameter being achieved in the center compared to where the filament connects with the rest of the part (**Figure 3.4a**). Following carbonization at 800 °C for 2 h under nitrogen we can see that there is significant shrinkage of the part (**Figure 3.4b**). With the center of the filamenting shrinking from 100 μm to between 50 to 56 μm. It has been previously shown in literature that by decreasing the filament diameter of DIW printed activated RF carbon electrodes from 400 μm to 100 μm can improve the capacitive retention of the electrode from 42 to 70%.[13] We hope that by decreasing the filament size with can help improve the lithium metal hosting ability of the carbon material by increase the surface area, and diffusion in the printed part. The high resolution of 50 μm is achieved only with DIW 3D printing. This is a unique feature, as previously in literature these low resolutions are achieved through templating with a micro-stereo-lithography printing to template a micron structure in a RF part. By removing the templated structure 1 μm channels are achieved in the final RF printed part.[14] We show that we are on the cusp of achieving low resolutions with the simpler

DIW printing method. **Figure 3.4c** shows the internal structure of the RF printed carbon, a dense carbon structure on the interior of the carbon part.

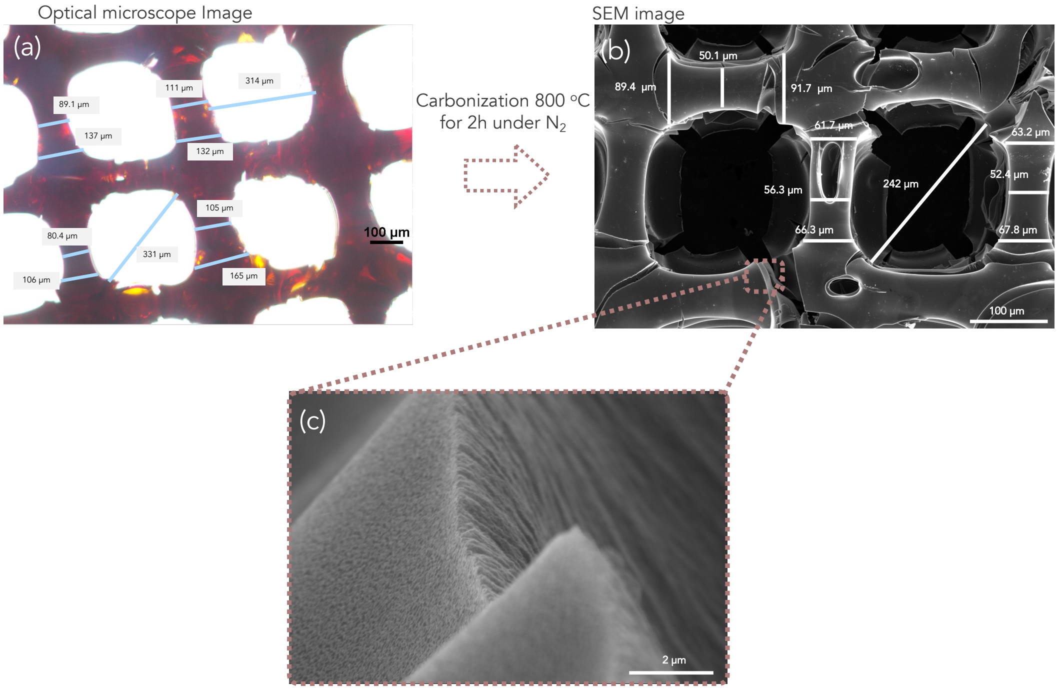

Figure 3.4 Demonstration of Preliminary 3D Printing of RF Part. (a) Optical microscope image which shows the freeze-dried part before carbonization. (b) Shows post carbonized RF part. (c) Shows the interior of the final carbonized RF part.

3.6.1 KOH Etching of RF Printed Part

The carbonized RF part was KOH etched with 1 M KOH solution to introduce further surface area and potentially manipulate the chemical properties. **Figure 3.5(a-c)** show the pre-KOH etched RF carbon sample. There is a skin layer which is forming on the surface of the RF printed part. Error! Reference source not found. shows that b ased on XPS data there is sodium present in the pre-etched carbonized RF part. **Figure**

3.5(d-f) shows the SEM image of the post KOH etched carbonized 3D printed RF part. Visually we can see that there is a decrease in the skin layer and an increase in surface porosity. The XPS data shown in Error! Reference source not found. shows a removal o f sodium from the sample in the post-KOH sample. It is important to remove the skin layer to further expose the carbon surface area for interactions with lithium and the polymer electrolyte.

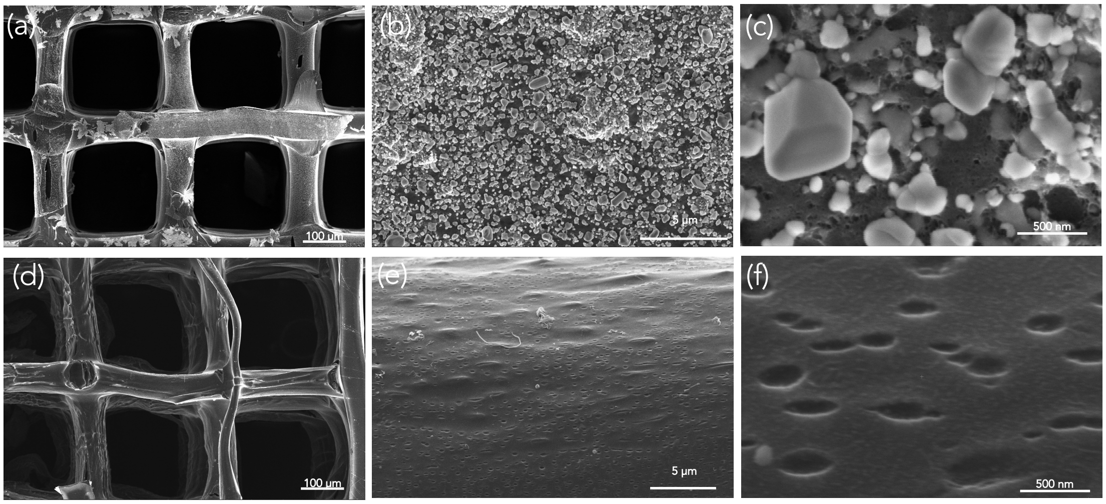

Figure 3.5 SEM images of pre and post KOH etched RF samples. (a-b) show pre KOH etched samples (d-f) show post KOH etched RF samples.

Error! Reference source not found. also shows the surface area changed as result of the K OH etching. DIW printed RF carbon shows an initial BET surface are of 588 m^2 g^{-1} and KOH etching of the RF carbon increases the surface are to 680 m^2 g^{-1}. The increase in surface area can help boost potential nucleation sites for lithium metal, maintaining an even lithium surface coating during cycling of the battery.

Table 3.1 XPS atomic percentage of pre and post KOH etched DIW printed carbonized RF part

Sample	Carbon (at %)	Oxygen (at %)	Sodium (at %)	BET Surface area (m^2 g^{-1})
Base Catalyzed RF Based Carbon	71.07	21.36	6.67	588
KOH Etched Base Catalyzed RF Based Carbon	77.54	20.08	-	680

3.7 Conclusions and Future Work

We have shown through initial work that utilizing a particle free RF ink we can achieve a final resolution with 50 μm carbonized part using DIW printing. Utilizing a mild KOH etching the skin layer was able to be removed and there was an observed increase in BET surface area of the sample. In the future, the KOH etching parameters can be changed to introduce further porosity, through increasing of the KOH etching solution concentration, increasing temperature and time of exposure. CO_2 etching can also be explored as a method to further introduce porosity to the carbonized RF printed part. A detailed characterization of the porosity will be needed to explore its effect on plating and stripping of the lithium inside the host material. Providing useful information on the optimal pore distribution to provide a long cycling life to the battery, and fast movement of the lithium ions. Close attention will need to be paid to the balance between nanoporosity and macroporosity. Characterization of chemical composition to aid in understanding interactions with lithium and polymer electrolyte as well as the lithium nucleation sites. Currently the inherent oxygen content of the carbon material is being used to introduce polar surface oxygen groups, but nitrogen groups have also been shown to be advantageous. Careful study will need to be made of which specific functional groups are providing the desired effect. Characterization of mechanical properties to understand behavior of the carbon host material under compression. It is important for the carbon structure to survive under compression so as lose of connection between the carbon host material and the current collector does not occur. Introducing other materials such as graphene or cellulose to the RF to create a more compressible composite material is also an option.

3.8 Reference

1. Evarts, E.C. **Lithium batteries: To the limits of lithium**. Nature. 2015; **526:** S93-S95.
2. Arya, A., and Sharma, A.L. **Polymer electrolytes for lithium ion batteries: a critical study**. Ionics. 2017; **23:** 497-540.
3. Xu, W., Wang, J., Ding, F., Chen, X., Nasybulin, E., Zhang, Y., and Zhang, J.-G. **Lithium metal anodes for rechargeable batteries**. Energy & Environmental Science. 2014; **7:** 513-537.
4. Zhang, X., Wang, A., Liu, X., and Luo, J. **Dendrites in Lithium Metal Anodes: Suppression, Regulation, and Elimination**. Accounts of Chemical Research. 2019; **52:** 3223-3232.

5. Cao, D., Sun, X., Li, Q., Natan, A., Xiang, P., and Zhu, H. **Lithium Dendrite in All-Solid-State Batteries: Growth Mechanisms, Suppression Strategies, and Characterizations**. Matter. 2020; **3:** 57-94.

6. Ye, H., Xin, S., Yin, Y.-X., and Guo, Y.-G. **Advanced Porous Carbon Materials for High-Efficient Lithium Metal Anodes**. Advanced Energy Materials. 2017; **7:** 1700530.

7. Shi, P., Zhang, X.-Q., Shen, X., Zhang, R., Liu, H., and Zhang, Q. **A Review of Composite Lithium Metal Anode for Practical Applications**. Advanced Materials Technologies. 2020; **5:** 1900806.

8. Chen, H., Pei, A., Wan, J., Lin, D., Vilá, R., Wang, H., Mackanic, D., Steinrück, H.-G., Huang, W., Li, Y., et al. **Tortuosity Effects in Lithium-Metal Host Anodes**. Joule. 2020; **4:** 938-952.

9. Wang, Z., Tian, M., Yu, J., Jiao, J., Yang, C., Pei, L., Yan, C., and Fang, C. **Recent advances of 3D compressible carbon assemblies: A review of synthesis, properties and applications in energy and environment**. Journal of Environmental Chemical Engineering. 2021; **9:** 106269.

10. Li, F., Xie, L., Sun, G., Kong, Q., Su, F., Cao, Y., Wei, J., Ahmad, A., Guo, X., and Chen, C.-M. **Resorcinol-formaldehyde based carbon aerogel: Preparation, structure and applications in energy storage devices**. Microporous and Mesoporous Materials. 2019; **279:** 293-315.

11. Gaca, K.Z., and Sefcik, J. **Mechanism and kinetics of nanostructure evolution during early stages of resorcinol-formaldehyde polymerisation**. Journal of colloid and interface science. 2013; **406:** 51-59.

12. Rouquerol, J., Llewellyn, P., and Rouquerol, F. **Is the BET equation applicable to microporous adsorbents**. Stud. Surf. Sci. Catal. 2007; **160:** 49-56.

13. Chandrasekaran, S., Yao, B., Liu, T., Xiao, W., Song, Y., Qian, F., Zhu, C., Duoss, E.B., Spadaccini, C.M., Li, Y., et al. **Direct ink writing of organic and carbon aerogels**. Materials Horizons. 2018; **5:** 1166-1175.

14. Chandrasekaran, S., Forien, J.-B., Campbell, P.G., Oakdale, J.S., Mancini, J.A., Worsley, M.A., and Biener, J. **Carbon aerogels with integrated engineered macroporous architectures for improved mass transport**. Carbon. 2021; **179:** 125-132.

4 CO_2 Capture Using Cellulose Based Carbon Materials

4.1 Abstract

To avert the devastating impacts of global climate change technologies which prevent CO_2 from entering or remove CO_2 from the atmosphere are critical. Solid sorbents are an attractive option to capture CO_2 from post combustion and other point sources due to their lower energy needs for regeneration. Carbon materials provide a solid CO_2 sorbet which is chemically stable in diverse environments. In carbon materials CO_2 uptake is influenced by both the structure of the carbon materials and the chemical dopants. The structure and dopants of carbon materials can be tuned synthetically. In this work we design and synthesize carbon materials to target CO_2 uptake at low pressure conditions to mimic the low CO2 concentrations found in the CO_2 point sources of flue gas, CO_2 concentration of 8-15 %, or biogas, CO_2 concentration of ~40%. I will present some preliminary results on using cellulose-derived carbon materials for CO_2 capture. To improve the understanding of the inherent structure and composition of the cellulose-carbon materials interplay with their CO_2 capture ability.

4.2 Introduction

4.2.1 Current Impacts of Climate Change

It is becoming more apparent with every passing year that the effects of climate change are being felt throughout the globe. Since the advent of the industrial age, in the mid 1700s, the amount of carbon dioxide (CO_2) in earth's atmosphere has increased drastically from 280 ppm before the industrial era to 412.5 ppm in 2020. Before the industrial revolution the atmospheric carbon dioxide levels did not range above 300 ppm. [1] The increase in CO_2 in the atmosphere driving an increase in surface temperatures. Even if the CO_2 emissions are drastically curbed, future projections still indicate that there will be a surface temperature increase over 1.5 ^{o}C.[2] The effects of climate change will be broad reaching. It is important to remember that we are not alone on this planet and that climate changes will not affect us alone, but all the flora and fauna. As stewards of this planet, we must work to ensure the survival of the planet.

4.2.2 Sources of CO_2

There are three major sources of CO_2: Biogas, Flue gas, and atmospheric air. Air is composed of 0.04% CO_2, it is the lowest concentration of CO_2 of any source. This provides the greatest challenge. As the material which pulls CO_2 from the atmosphere must have good selectivity of CO_2 over other air components like nitrogen.[1] Biogas contains around 40% CO_2 the other component is mainly methane with some sulfide species.[3] The ability to remove CO_2 from biogas provides an opportunity to create methane gas for use as a power supply, removing the need to use nonrenewable methane sources.[4] The amount of CO_2 in flue gas varies depending on the combustion source. The range can fluctuate between 8 to 15%. In addition to CO_2 flue gas contains water vapor, NO_x, and SO_x species which can affect capture materials. Flue gas is also emitted at high initial temperatures which may require varying degrees of cooling before it can be successfully feed into a capture material.[5] Flue gas is emitted by power plants, with more technologies being electrified there will still be a dependence on CO_2 emitting power plants. For the experiments presented here we will focus on testing the material under CO_2 pressure of 10 kPa and 40 kPa to mimic flue gas and biogas concentrations.

4.2.3 Solid State CO_2 Sorbents vs Liquid CO_2 Sorbents

For CO_2 capture there are two major branches of sorbents, liquid and solid. Liquid sorbents are commonly composed of liquid amines capturing CO_2 through chemisorption. Monoethanolamine (MEA) in water is commonly used in commercial CO_2 capture systems. The regeneration of this aqueous liquid sorbent though is energy intensive and contributes greatly to the cost of implementation this technology in real power plants.[6] Solid sorbents provide a CO_2 capture alternative with less energy intensive needs to regenerate the capture material due to the lack of water.[7] Depending on the composition of the solid sorbent chemisorption, physisorption or a combination can be used to capture CO_2. Chemisorption systems include amine functionalized supports and alkali-metal carbonates. While physisorption systems include Metal-organic Frameworks (MOFs), zeolites and activated carbons. When designing a CO_2

capture material critical criteria are: CO_2 uptake ability, fast uptake kinetics, good regeneration following capture, thermal and chemical stability.[7]

4.3 Characteristics of Carbon Materials for CO_2 Capture

We chose to focus on carbon materials for solid CO_2 sorbents because they are chemically stable and exhibit high tunable surface area. **Figure 4.1** shows a schematic representation of how not only increasing the surface area but decreasing the pore width can help improve the CO_2 interactions with the surface of the carbon. Narrow pore widths allow for more opportunities for the free electrons on CO_2 molecule to interact with the carbon surface. The pore structure of the carbon surface is a dominate factor in the CO_2 uptake ability of the carbon material. [8]

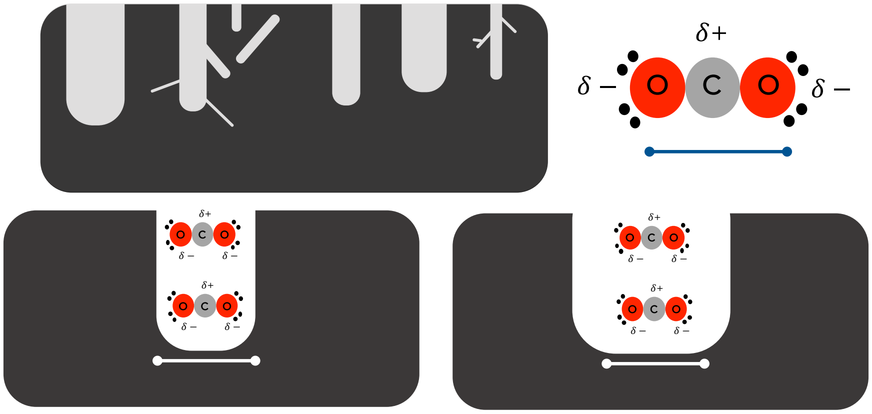

Figure 4.1. Schematic Representation of CO_2 Interaction with the Surface of a Carbon Material

Figure 4.2 shows a schematic of the desired oxygen functional groups, carboxyl and hydroxyl groups, to enhance CO_2 capture (in addition to improving the surface area). These interactions occur through partial positive charge found on the carbon of the CO_2 molecule and the negative partial charge found on the surface of the oxygen atom.[8] It is important to pay attention to the oxygen content of a carbon material when it comes to investigating the CO_2 capture properties as there is inherent oxygen content found on activated carbons.

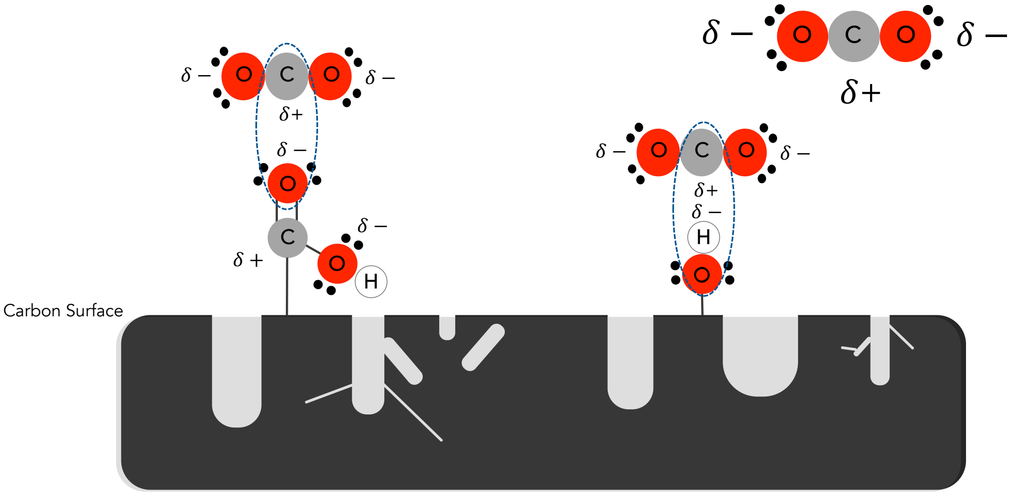

Figure 4.2 Schematic of Desired Oxygen Functional Groups for CO_2 Capture.

4.3.1 Background of Cellulose Material

We chose cellulose as starting material because it is derived from biomass, and if grown sustainably it can be considered a renewable feedstock. Cellulose is found in the cell wall of a plant cell intertwined with hemicellulose and lignin. The cellulose must be extracted to produce the desired final product. We will look at two different types of cellulose material: nanocrystalline and microcrystalline cellulose. Some sources for nanocrystalline cellulose are: wood, cotton, hemp and flax.[9] The source and method of isolating cellulose dictates the composition of the resulting cellulose materials.[10] The most common method for industrial production of cellulose nanocrystals is through sulfuric acid hydrolysis. [9,11] The Celluforce company reports the size dimensions of the final cellulose nanocrystal as 2-10 nm width and 80-150 nm in length. Commercial microcrystalline cellulose (AMCC) is mainly derived from wood and cotton and is also produced using acid hydrolysis methods.[10] The microcrystalline cellulose utilized in this work is from Alfa Aesar, the company reports a size dimension of 250 to 32 μm in length. Despite the particle size different the cellulose starting materials are chemically similar, as seen through the comparison of the IR spectra of the raw cellulose powder in **Figure 4.3**. By narrowing the pore size and through surface area manipulations we can increase the CO_2 uptake ability of carbon monolith derived from commercial cellulose. Without further chemical modification to the cellulose material.

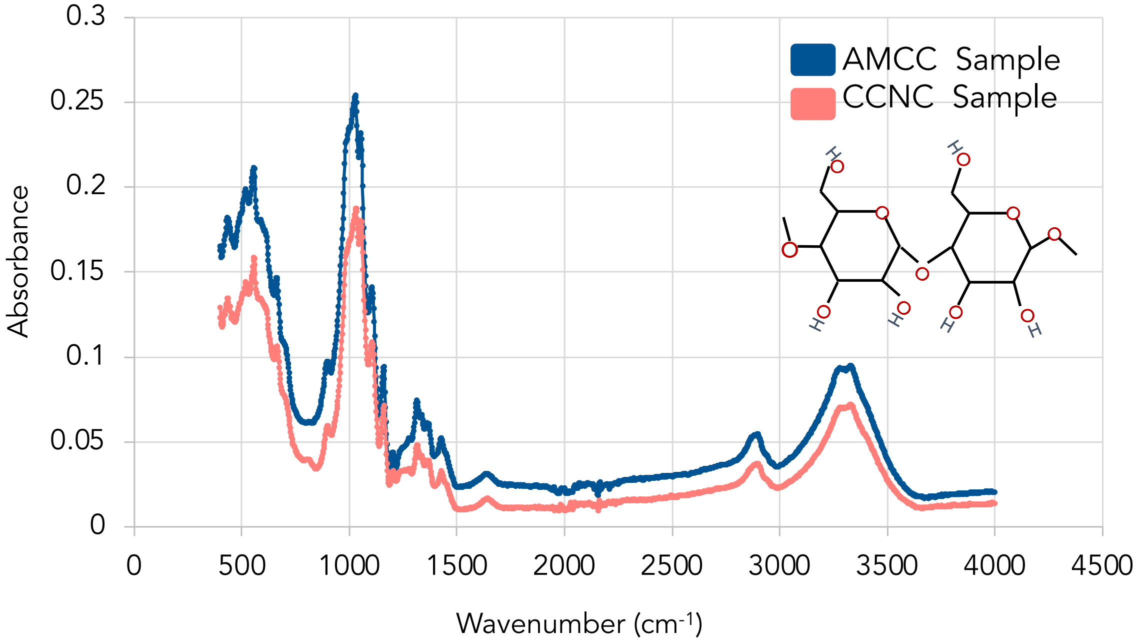

Figure 4.3 IR Spectra of Nanocrystalline Cellulose Compared to Microcrystalline Cellulose. Insert shows the cellulose polymer.

4.4 Experimental

4.4.1 Formulation of nanocrystalline cellulose puck

Nanocrystalline cellulose powder (1g) was mixed with of water (8g) in a Flack Tech container. The mixture was mixed three times at 2500 rpm in one-minute intervals using the Flack Tech. The resulting paste was the spread into silicon rubber molds of 1 cm diameter circles, on glass slides. The rubber molds on the glass slides were then placed glass side down on dry ice till they were frozen. The samples were then freeze dried for approximately 24 h. After the sample was removed from the freeze drier it was carbonized at a ramp rate of 5 °C min^{-1} to 800 °C and held for 2 h under flowing nitrogen. After this heating period the sample was allowed to free cool to room temperature. Producing the CCNC sample.

4.4.2 Formulation of microcrystalline cellulose puck

Microcrystalline cellulose powder (1g) was mixed with of water (2g) in a Flack Tech container. The mixture was mixed three times at 2500 rpm in one-minute intervals using the Flack Tech. The resulting paste was the spread into silicon rubber molds of 1 cm diameter circles, on glass slides. The rubber molds on the glass slides were then placed glass side down on dry ice till they were frozen. The samples were then freeze dried for approximately 24 h. After the sample was removed from the freeze drier it was carbonized at a ramp rate of 5 ^{o} C min^{-1} to 800 ^{o}C and held for 2 h under flowing nitrogen. After this heating period the sample was allowed to free cool to room temperature. Producing the AMCC sample.

4.4.3 Liquid nitrogen freezing

The nanocrystalline cellulose and microcrystalline cellulose pastes were loaded into the silicon mold on a glass slide. This entire apparatus was submerged into a dewar of liquid nitrogen. The sample was left for approximately 10 mins. After it was removed and immediately freeze dried for approximately 24 h. Both the samples were carbonized at 800 ^{o}C for 2 h under nitrogen with a ramp rate of 5^{o}C min^{-1}. Producing liquid nitrogen frozen AMCC and CNCC samples

4.4.4 Washing of carbonized cellulose parts

The following procedure was followed for both the nanocrystalline cellulose samples and the microcrystalline cellulose samples. CCNC carbonized pucks (0.04 g) and 0.1 g of AMCC carbonized pucks were placed in 20 mL of DI water at 80 °C for 8 h. Vacuum was pulled on the sample to ensure that it was fully saturated with water. The DI water was the decanted and 20 mL of 0.5 M HCl solution was added to the carbon samples and vacuum was pulled again. Three 0.5 M HCl washes were conducted with vacuum being pulled between each. After the 0.5 M HCl washes DI water washes were conducted until the pH of the resulting decanted solution was neutral. In total for one set of samples 150 mL of total solution (water and HCl) was used to wash the samples. After this washing the samples were dried in an 80 °C oven overnight.

4.4.5 CO_2 uptake testing

The sample was degassed in a vacuum oven at 110 °C for a minimum of 12 hs. The sample was then loaded into a home-built pressure decay system. One side (referred to as upstream) held a pressure sensor and a fixed volume container of 50 mL (about the same volume as the corresponding sample cell) this was then separated by a valve from a second side which contains a water jacked glass sample cell (referred to as sample side). Before each uptake experiment air was injected to calculate the volume in the sample side. To do this the upstream side was charged till it reached atmospheric pressure, isolated, and then exposed to the sample side before closing the in-between valve. This was done at 25 ^{o}C. Vacuum is then pulled on the entire system. While under dynamic vacuum the temperature is then raised to 50 ^{o}C on the water jacked sample cell to allow for any reaming gas in the sample to leave. After the sample returns to 25 ^{o}C the sample side is isolated from the upstream side. The upstream side is charged with double the desired test pressure of CO_2, the valve is open to expose the sample briefly to the upstream side allowing the CO_2 to charge the sample side. After the valve is closed and the sample side and upstream are isolated. The drop in pressure is observed in the sample side. The number of moles of CO_2 captured by the sample can be calculated by comparing the pressure drop seen in the sample chamber to the starting number of moles transferred from the upstream chamber. CO_2 exposure was conducted at 25 ^{o}C. Between each CO_2 exposure the entire system is placed under dynamic vacuum and the sample cell is heated to 50 ^{o}C. The moles of CO_2 uptake were calculated using the ideal gas law, $PV=nRT$, and normalized to the amount of sample used for the CO_2 uptake experiments.

4.4.6 Characterization

SEM images were captured using an Apreo SEM in standard mode. XPS spectra was collected using a PHI Quantum 2000 Scanning ESCA Microprobe, using Al Kα x-rays (1486.6 ev). Brunaur-Emmett-Teller (BET) data was collected using a Micromeritics Instrument *via* nitrogen porosimetry. BET surface area was calculated using points in the relative pressure range (p/p^{o}) from 0.02 to 0.07 for CCNC samples and dry ice frozen AMCC sample, a relative pressure range (p/p^{o}) from 0.05 to 0.10

was used for liquid nitrogen frozen AMCC sample based on Rouquerol *et al.*[12]. IR spectra was collected using a Bruker Alpha FT-IR spectrometer. The final part was carbonized using a one-inch Lindberg Blue tube furnace under flowing nitrogen.

4.5 Effect of Surface Coating on CO_2 uptake of CCNC Sample

Initial CO_2 uptake testing was conducted with a dry ice frozen CCNC sample. The CCNC sample achieved a CO_2 uptake of 24 mg g^{-1} at 10 kPa of CO_2 and 47 mg g^{-1} at 40 kPa, (**Figure 4.4)** This uptake is lower than expected, especially for the 40 kPa pressure, as based on previous literature we would expect a range of CO_2 uptake of between 20 and 40 mg g^{-1} for 10 kPa uptake and between 75 and 85 mg g^{-1} for 40 kPa,[13-17] with the best samples for 40 kPa capture achieving CO_2 uptake of approximately 120 mg g^{-1}.[8,18,19] Upon closer inspection of the SEM images we can see that there is a coating forming on the surface on the CCNC sample. This coating can be seen in the SEM images in **Figure 4.4b-d**. Based on preliminary XPS data it appears that a significant amount of sodium is appearing in the sample, about 15.54 at % (**Table 4.1**). This amount of sodium than would not be expected based on synthesis parameters and other sample treatments. Currently, the sodium is believed to be inherent to CCNC precursor possibly because of the acid hydrolysis. The formation of this coating on the surface of the carbon is potentially blocking the surface needed to facilitate interactions with the CO_2 molecule. Preliminary BET shows that the surface area for the sample with the sodium coating is 643 m^2 g^{-1}.

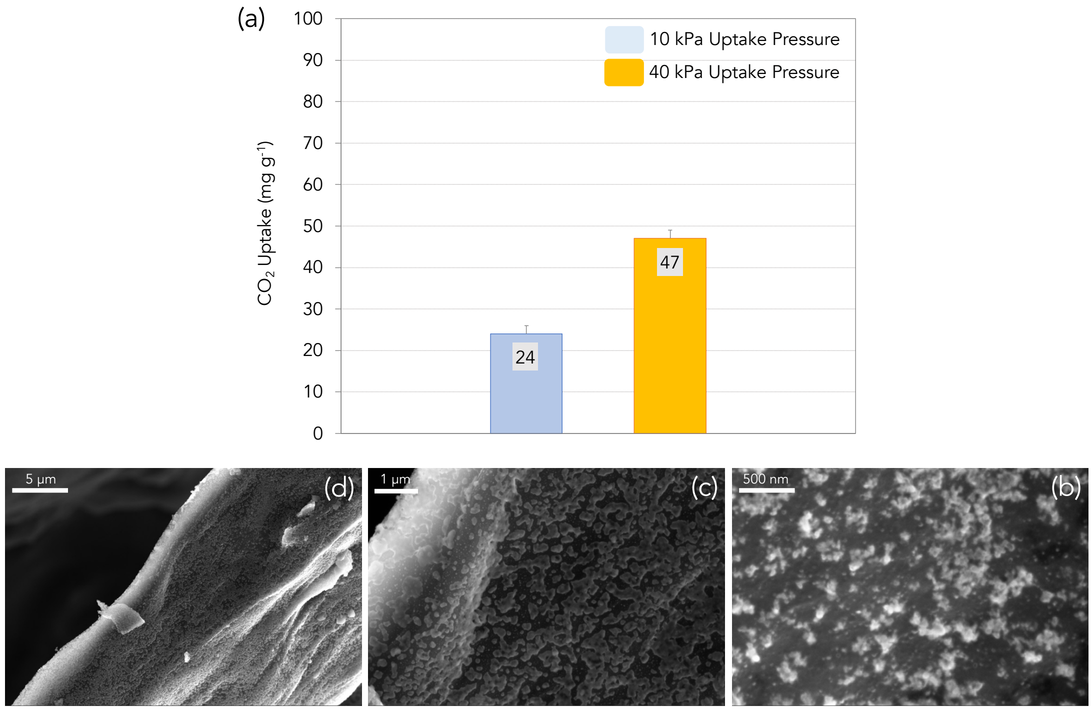

Figure 4.4 CO_2 Uptake Data for CCNC Sample Frozen with Dry Ice, and Corresponding SEM Images. (a) Shows CO_2 uptake data for 10 kPa CO_2 uptake pressure at 25 °C in blue and 40 kPa partial CO_2 uptake pressure at 25 °C is shown in yellow. (b-d) correspond to SEM images of the CCNC part at 500 nm, 1 µm, and 5 µm respectively.

After a mild water wash, of soaking the sample DI water at room temperature for 7 h, there is a decrease in the amount of sodium seen in the XPS data from 15.54 to 2.17 at %. Encouraged by this result a more thorough water wash was conducted. Following this more intense water wash there was no sodium apparent in the XPS spectra (**Table 4.1**). **Figure 4.5** shows the increase in CO_2 uptake of the washed compared to unwashed CCNC sample. The increase at 10 kPa is from 24 mg g^{-1} to 35 mg g^{-1} there is a larger increase at the 40 kPa pressure, increasing from 35 mg g^{-1} to 71 mg g^{-1}, for unwashed compared to washed respectively. In the SEM images shown in **Figure 4.5b-d** no coating can be seen. This coupled with the lack of sodium in the XPS spectra seems to correspond to a removal of the coating, seen on the carbon surface in **Figure 4.4b-d**. This could indicate that the increase in CO_2 uptake is the result of the exposure of more carbon surface area, increasing the interactions of the carbon surface with CO_2 molecules. The washed CCNC CO_2 uptake is more in line with previous literature. [13-17]

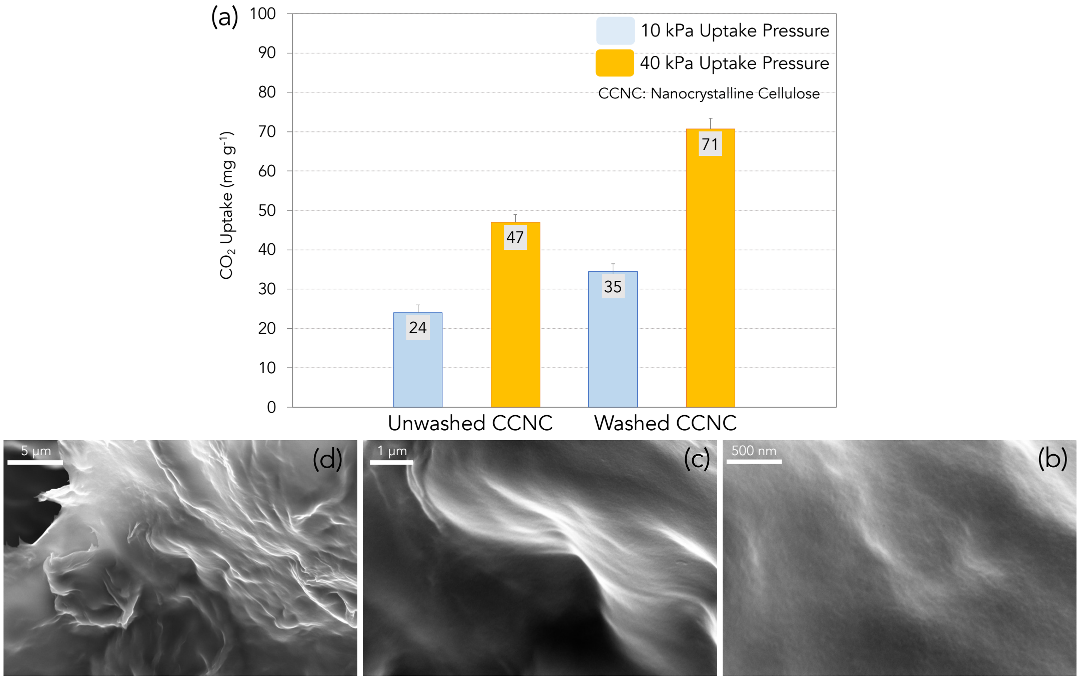

Figure 4.5 CO_2 Uptake Data for both Unwashed and Washed CCNC Sample Frozen with Dry Ice, and Corresponding SEM Images of Washed CCNC Samples. (a) Shows CO_2 uptake data for 10 kPa CO_2 uptake pressure at 25 °C in blue and 40 kPa partial CO_2 uptake pressure at 25 °C is shown in yellow. (b-d) correspond to SEM images of the CCNC part at 500 nm, 1 µm, and 5 µm respectively.

4.6 Carbon Structure Influence on CO_2 Uptake of CCNC Sample

We can manipulate the structure of the carbon sample through freeze casting. There are two approaches we will utilize are Flash freezing and directional ice templating. Lavoine *et al.* found that the rapid freezing, using the flash freezing method, of a cellulose nanofibrils (CNF) suspension preserved the intrinsic structure of the CNF suspension and resulted in smaller pore sizes. While slower freezing caused a separation between the suspended CNFs and solvent generating an ice template with a larger pore size.[20]

4.6.1 Effect of Dry Ice Freezing on CCNC Structure

When the sample is frozen with dry ice we are utilizing what I am calling a 'pseudo-directional casting method'. **Figure *4.6*** shows SEM images of the two faces of the washed dry ice frozen CCNC samples. By comparing the two sides we can see that there are two structures forming. The SEM image in **Figure 4.6a** exhibits a flaky structure and there appears to be pebbling on the surface upon closer examination in the 500 nm SEM image shown in **Figure 4.6b** of the same side. **Figure 4.6c-d** shows the other face of the carbon puck, this face shows a more ribbon like structure and there is an absence of the pebbling seen in **Figure *4.6*b**. The ribbon like structure is similar to the structure seen in directional freeze casted cellulose nanocrystal aerogel in the work by Munier *et al.*[21] I believe the incomplete structure is the result of the formation of an uneven thermal gradient. A glass slide was used to make contact between the dry ice and would not conduct the cold as well as a metal. The silicon mold used could also be providing a form of insulation. Munier *et al.* utilize a cooling rate between 0.5 to 15 K/min when templating their sample.[21] Our sample was directly introduced to the dry ice, this could have resulted in an initial rapid freezing of the sample which first made contact with the cold, followed by slower freezing of the rest of the sample. The pebbling which is seen in **Figure *4.6*b** is believed to be a residual effect of the surface coating which has seen in previous unwashed samples.

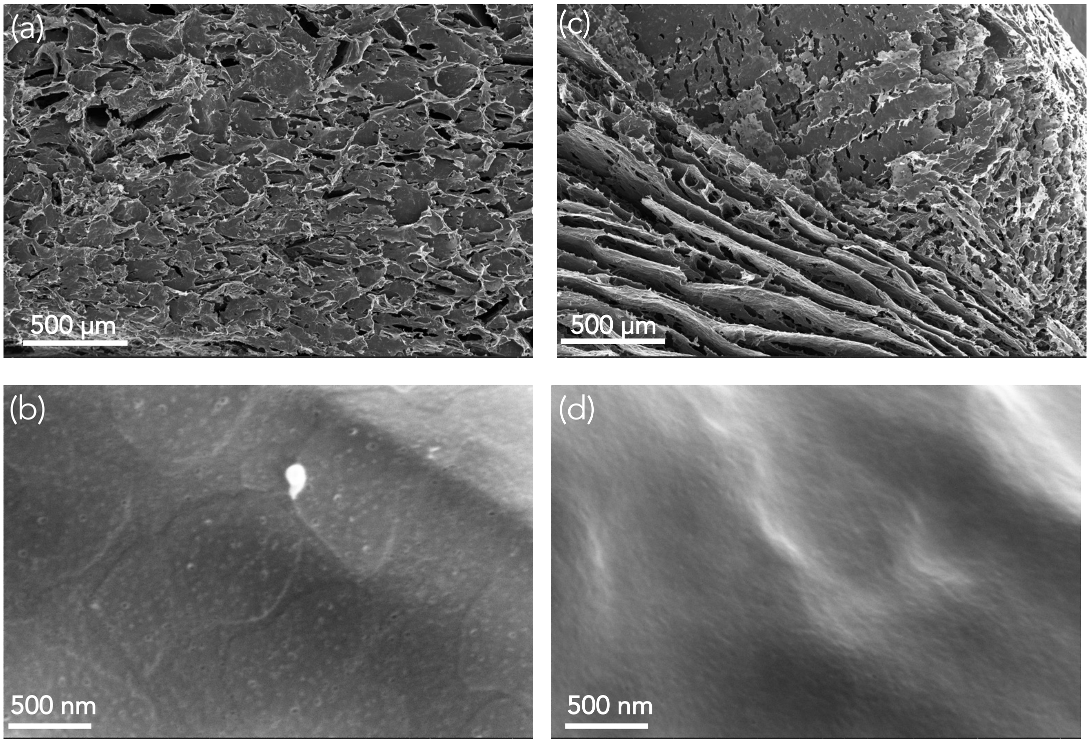

Figure 4.6 SEM Images of Washed Dry Ice Frozen CCNC Sample. (a) and (b) show side 1 of the CCNC monolith while (c) and (d) show side 2 of the CCNC monolith.

4.6.2 Effect of Liquid Nitrogen Freezing on CCNC Structure

To try and achieve a smaller pore size and higher surface area we froze a CCNC sample using liquid nitrogen. Based on the SEM in **Figure 4.7** compared to that in **Figure *4.6*** we do see a change in structure. Three different structures are visible in the liquid nitrogen frozen CCNC sample. SEM image in **Figure 4.7b** shows very dense structure with a similar coating to what is seen in the SEM images in **Figure 4.4** which we attributed to a sodium containing coating. **Figure 4.7c** shows a more open structure, but the coating is still present on the surface, the SEM image **Figure 4.7d** shows a much more open structure and little of the coating. It is reasonable to assume that this coating is the same sodium-based coating seen in the dry ice frozen samples as the sample is made with the same nanocrystalline cellulose starting material. Insulating effects from contact with the silicon rubber mold at the edge could be the reason for the difference in the structure. The region seen in SEM image **Figure *4.7*d** would be in contact with the silicon rubber mold. In the future elemental analysis would be useful to conduct on each region of the unwashed liquid nitrogen frozen CCNC part seen in **Figure *4.7*** to better understand the distribution of the sodium-based coating.

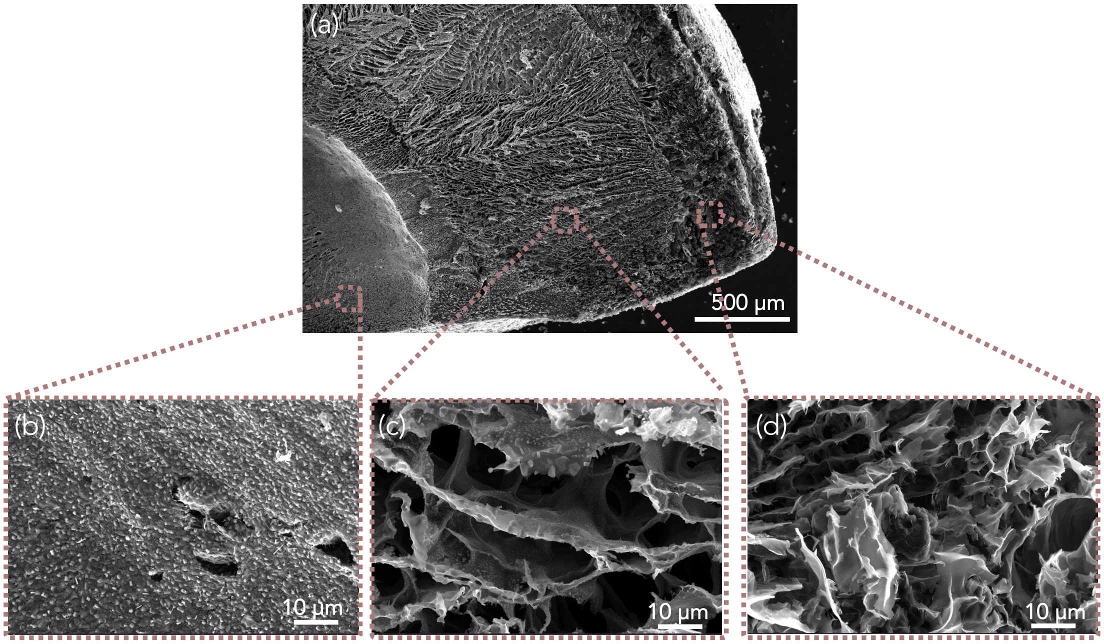

Figure 4.7 Unwashed Liquid Nitrogen Frozen CCNC. (a) corresponds to 500 μm scale image (b-d) correspond to 10 μm images of the three regions of interest.

We conducted BET surface area measurements on the unwashed liquid nitrogen frozen CCNC sample. The resulting surface area was 267 m^2 g^{-1} this is lower than the BET surface area for the unwashed dry ice frozen sample with similar chemical composition, which achieved a BET surface are of 643 m^2 g^{-1}. This is not the expected result based on the freezing method applied. We would expect the liquid nitrogen sample to achieve the higher surface area. The discrepancy in the BET surface could potentially be explained by the dense coating that we are seeing at the center of the liquid nitrogen frozen sample. Also, the even growth of the sodium-based coating in the frozen dry ice samples could be introducing further surface area through surface roughness. **Figure 4.8** shows the resulting BJH calculated pore size distribution of the dry ice frozen sample compared with the liquid nitrogen sample. The pore size distributions are similar between the two samples in the region, between 15 to 130 Å (1.5 to 130 nm).

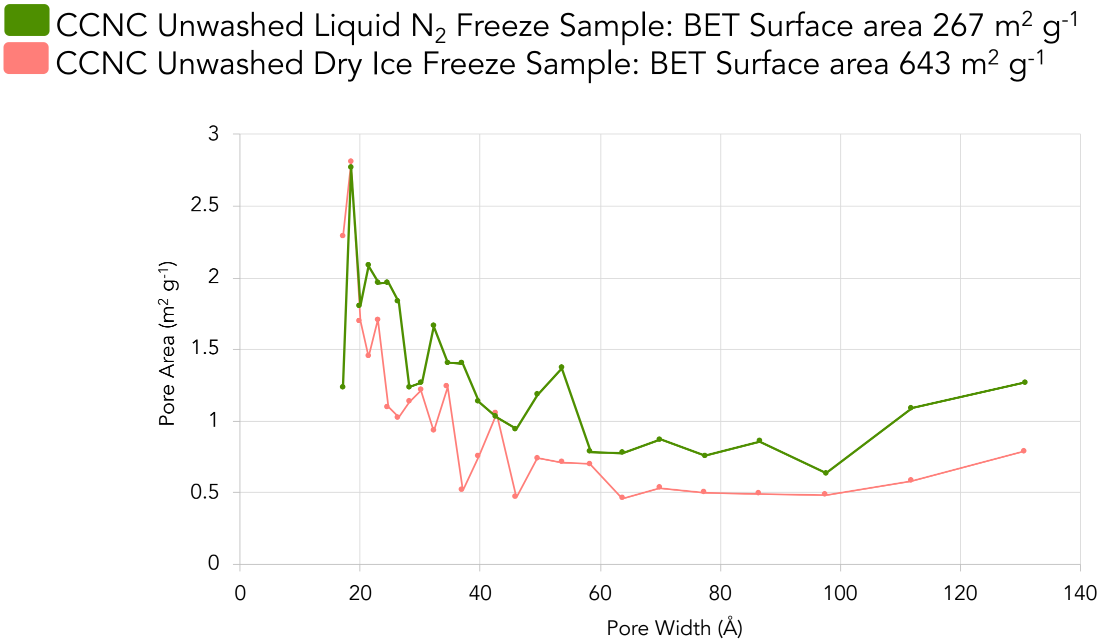

Figure 4.8 Pore Distribution of Liquid Nitrogen Frozen CCNC sample in green compared to dry Ice frozen sample in pink, both unwashed.

The liquid nitrogen frozen CCNC sample was also washed with DI water following the same procedure as the dry ice frozen sample to remove the sodium-based coating. Based on SEM images in **Figure 4.9**, it does appear that the coating is removed. Interestingly the very dense structure which we saw in **Figure 4.7b**, which we attributed to the coating is still present in the washed sample as evidence by **Figure 4.9c**. Indicating that the dense structure is not the result of the overlaying coating but is the result of the underlying denser carbon structure. The two more open structures seen in the unwashed sample (**Figure 4.7b-c**) are maintained in the washed sample, and are free of the sodium-based coating (**Figure 4.9d-e**).

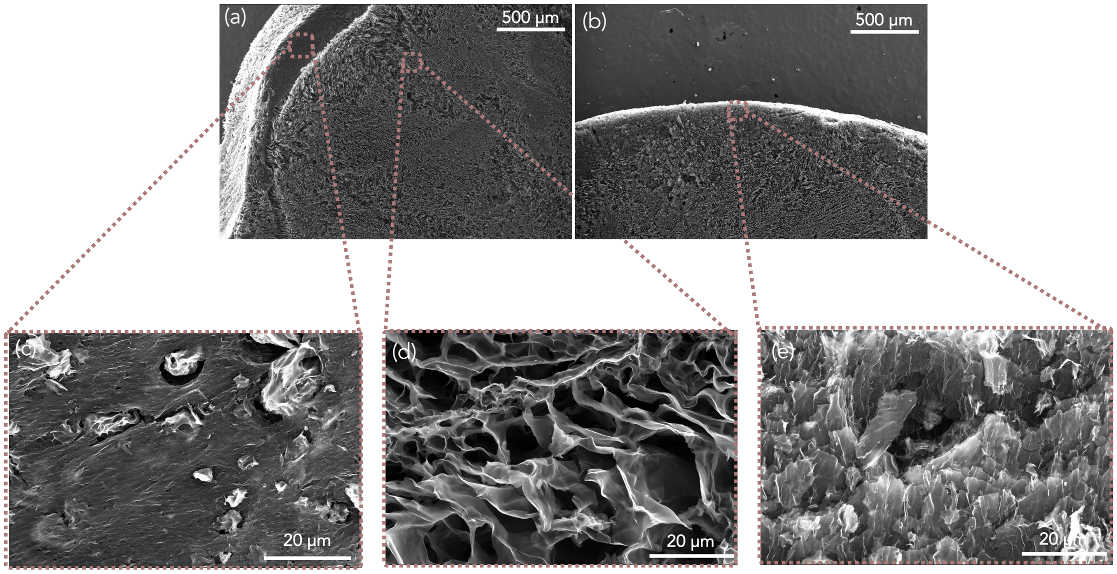

Figure 4.9. Washed Liquid Nitrogen Frozen Sample CCNC. (a,b) corresponds to 500 μm scale image (c-e) correspond to 20 μm images of the three regions of interest.

4.6.3 Effect of Structural Changes on CO_2 Uptake in CCNC Samples

Figure *4.10* compares CO_2 uptake for unwashed and washed dry ice and liquid nitrogen frozen CCNC samples. The unwashed samples contain the sodium-based surface coating. The unwashed dry ice frozen CCNC sample achieves a CO_2 uptake of 24 mg g^{-1} and 47 mg g^{-1} at 10 and 40 kPa respectively. The unwashed liquid nitrogen frozen CCNC sample achieves a CO_2 uptake of 33 mg g^{-1} and 64 mg g^{-1} at 10 and 40 kPa respectively. This difference in CO_2 uptake is achieved through alterations of the structure of the CCNC part by changing the freezing parameters. The CO_2 uptake trend does not correlate with BET surface area. The current data shows the dry ice frozen sample achieves a BET surface area of 643 m^2 g^{-1} while the liquid nitrogen frozen sample achieves a BET surface area 267 m^2 g^{-1}. Currently I do not have a clear explanation for this trend. It could be due to reasons discussed previously, the surface coating is inflating the surface area of the dry ice coated sample and/or the liquid nitrogen structure at the center of the part (**Figure *4.9*c**) is solid and reducing surface area. Further study is needed to investigate this trend. Next, the liquid nitrogen sample was washed with DI water in the same manner as the dry ice frozen sample. Based on SEM images the sodium-containing coating is removed from the liquid nitrogen washed sample (**Figure *4.9***). Preliminary data shows the washed liquid nitrogen sample achieved a CO_2 uptake of 30 mg g^{-1} and 69 mg g^{-1} at 10 and 40 kPa respectively. We do not see a significant change in CO_2 uptake performance between the washed and unwashed liquid nitrogen frozen sample. By comparison there is a large increase between unwashed and washed dry ice frozen CCNC samples from 24 mg g^{-1} to 35 mg g^{-1} at 10 kPa there is a larger increase at the 40 kPa pressure, increasing from 35 mg g^{-1} to 71 mg g^{-1}. Based on this result it indicates that the sodium-based coating has a more significant effect on the dry ice frozen sample. There is a small difference between the CO_2 uptake washed dry ice frozen sample compared to both washed and unwashed liquid nitrogen CCNC sample. It is unclear why the sodium-based coating does not have as significant effect on the CO_2 uptake in the nitrogen frozen sample compared to the dry ice frozen CCNC sample. Based on the CO_2 uptake results the sodium-based coating does not facilitate the CO_2 capture ability of the CCNC part.

The current CO_2 uptake data presented in **Figure *4.10*** shows that the use of liquid nitrogen to freeze the CCNC sample does improve the CO_2 uptake when the sodium-based coating is still present, when compared to the dry ice frozen CCNC samples. However, when the sodium-based coating is removed there is significant improvement in the CO_2 uptake of the dry ice frozen CCNC sample and the uptake becomes comparable to the liquid nitrogen frozen sample.

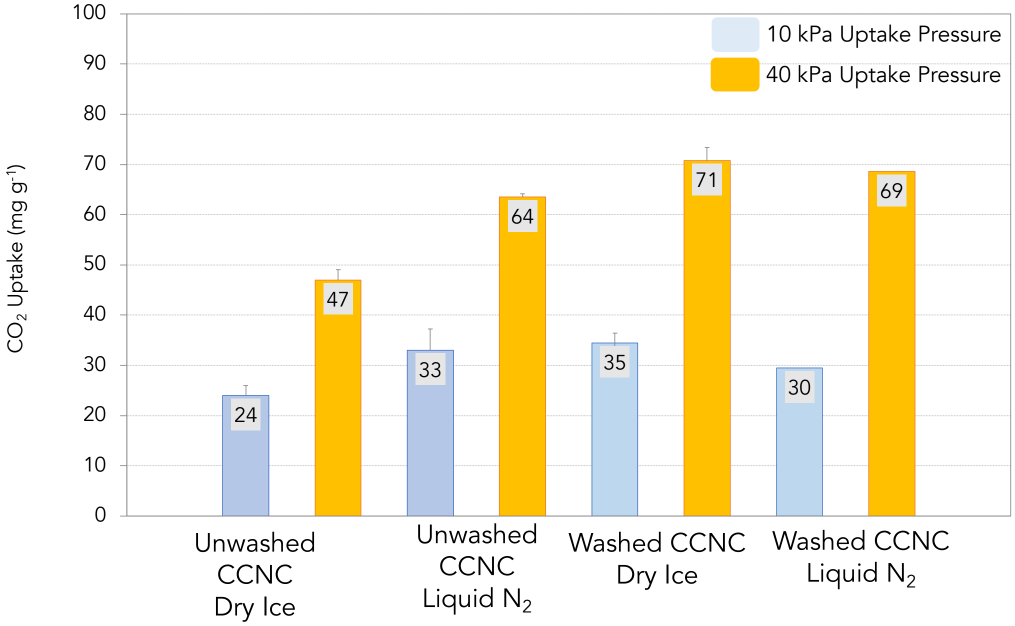

Figure 4.10. CO_2 Uptake for Washed and Unwashed Dry Ice and Liquid Nitrogen Frozen CCNC Samples at 10kPa and 40 kPa of Pressure at 25 °C.

4.7 Effect of Cellulose Precursor Particle Size on CO_2 Uptake

As previously stated in the introduction we utilized two different types of cellulose to formulate carbon materials for CO_2 uptake: nanocrystalline cellulose, which has a particle size with 2 to 10 nm in width and 80 to 150 nm in length, compared to a larger microcrystalline cellulose with a size distribution of 250 to 32 μm. To examine the effect the starting cellulose particle size has on the final surface area of the carbonized part, if smaller cellulose particles give rise to a higher final surface area and better CO_2 uptake. We conducted initial CO_2 uptake with dry ice frozen carbonized microcrystalline cellulose (AMCC) sample. In the SEM images it is apparent there is not a large amount of coating on the surface of the AMCC part, **Figure 4.11b** especially when compared to the initial surface coating that we see in the CCNC part (**Figure 4.4**). Washing the sample (following the same stringent wash procedures used for the CCNC sample) removes this small amount of surface coating, **Figure 4.11c**. Based on preliminary XPS data it is not immediately clear what this minor coating is (**Figure 4.11b**), if it is similar to the one seen in the CCNC sample. Preliminary XPS data only shows carbon and oxygen species which is expected when looking at carbon materials (**Table 4.1**). This coating though does appear to have a minor effect on the performance on the CO_2 uptake ability of dry ice frozen AMCC samples. **Figure 4.11a** shows the CO_2 uptake of both washed and preliminary data for the unwashed dry ice frozen AMCC samples. There is a minor difference in the CO_2 uptake between the two samples at both 10 kPa and 40 kPa pressure. With unwashed AMCC samples achieving CO_2 uptake of 24 mg g^{-1} and 55 mg g^{-1} and 10 kPa and 40 kPa respectively, while washed AMCC sample achieved 23 mg g^{-1} and 51 mg g^{-1} at 10 kPa and 40 kPa respectively (**Figure 4.11a**). Based on CO_2 uptake data the surface coating we see in the SEM has a minor effect on the CO_2 uptake of the AMCC sample. The CO_2 uptake achieved for the unwashed dry ice frozen AMCC sample is higher than that of the unwashed dry ice frozen CCNC sample, **Figure *4.5*a**. However, when the sodium-based coating is removed from the CCNC sample the CO_2 uptake is improved past that of the AMCC sample for both washed and unwashed samples. Indicating that when the carbon surface area is fully exposed, a smaller starting cellulose particle size is beneficial for CO_2 uptake in the final part.

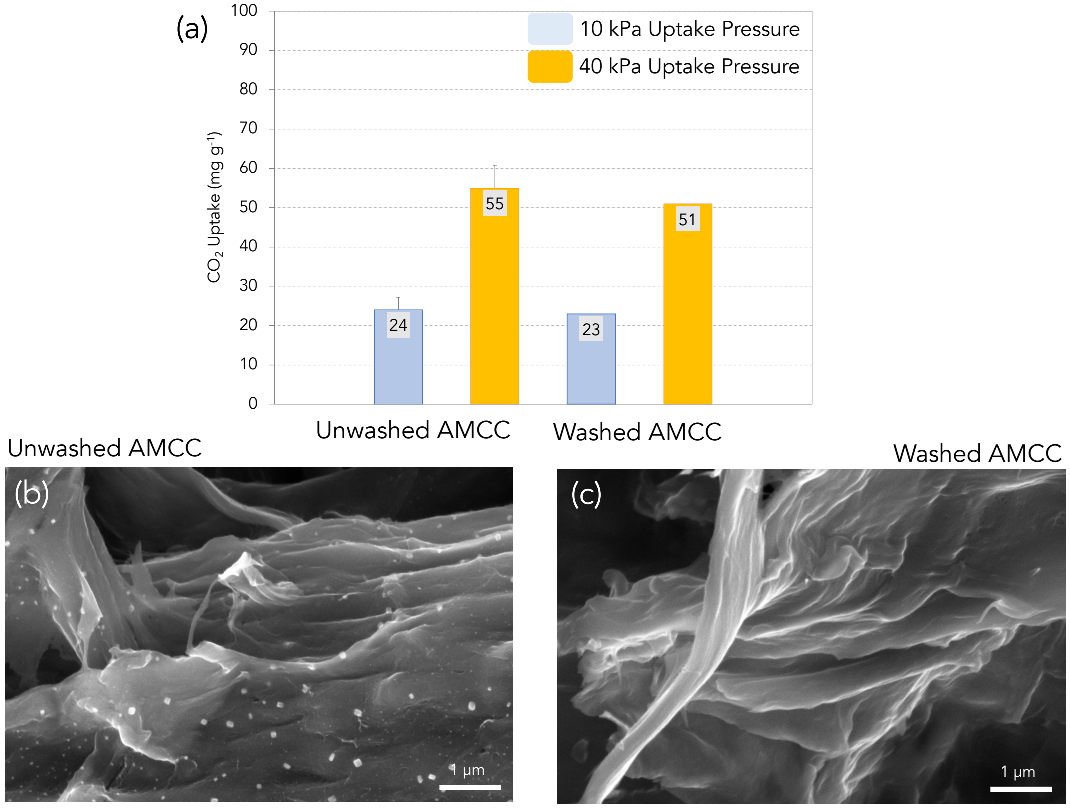

Figure 4.11 CO_2 Uptake Data for Unwashed and Washed AMCC Sample Frozen with Dry Ice, Corresponding SEM Images. (a) shows the initial uptake data for 10 kPa in blue and 40 kPa in yellow. (b) shows an unwashed AMCC sample, while (c) shows a washed AMCC sample.

4.8 Effect of Structure on CO_2 Uptake in AMCC Sample

Investigation was made into the effect different freezing methods on the structure of AMCC samples. **Figure 4.12** shows a comparison between SEM images of dry ice frozen AMCC sample (**Figure 4.12a**) and the liquid nitrogen frozen AMCC sample (**Figure 4.12b**). Through comparison of these two images it appears that there is not a drastic difference in the structure between the two different freezing methods especially when compared to the difference seen in the CCNC sample in **Figure 4.6** and **Figure 4.9**. The larger particle size of the AMCC starting material could affect the structure during freezing. Large particles minimize the amount of nucleation sites available for ice crystal formation leading to larger ice crystals, also it is harder to form fine features due to the limited mobility of larger particles. [22] Thus the large particle size of the AMCC starting material could mitigate the effect of the different freezing methods.

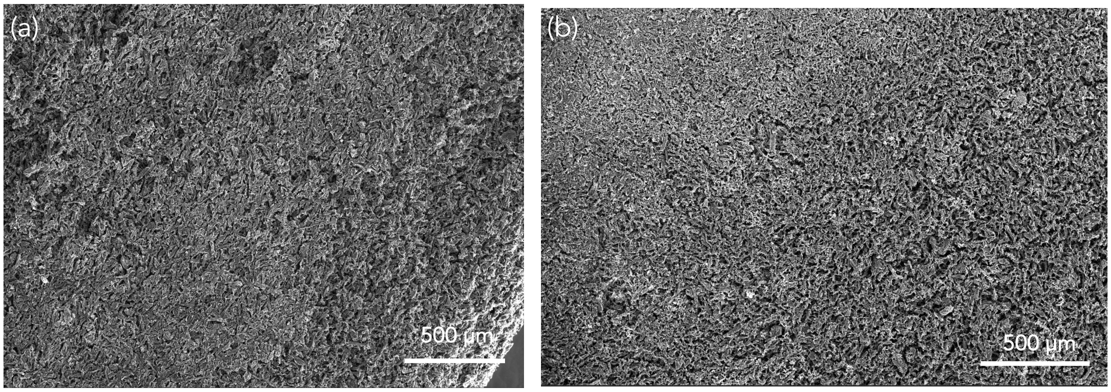

Figure 4.12 SEM Images Comparing (a) Dry Ice Frozen AMCC sample and (b) liquid nitrogen frozen sample.

BET surface area was collected for both the dry ice and liquid nitrogen frozen AMCC samples, the dry ice sample achieved a BET surface area of 300 m^2 g^{-1} and the liquid nitrogen frozen sample achieved a BET surface area of 104 m^2 g^{-1}. The BJH pore distribution seen in **Figure 4.13** shows that the dry ice frozen AMCC sample has very narrow pore size distribution 17 and 25 Å. The pore distribution is much broader for the liquid nitrogen frozen sample (**Figure 4.13**). Based on these BJH pore distribution between dry ice and liquid nitrogen frozen AMCC sample it appears that there is a drop in pore area in this range. This could be contributing to the lower overall BET surface area of the liquid nitrogen frozen AMCC sample. The surface area for the unwashed dry ice frozen (643 m^2 g^{-1}) and liquid nitrogen frozen (267 m^2 g^{-1}) CCNC samples are higher than the surface area for unwashed dry ice frozen (300 m^2 g^{-1}) sample and liquid nitrogen frozen (104 m^2 g^{-1}) AMCC samples indicating that the starting with a smaller cellulose particle size provides a higher surface area for the final material.

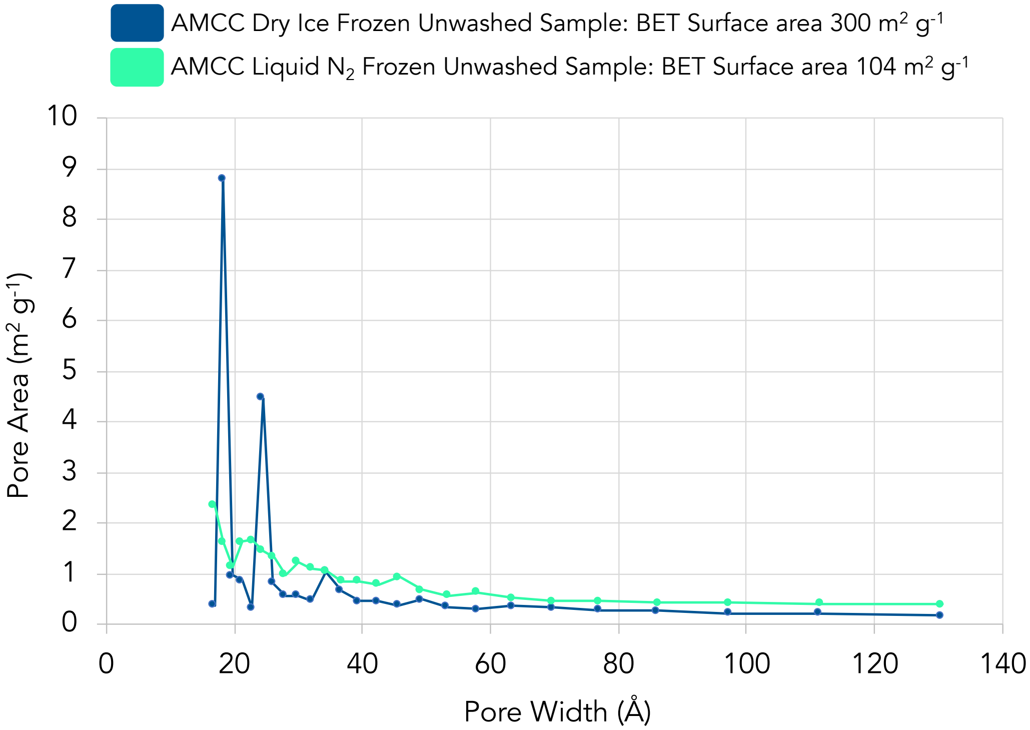

Figure 4.13 BET surface area and BJH pore size distribution for a comparison of dry ice and liquid nitrogen frozen AMCC samples

We conducted initial CO_2 uptake experiments using the AMCC samples (**Figure 4.14**). The CO_2 uptake agrees with the BET surface area. With the liquid nitrogen frozen sample, which exhibits the lower surface area, yielding the lower CO_2 uptake compared to the higher surface area dry ice frozen sample. The unwashed dry ice frozen sample yields a CO_2 uptake of 24 mg g^{-1} and 55 mg g^{-1} at 10 kPa and 40 kPa respectively, while the unwashed liquid nitrogen frozen sample exhibits a CO_2 uptake of 20 and 47 mg g^{-1} at 10 kPa and 40 kPa respectively. Indicating that using liquid nitrogen to introduce a narrower pore size in AMCC sample was not effective to improve the CO_2 Uptake ability of the sample.

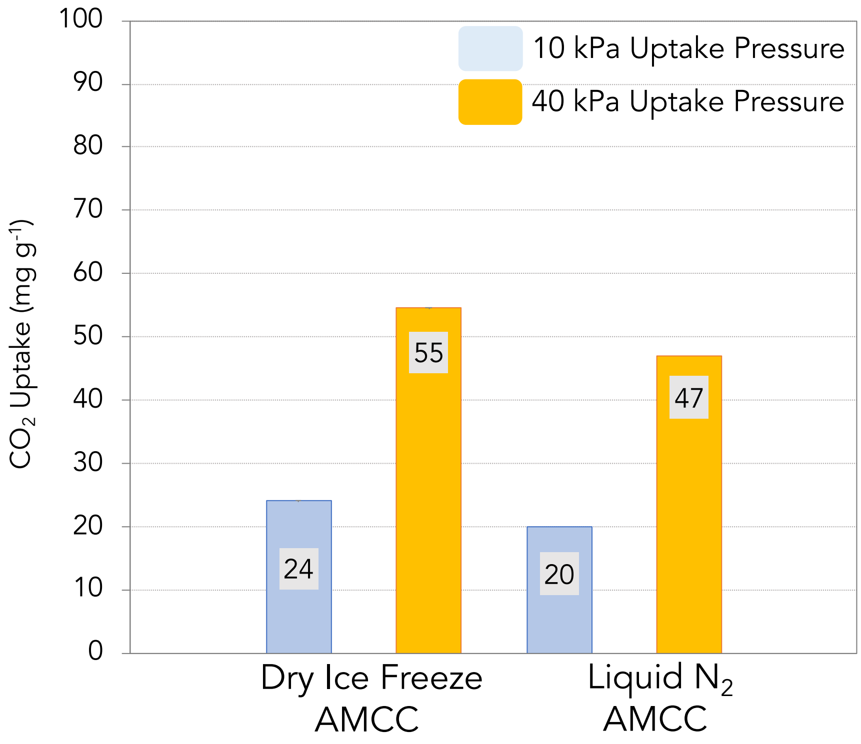

Figure 4.14 CO_2 Uptake Comparison Between Unwashed Dry Ice and Liquid Nitrogen Frozen AMCC sample.

4.9 XPS Characterization of AMCC and CCNC Samples

Based on XPS data and the corresponding CO_2 uptake data it does not appear that the oxygen content is the key component for the CO_2 capture mechanism for these cellulose-based carbon materials (**Table 4.1**). The current data suggests the mechanism appears to be a function of exposed carbon surface area allowing for electrostatic interactions between the carbon surface and the CO_2 molecule. The sample which exhibits the best CO_2 uptake, washed dry ice frozen CCNC sample, has lower oxygen content when compared to the unwashed CCNC sample. The sodium content in the CCNC sample also appears to be linked to the oxygen content, after the sample is washed there is drop in oxygen content. The oxygen content of the AMCC sample is also similar the CCNC washed sample, while the CO_2 uptake is lower for the AMCC sample. This further indicates that oxygen content is not a main component for the CO_2 uptake mechanism in the CCNC sample, but rather exposed carbon surface area.

Table 4.1 XPS data for CCNC and AMCC samples

Sample (all frozen with dry ice)	Carbon (at %)	Oxygen (at %)	Sodium (at %)	CO_2 Uptake (10 kPa, mg g^{-1})	CO_2 Uptake (40 kPa, mg g^{-1})
CCNC No Wash	63.36	21.10	15.54	24	47
CCNC Washed	86.78	9.98	-	35	71
AMCC Non Wash	95.09	4.91	-	24	55

Sample (all frozen with dry ice)	C-O (at %)	C=O (at %)	O-C=O (at %)	O= (at %)	OH- (at %)	H_2O (at %)	Na (at %)
CCNC No Wash	20.91	-	8.87	6.33	13.08	1.69	15.54
CCNC Washed	21.44	6.62	3.10	5.76	3.76	0.81	-
AMCC No Wash	19.05	4.42	3.13	2.73	1.91	0.43	-

4.10 Conclusions and Proposed Future Work

In this work we have demonstrate some preliminary results on building cellulose-based carbon monoliths for CO_2 uptake. The cellulose starting material do not undergo any further chemical modification before carbonization treatments. Two cellulose materials with different particle sizes were examined: nanocrystalline cellulose (CCNC) and microcrystalline cellulose (AMCC). Based on the current results the CO_2 uptake of these materials is influenced by the carbon surface area exposed for CO_2 interaction and the smaller particle size of the starting cellulose material is more advantageous for CO_2 uptake.

In the CCNC part we found that a large amount of a sodium containing coating forms on the surface of the final carbonized part. This coating can be easily removed with a water and mild acid wash. The coating found on the surface of the CCNC parts has a significant influence on CO_2 uptake. By removing it and further opening the carbon surface we can improve the CO_2 uptake.

We have demonstrated some initial exploration into further structural manipulations through different freezing methods. We conducted a comparison between a slower dry ice freezing method and flash freezing method using liquid nitrogen, for both CCNC and AMCC samples. For the CCNC sample specifically we can see that the liquid nitrogen freezing does produce a denser structure compared to that of the dry ice frozen sample. However, this does not translate to the BET surface area. This could potentially be the result of a solid carbon structure forming at the center of the liquid nitrogen frozen CCNC sample. The AMCC part did not see as significant change between dry ice and liquid nitrogen freezing. Potentially this could be that the larger particle size in the AMCC starting material is not as affected by the ice templating provided by the different freezing methods.

Further work needs to be done to explore the effect that different freeze casting templating methods provide to the internal structure of the cellulose-based carbon monolith, and the effect these structural changes have on CO_2 uptake. This could be done by utilizing temperature ramping on the freeze rate to introduce more control over ice templated structure. Removing the salt from the nanocrystalline cellulose starting material before freezing and carbonization to see if this effects the structure.

Further work also needs to be done to explore the selectivity of the carbon material of CO_2 over other gaseous components commonly found in CO_2 point sources. For flue gas capture systems, it is important to understand the viability of the capture system in the presence of humidity and oxygen.

4.11 Reference

1. Lindsey, R. 2021; **Climate Change: Atmospheric Carbon Dioxide** E. Dlugokencky, ed. (NOAA Climate.gov).
2. H.-O. Pörtner, D.C.R., E.S. Poloczanska, K. Mintenbeck, M. Tignor, A. Alegría, M. Craig, S. Langsdorf, S. Löschke, V. Möller, A. Okem 2022; **IPCC, 2022: Summary for Policymakers**. In *Climate Change 2022: Impacts, Adaptation, and Vulnerability*. Contribution of Working Group II to the Sixth Assessment Report of the Intergovernmental Panel on Climate Change. (Cambridge University Press).

3. Rasi, S., Veijanen, A., and Rintala, J. **Trace compounds of biogas from different biogas production plants**. Energy. 2007; **32:** 1375-1380.

4. Collet, P., Flottes, E., Favre, A., Raynal, L., Pierre, H., Capela, S., and Peregrina, C. **Techno-economic and Life Cycle Assessment of methane production via biogas upgrading and power to gas technology**. Applied Energy. 2017; **192:** 282-295.

5. Zevenhoven, R., Kilpinen, P. 2001; **Chapter 2 Flue gases and fuel gases**. In Control of pollutants in flue gases and fuel gases. (Web).

6. Rao, A.B., and Rubin, E.S. **A Technical, Economic, and Environmental Assessment of Amine-Based CO2 Capture Technology for Power Plant Greenhouse Gas Control**. Environmental Science & Technology. 2002; **36:** 4467-4475.

7. Samanta, A., Zhao, A., Shimizu, G.K.H., Sarkar, P., and Gupta, R. **Post-Combustion CO2 Capture Using Solid Sorbents: A Review**. Industrial & Engineering Chemistry Research. 2012; **51:** 1438-1463.

8. Ma, X., Yang, Y., Wu, Q., Liu, B., Li, D., Chen, R., Wang, C., Li, H., Zeng, Z., and Li, L. **Underlying mechanism of CO_2 uptake onto biomass-based porous carbons: Do adsorbents capture CO_2 chiefly through narrow micropores?** Fuel. 2020; **282:** 118727.

9. Sharma, A., Thakur, M., Bhattacharya, M., Mandal, T., and Goswami, S. **Commercial application of cellulose nano-composites – A review**. Biotechnology Reports. 2019; **21:** e00316.

10. Trache, D. 2016; **Microcrystalline cellulose and related polymer composites: Synthesis, Characterization and Properties**. In Handbook of Composites from Renewable Materials, Structure and Chemistry, V.K. Thakur, M.K. Thakur and M.R. Kessler, eds. (Wiley).

11. Tang, Y., Yang, H., and Vignolini, S. **Recent Progress in Production Methods for Cellulose Nanocrystals: Leading to More Sustainable Processes**. Advanced Sustainable Systems. 2022; **6:** 2100100.

12. Rouquerol, J., Llewellyn, P., and Rouquerol, F. **Is the BET equation applicable to microporous adsorbents**. Stud. Surf. Sci. Catal. 2007; **160:** 49-56.

13. Casco, M.E., Martínez-Escandell, M., Silvestre-Albero, J., and Rodríguez-Reinoso, F. **Effect of the porous structure in carbon materials for CO2 capture at atmospheric and high-pressure**. Carbon. 2014; **67:** 230-235.

14. Geng, S., Wei, J., Jonasson, S., Hedlund, J., and Oksman, K. **Multifunctional Carbon Aerogels with Hierarchical Anisotropic Structure Derived from Lignin and Cellulose Nanofibers for CO2 Capture and Energy Storage**. ACS Applied Materials & Interfaces. 2020; **12:** 7432-7441.

15. Wang, R., Wang, P., Yan, X., Lang, J., Peng, C., and Xue, Q. **Promising Porous Carbon Derived from Celtuce Leaves with Outstanding Supercapacitance and CO2 Capture Performance**. ACS Applied Materials & Interfaces. 2012; **4:** 5800-5806.

16. Estevez, L., Barpaga, D., Zheng, J., Sabale, S., Patel, R.L., Zhang, J.-G., McGrail, B.P., and Motkuri, R.K. **Hierarchically Porous Carbon Materials for CO2 Capture: The Role of Pore Structure**. Industrial & Engineering Chemistry Research. 2018; **57:** 1262-1268.

17. Ma, X., Li, L., Zeng, Z., Chen, R., Wang, C., Zhou, K., and Li, H. **Experimental and theoretical demonstration of the relative effects of O-doping and N-doping in porous carbons for CO2 capture**. Applied Surface Science. 2019; **481:** 1139-1147.

18. Sevilla, M., and Fuertes, A.B. **Sustainable porous carbons with a superior performance for CO2 capture**. Energy & Environmental Science. 2011; **4:** 1765-1771.

19. Zhou, J., Li, Z., Xing, W., Shen, H., Bi, X., Zhu, T., Qiu, Z., and Zhuo, S. **A New Approach to Tuning Carbon Ultramicropore Size at Sub-Angstrom Level for Maximizing Specific Capacitance and CO2 Uptake**. Advanced Functional Materials. 2016; **26:** 7955-7964.

20. Lavoine, N., and Bergström, L. **Nanocellulose-based foams and aerogels: processing, properties, and applications**. Journal of Materials Chemistry A. 2017; **5:** 16105-16117.

21. Munier, P., Gordeyeva, K., Bergström, L., and Fall, A.B. **Directional Freezing of Nanocellulose Dispersions Aligns the Rod-Like Particles and Produces Low-Density and Robust Particle Networks**. Biomacromolecules. 2016; **17:** 1875-1881.

22. Li, W.L., Lu, K., and Walz, J.Y. **Freeze casting of porous materials: review of critical factors in microstructure evolution**. International Materials Reviews. 2012; **57:** 37-60.

5 Reactive Capture: Integration of Carbon Capture and Conversion

5.1 Abstract

Carbon dioxide (CO_2) capture and CO_2 conversion have traditionally been treated as distinct application areas with non-overlapping research programs. However, the integration of capture and conversion processes presents an opportunity to eliminate energy penalties, costs, and logistical hurdles inherent in the separation of CO_2 from mixed gas streams, regeneration of the capture material/solvent, compression of CO_2, and transport to a conversion facility. By integrating the two processes, which we term "reactive capture", CO_2 can be separated from a mixed gas stream and converted to valuable products using process steps that eliminate sorbent regeneration, CO_2 compression, and transportation. Here, we describe recent rapid progress, current understanding, and state-of-the-art performance metrics with comparisons between reactive capture technologies. We highlight the need for 1) standardized performance metrics for reporting and technical viability, 2) tailoring and demonstrating reactive capture technologies for a particular CO_2 source, and 3) ensuring that reactive capture outperforms separated capture and conversion in carbon and energy balance as key needs to move this field of research forward.

5.2 Introduction

The development, scale-up, and deployment of technologies that mitigate or remove CO_2 from the atmosphere is becoming more urgent.[1] Global CO_2 emissions are currently estimated to be ~35 billion tons per year.[2] Greenhouse gas mitigation strategies, such as renewable energy, transportation electrification, and energy efficient buildings, have been implemented to reduce CO_2 emissions. However, these tactics do not address the need to replace fossil carbon feedstocks, which are responsible for about 2 billion tons of annual fossil CO_2 emissions.[3] CO_2 could serve as a starting material in combination with increasingly abundant renewable electrical energy to produce valuable carbon feedstocks for the creation of a new carbon economy. For example, 156 million metric tons (MMT) of ethylene are produced each year primarily using fossil-derived oil and gas as carbon sources, emitting 258 MMT of CO_2 per year through traditional petrochemical production.[4] Yet, ethylene production could utilize 490 MMT of CO_2 as the carbon precursor if research and industrial communities can invent effective and efficient ways to recycle CO_2.[5] However, many major challenges must be overcome, including the high cost and energy intensity of CO_2 capture and conversion processes relative to conventional production of carbon-based chemicals.

To date, CO_2 capture and conversion are typically treated as separate processes **Figure 5.1,** increasing the capital and operational costs of carbon utilization. Regeneration of carbon capture sorbents and solvents is an energy intensive process, with capture and regeneration of sorbents requiring between 60 and 120 kJ/mol of energy; further compression of the CO_2 requires around 12 kJ/mol. Additional energy must then be added to convert the captured and compressed CO_2 to useful products, diminishing the overall lifecycle benefits of utilizing captured CO_2. In contrast, in reactive capture (RC) processes, the energy introduced to produce products also regenerates the capture sites. We define RC as the coupled and integrated process of capturing CO_2 from a mixed gas stream and converting it to valuable products. Importantly, RC occurs in one platform, which should streamline CO_2 recycling and reduce capital and operational costs (*e.g.,* by eliminating the need for energy intensive sorbent regeneration, CO_2 compression, transportation and associated capital costs). The successful advancement and implementation of RC technologies will open new opportunities for both CO_2 producers and CO_2 conversion industries to reduce emissions and create valuable products, maximizing the potential of the circular carbon economy.

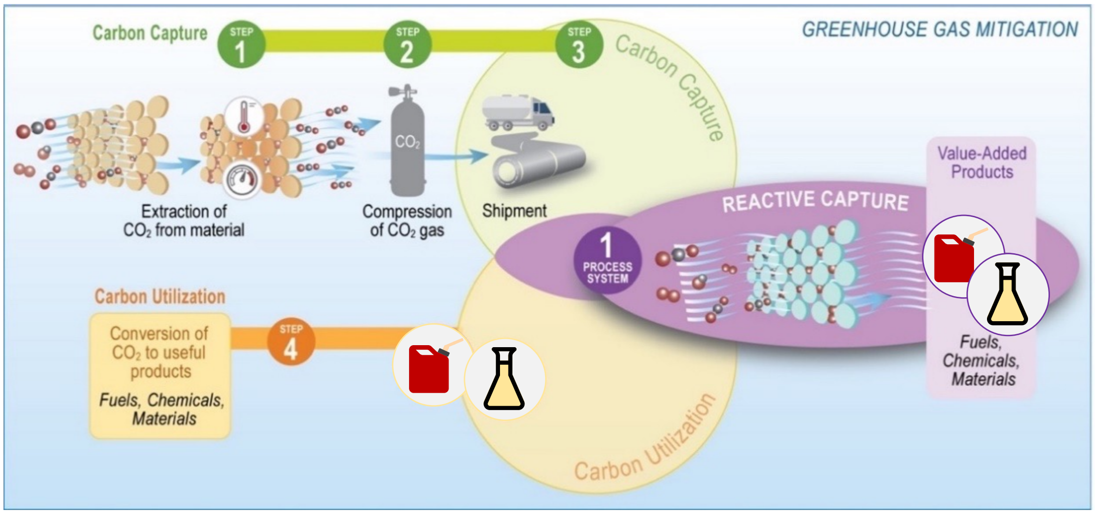

Figure 5.1 Comparison between separate capture and conversion versus reactive capture system.

RC is an emerging research area that spans a broad range of strategies, materials, and chemical pathways, working toward the common goal of integrating CO_2 separation and conversion. We will categorize and present a concise review of current research areas and an assessment of research needs. Our major findings are: 1) there is an urgent need to unify experimental testing standards, protocols, and benchmarks across the diverse range of technologies so that progress can be measured and compared; 2) Individual RC technologies should be developed toward a target CO_2 source so that materials and process development can be optimized appropriately, with consideration for scale, selectivity and contaminant tolerance, among other considerations; 3) Nascent RC technologies must have a path toward favorable overall energy efficiency and carbon efficiency relative to the separate capture and conversion processes.

5.3 Reactive Capture Overview

RC is at a very early stage; most published studies have presented basic proof-of-concept demonstrations of potential integration of capture and conversion separately while highlighting the future potential of RC technologies, and very few have demonstrated separation from a mixed CO_2 source and conversion in an integrated process. We have organized reported demonstrations of RC into three broad categories according to conversion reaction requirements to concisely describe the basic strategies to achieve RC in a single process. These categories are electrochemical methods, thermal methods, and biological methods. We summarize these technologies and show their categorical mapping and associated materials requirements in **Figure 5.2**.

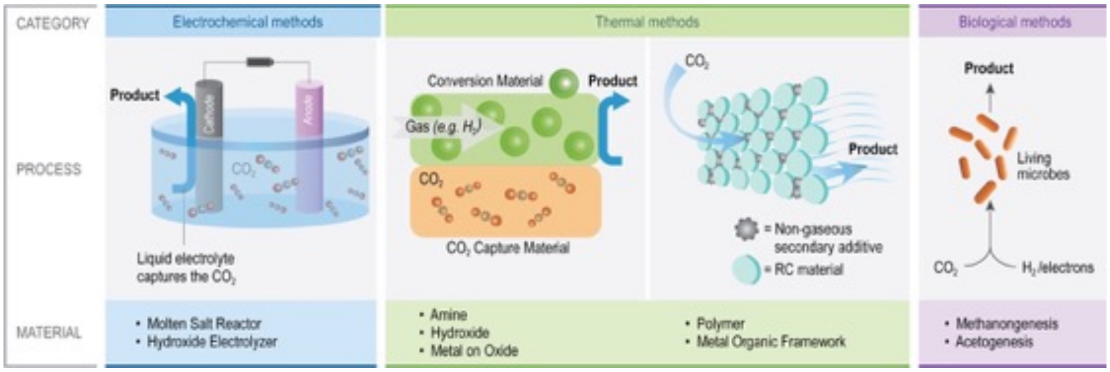

Figure 5.2 Schematic illustrations of three RC categories discussed, helping to show in broad strokes where CO2 is capture and then subsequently converted.

5.3.1 Electrochemical Reactive Capture Strategies

We broadly categorized RC technologies as "electrochemical" that separate CO_2 from mixed gas streams using a CO_2-selective electrolyte and electrochemically convert captured CO_2 to more reduced products. Within the electrochemical category, reactive capture and conversion can span a wide operational parameter and material (*e.g.,* catalyst, product). For example, CO_2 may first be captured by a high temperature molten salt (*e.g.,* Li_2O)[6,7] or target a low temperature hydroxide (*e.g.,* KOH) [8,9] electrolyte as the capture solution and then electrochemically reduced at the cathode to desired products, including carbon monoxide (CO)[9] and solid carbon materials.[8,9] In an ideal electrochemical RC system, the capturing electrolyte will be regenerated by the electrochemical conversion process at the cathode and anode, with minimal losses and degradation to the capture medium.

5.3.2 Thermal Reactive Capture Strategies

Thermal methods utilize a CO_2 sorbent material or solvent to capture CO_2 and expose it to a secondary reactant in gas or liquid phase and a catalytic site to convert the captured CO_2 to the desired products. The most commonly used gas is hydrogen[10-15] while the most common liquid additives are epoxides[16-25]. For thermal RC systems, the site of CO_2 sorption must be brought into close proximity to the catalytic site for CO_2 conversion. Processes that react the captured CO_2, rather than simply requiring CO_2 desorption in the presence of the conversion site, may be able to take advantage of the altered atomic and electronic configuration of bound CO_2 compared to a conversion process that uses molecular CO_2. This can be accomplished by tethering the sorption and conversion site onto the same solid material, as is the case for metal on oxide materials[15, 26-31] or by performing both processes in the liquid phase, as is the case for amine and hydroxide solutions with dissolved organometallic catalysts[10-13,32-36]. Highly porous solid sorbent and catalytic materials, such as porous polymers[16,21] and metal-organic frameworks,[22,24,37] may be dispersed in a liquid that contains a secondary reactant, such as an epoxide. Potential advantages of thermal RC processes are the ability to use the heat from high temperature, post-combustion CO_2 streams, if the capture and conversion processes can both be performed at elevated temperature, and the fact that the conversion methods are most similar to traditional chemical manufacturing that have been proven at scale. However, many capture chemistries perform better at lower temperature due to exothermic sorption, necessitating development of temperature swing processes that operate between capture and conversion temperature, or new materials that perform well for both capture and conversion at some intermediate elevated temperatures.

5.3.3 Biological Reactive Capture Strategies

Biological RC strategies utilize highly selective microbes such as methanogens and acetogens to accomplish both the CO_2 capture and conversion to products.[38-49] While hydrogen can be the source of reducing equivalents to further convert captured CO_2 to the desired product, direct electron transfer of electrons from a biocathode, where microbes are in direct contact with the electrode surface has also been demonstrated.[50] An exemplary strategy for biological RC is the conversion of biogas, which contains primarily CO_2 and methane, into a purified methane stream that needs little additional treatment to make it suitable for downstream utilization. Alternatively, RC can be achieved using biological strategies by converting the gaseous reactants to liquid products, allowing the inert constituents of the mixed gas stream to exit the bioreactor. Advantages of biological strategies include low process complexity that arises from the use of mature stirred tank fermenters and near ambient operating conditions, and the use highly selective and self-replicating biocatalysts that can be engineered to generate a range of products. However, mass transfer of gas phase species to biocatalysts in liquid can hinder productivity, and often the biocatalysts require specific physiological operating conditions to maintain their viability. While trees, plants, and algae are the original “reactive capture” demonstrations, we do not consider photosynthetic processes in this discussion.

5.4 Reactive Capture Strategies: CO_2 affinity and target sources

Figure *5.3* shows some of the major CO_2 sources appropriate for RC. Tailoring the RC system to a specific CO_2 source is important to ensure the RC system can perform optimally with the concentration of CO_2 found in the specific CO_2 source, and the system is compatible and stable in the presence of other components of the CO_2 source.

5.4.1 Direct Air Capture

The ability to react and convert CO_2 directly from air has several attractive aspects, including the flexibility to locate the process anywhere, for example, close to renewable energy sources or customers/transportation systems for product offtake. Additionally, products made from air derived CO_2 can have significantly lower carbon intensity, and if long-lived products are produced, the process can be categorized as net carbon dioxide removal. However, the 2-3 orders of magnitude lower concentration of CO_2 in air than most point sources (0.04% *vs.* 4-40%) means that RC technologies aiming to achieve direct air capture, must have exceptional CO_2 selectivity over other common components of air, primarily N_2 and O_2. Also, large volumes of air must be moved over the capture material, putting special requirements upon sorbent surface area and reactor configurations with low pressure drop.

Several RC materials and processes are compatible in principle with conversion of air CO_2. For example, oxides and carbonates in the form of molten salt (*e.g.,* Li_2O),[7,51] have been demonstrated to directly capture CO_2 from the air at high temperatures (450 – 850 °C), forming the carbonate salts. This is an attractive option for RC because the oxide material is able to capture and greatly increase the CO_2 concentration near catalytic sites.[7] The secondary gases found in air, mainly N_2 and O_2 also have a minimal effect on the molten salt capture material.

Additionally, amine and hydroxide based RC sorbents have sufficient selectivity for air capture, operating at milder conditions and being demonstrated directly with air or simulated air. In the amine-based RC system, CO_2 is captured by an amine to form an intermediate, which is then reacted with hydrogen gas via organometallic catalysis to generate desired products. Amines can be freely distributed within an alcohol or aqueous solution[12,13,32-34] or sequestered to a polymer or silica support[35,36]. The conversion material is also distributed in solution phase allowing the amine material laden with CO_2 to contact the conversion material. Alternatively, CO_2 can be captured using alkali hydroxides. Prakash *et al.* screened multiple alkali hydroxide salts (*e.g.,* NaOH, KOH, LiOH, CsOH, and $Ca(OH)_2$) for their CO_2 capture affinity. NaOH and KOH were identified as the best candidates for CO_2 capture based on CO_2 uptake and cost.[11]

5.4.2 Flue Gas

Industrial sources can contain from about 4 – 98 % CO_2 that is either derived from petroleum (natural gas, coal 4-12% CO_2) or biogenic (biogas, corn fermentation 40-98% CO_2). From an energy and capital cost perspective, drawing down industrial, more concentrated sources of CO_2 first can enable smaller, more energy efficient and less costly RC technologies relative to RC tailored to air capture due to the ability to process smaller gas volumes with a larger driving force for CO_2 capture. Important considerations in tailoring RC for industrial gas streams include the ability to tolerate high temperature gas at the inlet (*e.g.*, 150-260 °C for natural gas fired power plants) as well as contaminants such as SO_x and NO_x (from combustion of fossil fuels) or H_2S (from biogas). CO_2 is captured via both chemi- and physisorption processes. Physisorption through van der Waals interactions has a lower heat of adsorption, it leads to the sorption of other gases such as N_2. Chemisorption is more selective for CO_2 sorption, but sometimes the absorption materials can be poisoned by contaminants in the flue gas such as SO_2.[31]

Researchers are developing metal on oxide thermal systems specifically to target flue gas as a point source of CO_2. While no metal on oxide system has been tested in the presence of NO_x and SO_x species, testing has been done in the presence of oxygen and moisture[15,52] to test the longevity of the metal on oxide material in the presence of the oxidizing environment. Duyar et al. tested a Ru on nanodisperesed CaO supported on γ-Al_2O_3 carrier material used to generate methane, for 20 cycles (each 40 mins in length) in the presence of two CO_2 source gas consisting of 10%CO_2/air and 8% CO_2/21 % H_2O/air. For the metal on oxide material tested in both CO_2 streams there was a similar reduction in Ru conversion centers (about 20%), however the was a significantly larger decrease in CaO capture material for the sample exposed to steam, 87% compared to 20% in sample only exposed to air. The larger decrease in CaO in the presence of steam was attributed to sintering.[15] Despite the decrease in both Ru conversion sites and CaO capture material the methane generation of the 5% Ru, 10% CaO/γ-Al_2O_3 under both CO_2 gas sources was stable and similar at about 300 μ-mol over the 20 cycles. Duyar et al attribute this observation to the loss of excess CaO absorption sites. And though there is some loss of Ru conversion sites due to oxidation, the performance of the 5% Ru, 10% CaO/γ-Al_2O_3 is still better than materials which contain only Ru supported on γ-Al_2O_3 indicating CaO plays a critical role in the performance of the RC material.[15] This potential for common flue gas contaminants to diminish the RC performance further emphasizes the importance to test materials in a practical operation conditions. While it is very useful to understanding the survivability of the metal on oxide materials in the presence of oxygen and steam, it is also critical to understand how CO_2 will compete secondary species such as: NO_x and SO_x, on adsorption and catalytic sites, and how these components may further influence the lifetime of the RC materials.

5.4.3 Preliminary Reactive Capture Testing

At this early stage, several technologies have yet to be tested directly on mixed gas streams, but still merit consideration and further development. Promising RC systems that have yet to be extensively validated directly using mixed gas streams include polymer, MOF, and biological approaches. [16] [17] [23] [24] [38] [39] Instead of direct measurement of capture and conversion from mixed gas streams, absorption isotherms are compared under pure CO_2 and pure N_2 conditions followed by calculations to determine selectivity of CO_2 over N_2. Typically, at higher temperatures the calculated CO_2 selectivity compared to N_2 decreases.[53] Though these technologies have not been demonstrated on mixed gas sources they still provide interesting beginning strategies for CO_2 capture from flue gas and air. Strategies that researchers have used to confer selectivity to CO_2 include adding sites for physisorption and chemisorption. Physisorption CO_2 uptake rate and capacity of MOF polymer-based RC systems are determined by the porous structure and the type and prevalence of surface functional groups. For polymers pore sizes less than 2 nm in diameter are most commonly sought to increase CO_2 uptake.[17,54] Chemisorption is found to help improve uptake rates and selectivity of CO_2. In polymer-based RC systems functional groups are often negatively charged and contain nitrogen to improve chemisorption.[17,18,54] In MOF-based RC systems chemisorption through functional groups found on the organic ligand in the MOF, such as sulfonate functional groups[23], and nitrogen containing groups.[22] In comparison to physisorption, chemisorption can facilitate selective CO_2 uptake at low pressure.[22] For example, by increasing the open metal sites and Lewis basic sites, a recently developed Cu(II) MOFs achieved a high volumetric uptake (171 $cm^3\ cm^{-3}$) of CO_2 under ambient conditions (298 K, 1 atm), with excellent selectivity for CO_2 over N_2.[22] Finally, methanogens and acetogens RC systems have been demonstrated using pure CO_2 and a few systems using a mixed gas of CO_2 and N_2. This provides biological systems with excellent selectivity as long as the microbes can survive any contaminants in the CO_2 source. Methanogens and acetogens operate best in anaerobic conditions, this maybe a hinderance for CO_2 sources which contain large amounts of oxygen such as air. Though preliminary selectivity data has been gathered for these technologies it is still critical for them to be tested with mixed gas sources containing the percentage of CO_2 which will be present in the real point source.

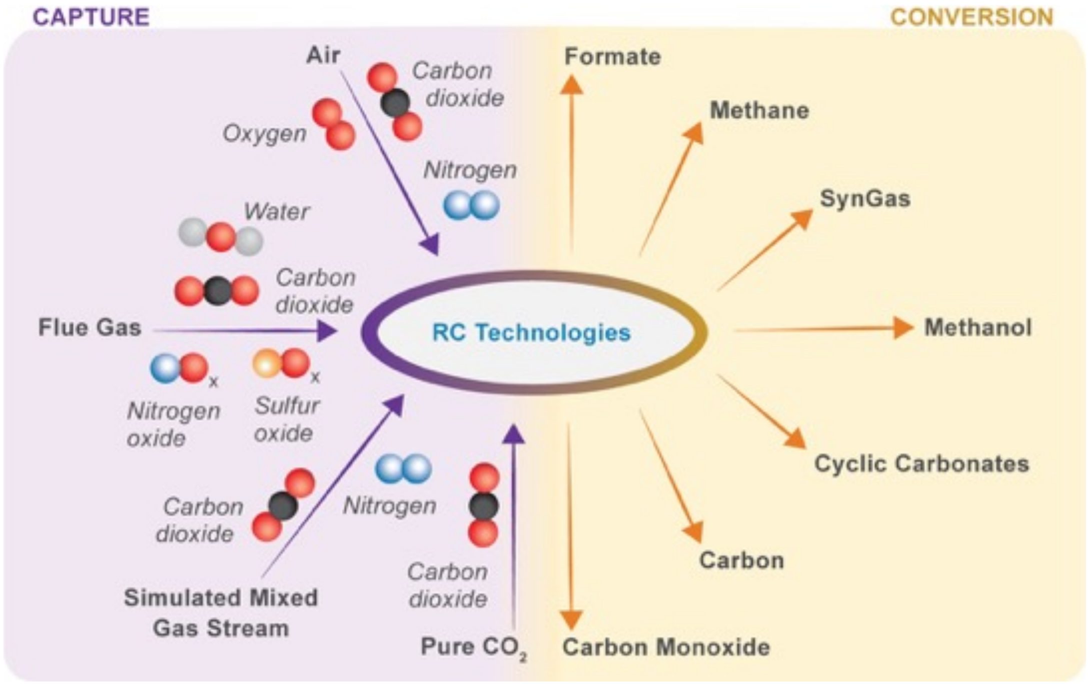

Figure 5.3 A schematic diagram showing the major gas sources and products produced by RC technologies.

5.5 Reactive Capture Process Considerations

While a full technoeconomic and lifecycle assessment for the different RC systems is outside the scope of this discussion, here we use operational temperature and pressure, parameters that can be readily gleaned from published reports, to provide indication of process complexity and ability to integrate readily with renewable energy sources for the various RC methods and strategies. We fully acknowledge that other parameters may be more important indicators of technological promise and to guide research. This highlights our message that the RC community will benefit greatly from early stage, systems level guidance on the most impactful performance metrics informed in part by the target source of CO_2. **Figure 5.4** compares the CO_2 uptake and conversion temperature and total system pressure for the various RC systems reported in the academic literature. Temperatures and pressures indicated in **Figure *5.4*** range from ambient to 900 °C and ambient to 8 MPa, respectively. In some cases, thermal and/or pressure swings are required for the complete capture and conversion sequence. These operational conditions have important implications for the development of the technologies, in everything from target CO_2 source, as described above, to target energy source. High pressure and temperature volumetric processes may be more operationally complex, more compatible with post combustion gas streams and may follow different scaling laws than more modular and lower temperature systems, *e.g.,* based upon electrolysis. Additionally, at high temperatures and pressures, materials of construction, and durability can be more costly and critical. Processes that require temperature/pressure swings may be less energy efficient overall than continuous, single condition systems. High temperature systems are less readily integrated with renewable electricity, or may target the use of waste heat or heat pumps for integration, while low temperature and biological systems are more readily integrated, requiring only electrical input for the conversion step and for mechanical agitation. Parameters that are not presented here, due to lack of information, but which may be equally or more important include: volumetric productivity, effects of intermittency on operation, single pass conversion, product purity, and process durability. Here we present a list of RC reporting parameters to guide the community:

Broadly, we find that electrochemical methods operate at low pressures but have a wide range of temperatures. For example, molten salt reactors are operated at significantly higher temperatures (typically beyond 450 °C) than bicarbonate electrolyzers. In terms of durability, the caustic environment can also be a problem for molten salt reactors and required to survive the conditions necessary. For the anode, the most stable material was found to be costly iridium, but cheaper alternatives such as nickel and tin oxide can be used.[7,55] In contrast, we found that amine and hydroxide-based RC systems operate at moderate temperatures, never exceeding 200 °C in order to protect the integrity of CO_2 capture materials (**Figure 5.4a**).

However, amine-based systems are typically operated at higher pressures as a result of the introduction of hydrogen gas as a secondary additive. Metal/metal oxide composites-based RC demonstrations operate at ambient pressure but at the highest temperatures of the thermal RC systems (300 to 730 °C). The composites remain in solid state during the reaction. The chosen materials for these RC systems must be able to operate and maintain stability at elevated temperatures, which places further limitations on material compatibility. In metal on oxide RC systems, the introduction of nanofeatures has helped improve the capture and release of CO_2 by lowering the reaction temperature required for these systems.[15,31] This could help the metal on oxide materials transition to a wider temperature option for capture and conversion.

Most polymer and MOF RC systems perform the capture and conversion at the same temperature under 150 °C. A few polymer RC systems utilize temperature swings, operating at a lower temperature for CO_2 capture and then ramping to a higher temperature for the conversion reaction to take place (**Figure 5.4a**), adding operational complexity and potentially reducing yields due to desorbing CO_2 during heating. Most polymer RC systems are held under higher pressures (pure CO_2) compared to the other RC systems (**Figure 5.4b)**, helping to suppress CO_2 desorption at elevated temperatures. In addition, both methanogenesis and acetogenesis based RC systems are operated at slightly elevated temperatures in a range from 30 to 60 °C, for CO_2 capture and conversion. This slightly elevated temperature is needed to maintain the productivity of the microbes. Microbes offer an exciting opportunity to utilize a catalyst which can regenerate itself through microbe growth. But the anaerobic, moderate pH and temperature conditions must be maintained to retain microbe viability.

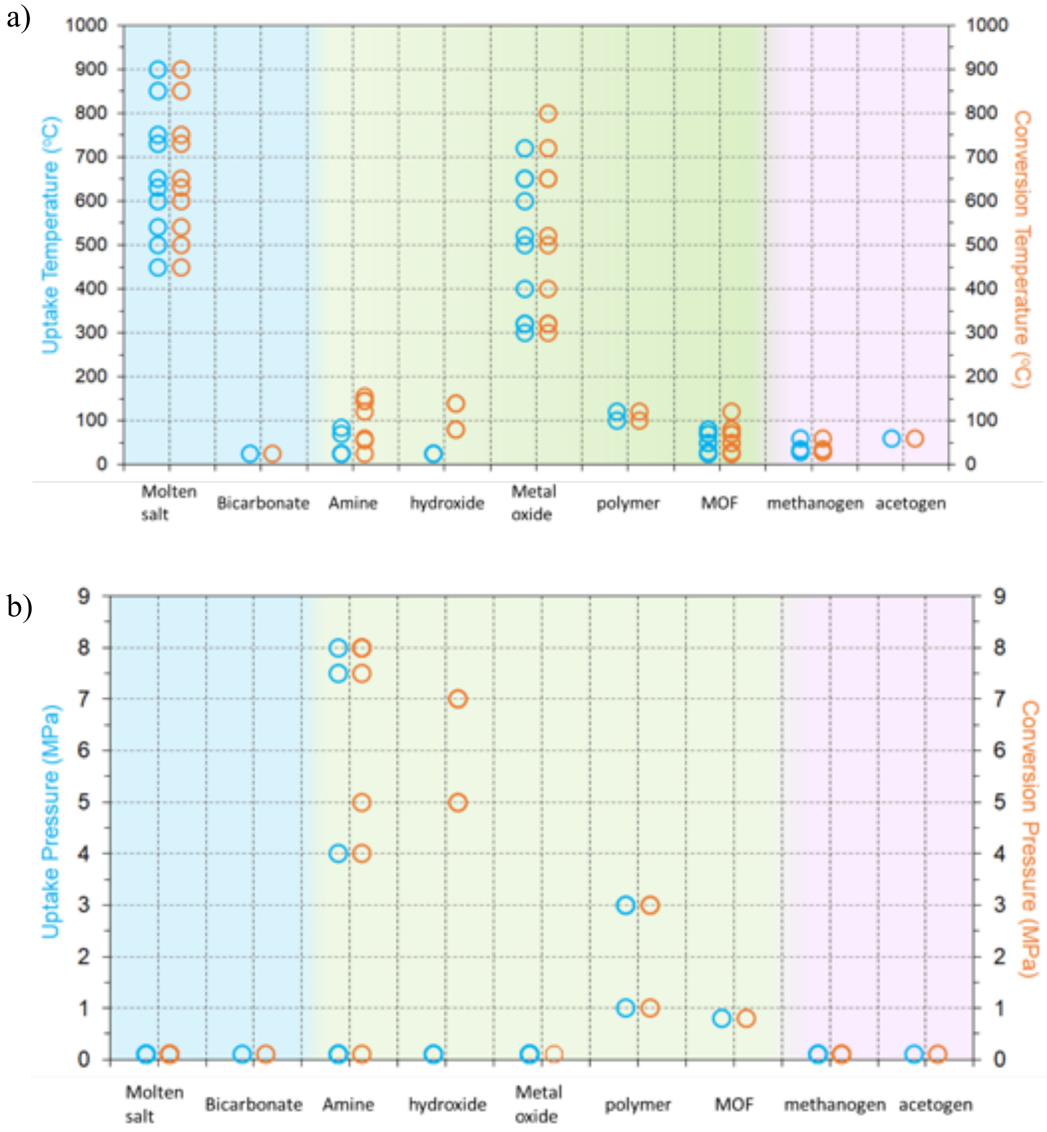

Figure 5.4 Plots to illustrate the (a) CO_2 uptake and conversion temperature; (b) Total pressure of CO_2 uptake and conversion of existing RC technologies. Blue and orange circles represent uptake and conversion, respectively.

5.6 Reactive Capture Process Parameters: co-reactants, rates, products, and other considerations

Most RC systems require co-reactants or additional reagents that are consumed in the process of conversion of captured CO_2 to desired products, impacting the economics and life cycle of carbon emissions from the process. Here we consider the commonly used reagents for RC systems and their corresponding products, product yields, and production rates (**Table *5.1***). The only RC systems examined in this discussion that do not require additional reagents by our definition are two electrochemical methods: molten salt reactors and bicarbonate electrolyzer.

The most common additive is hydrogen gas, which is used by the metal oxide, amine, and hydroxide reactors, in addition to methanogenesis, and acetogenesis. In these RC systems, hydrogen is introduced as a secondary gas or in the case of bio-methanogenesis generated *in situ* through water splitting. **Table *5.1*** shows the major products which are generated through the use of hydrogen, including methanol,[10,35] formate,[11,32,36] methane [14,15] and syngas [28]. Currently, the majority of H_2 is generated using fossil fuels.[56] For systems that rely on H_2 gas as a co-reactant the cost and energy associated with renewable hydrogen production, or emissions from conventional production must be accounted for in technoeconomic and lifecycle assessments. Similarly, polymer and MOF systems produce cyclic carbonates by catalyzing the reaction between the captured CO_2 and liquid epoxides with high conversion efficiencies.[57,58] However, epoxide production is energy intensive and could potentially offset the reduction in carbon emission benefit of the RC system. Additives that are used less frequently in RC systems are methane and ethane. Metal on oxide systems use methane and ethane to convert the captured CO_2 to syngas. It is important that these additives can be produced through a carbon neutral method, so they do not negate the goal of the RC systems. For example, hydrogen gas can be generated through water splitting or biomass gasification, while methane can be obtained from biogas, albeit hat significantly higher cost than natural gas.

Table 5.1 Summary of additional reagents required for CO_2 conversion of CO_2 in RC systems, and their corresponding product, product yields and production rate metrics.

RC Material	Experimental CO_2 Source	Co-Reactant	Product	Product Yields	Product Rate Metrics	Ref
Molten Salts	Mixed Gas (CO_2 and N_2)†	None	Structured Carbon	29-36%	CE: 78.5-89.7%	59
	Air	None	Structured Carbon	>80%	CoE: 100%	7
				-	CoE: 100%	51
	Pure CO_2	None	Structured Carbon	78%	-	6
				75-95 wt%	CE: >90%	60
				>80%	CE: 82%	61
				0.11g	FE: 100%	62
				-	CE:>70%	55
Bicarbonate	Pure CO_2	None	Carbon Monoxide	-	FE: 82%	9
Amines	Simulated Air	Hydrogen	Methanol	89%	TON: 96	13

				79%		12
	Pure CO_2	Hydrogen	Formate	95%	TON:7375	32
				37%	TON: 260	33
			Methanol	95%	TON: 208	13
				65%	TOF: 70 h^{-1}	12
				0.9 mmol	TON: 90	35
Hydroxides	Air	Hydrogen + Ethylene Glycol	Methanol	25-100%	-	10
		Hydrogen	Formate	73%	-	11
	Pure CO_2	Hydrogen + Ethylene Glycol	Methanol	100%	TON: 200	10
		Hydrogen	Formate	98%	TOF: 5420 h^{-1}	11
Polymers	Pure CO_2	Epoxide	Cyclic Carbonate	98.1%	TON: 167-201	16
				81.5%	-	17
				92%	-	18
				98%	-	19
				99%	-	20
				90%	TOF: 2888 h^{-1}	21
		Hydrogen	Formic Acid	54.1%	TON: 2254	54
MOFs	Pure CO_2	Epoxide	Cyclic Carbonate	>99%	-	23
				77.9%	TOF: 7.1 h^{-1}	24
				94%	-	25
		Terminal Alkynes	Propiolic acids	96.5%	-	37
	Mixed Gas (CO_2 and N_2)†	Epoxide	Cyclic Carbonate	86%	-	22

Metal on Oxides	Mixed Gas (CO_2 and N_2) and (CO_2, N_2, O_2 H_2O and air)†	Hydrogen	Methane	96%	TOF: 15000 h^{-1}	14
				85%	-	15
			Syngas	7.3 mmol per gram of catalyst	TOF: 0.78 s^{-1}	28
		Methane	Syngas	~ 9 mmol per gram of catalyst	ConE: 80%	63
		Ethane	Syngas	50%	ConE: 75%	26
Methanogens	Mixed Gas (CO_2 and N_2)†	Hydrogen	Methane	17653 mmol per liter of microbe/growth media per day	CCE: >90%	64
				-	ECE: 70%	65
				-	CoE: 80%	66
				-	ConE: 20%	67
	Pure CO_2	Hydrogen	Methane	1.4 L day^{-1}	CoE: >90%	38
				5.2 L m^{-2} day^{-1}	-	39
				65 L per m^2 catalyst per day	-	40
				129.32 mL day^{-1}	-	68
				-	ConE: 97.7%	69
Acetogens	Mixed Gas (CO_2 and N_2)†	Hydrogen	Acetate	154 µmol	-	42
	Pure CO_2	Hydrogen	Acetate	643 µmol	-	42
				180 mM	-	43
				60.8-78.2 µmol per liter substrate	-	44

				22.7 mmol per 100 mmol substrate	-	[45]
				9.8 mM	-	[46]
				76.9-99.8 mM	-	[47]
				49.9 mmol per 100 mmol substrate	-	[48]
				95.41 mmol per liter substrate	-	[49]
				94.73 mg day^{-1}	-	[68]

† Composition of different components depend on system; CE: current efficiency; CoE: Coulomb Efficiency; FE: Faradaic Efficiency; TON: Turn Over Number; TOF: Turn Over Frequency; ConE: Conversion Efficiency; CCE: Current Capture Efficiency; ECE: Electron Capture Efficiency

Current RC technologies have demonstrated the production of a wide range of carbon-containing products, from organic acids, single carbon gasses and liquids, gas mixtures such as syngas, and even solid carbon products. However, as shown in **Table *5.1***, there is also a correspondingly wide range of process metrics reported, making it extremely challenging to evaluate and compare technologies. As ‘Reactive Capture’ becomes a more mature field there is an urgent need for uniform standards, protocols and performance parameters for testing and reporting, driven not only by bottom-up understanding of needs for high selectivity/durability catalysts, sorbents, etc. but also from a top-down understanding of end-use. We propose the following as initial basic metrics for unified reporting across the discipline: 1) volumetric productivity (g/L/hr or g/cm^2/hr) will enable a comparison of process intensity, which ultimately informs reactor footprint and capital expense. 2) Single pass CO_2 conversion efficiency is a technology agnostic means of representing the carbon efficiency of the process. 3) Product purity is critical for assessing downstream energy usage and cost for producing the desired product at needed purity. 4) Productivity over time provides information on durability Importantly, our proposed metrics require testing on mixed gas streams. Unifying reporting metrics will make analysis and comparison of performance more straightforward for a more cohesive 'Reactive Capture' field.

5.7 Materials Challenges

To realize the full potential of RC systems, several technical challenges must be overcome. First, the low sorption selectivity of CO_2 over other gaseous species in air or flue gas at relevant temperature and pressure is problematic for most RC systems. The sorption selectivity of CO_2 over other gas components could be improved through the introduction of specific functional groups that have preferential CO_2 (chemi-)sorption or formation of intermediates, which can then be further utilized in the conversion process.

Second, the performance of RC systems can be affected by secondary components of the CO_2 source. For example, flue gas commonly contains NO_x, SO_x, CO, and H_2O, which can react with or irreversibly bind to sorption or catalytic sites.[70] Air contains a high concentration of O_2 and can contain varying amounts of H_2O, both of which can contribute to the degradation of certain materials. More rigorous testing is needed to determine the viability of RC systems in the presence of these components and determine if and when they must be removed from the reactant or product streams. A practically feasible RC system should not only have the capability to selectively capture and convert CO_2 over other gases, but also have highly stable sorption and conversion centers that are not poisoned or degraded by other components of the CO_2 source gas. The content of secondary components in the gas stream is dependent on when the contaminants are removed, prior to the RC system or from the final product stream.

Third, there are two facets to RC systems, the capture of CO_2 and the conversion to the desired products. In an ideal system, the best performance of one facet would not diminish the performance of the other. The CO_2 capture rate should closely match with the conversion rate. The capture and conversion sites should be in close proximity and CO_2 must not bind so tightly on the capturing materials that it prevents further conversion to products. Good compatibility between optimum uptake and conversion reaction conditions is critical to the success of any RC system.

5.8 Future Outlook

In this Discussion, we have highlighted the recent development of RC technologies. With such a diverse range of technologies, it is hopeful that they can be tailored to meet the needs of a diverse range of CO_2 gas sources and operation conditions (**Figure** *5.5*). Each major CO_2 point source has its own challenges to overcome. **Figure** ***5.5*** highlights characteristics which all RC technologies should have and characteristics which will be important for the RC technologies that target a specific CO_2 source. Direct air capture offers the greatest flexibility in the placement of the RC system. The system does not need to be placed at the CO_2 point source, but anywhere the product is needed, renewable energy is readily available, or where optimum performance can be attained. The RC materials face a selectivity challenge due to the low concentration of CO_2 in air compared to other components such as N_2 or O_2. The higher concentration of CO_2 in flue gas makes it a slightly easier target for RC technologies. However, the RC technology must be able to withstand the high temperature and potentially caustic impurities (*e.g.,* O_2, NO_x SO_x) along with humidity. Biogas has the highest CO_2 content (approximately 40% depending on source), but there are still compatibility challenges due to small scale, variable CO_2 streams with H_2S contamination. Finally, it is essential to bring RC technologies to a practically feasible level in order to make an impact on circular carbon economy. A comprehensive techno-economic analysis on different RC processes should be performed to gain a quantitative understanding of the benefits and risks of these technologies compared to separate capture and conversion systems. A life cycle analysis for the specific RC systems can give insight on the overall environmental impact for cradle to grave operation of the RC technology.

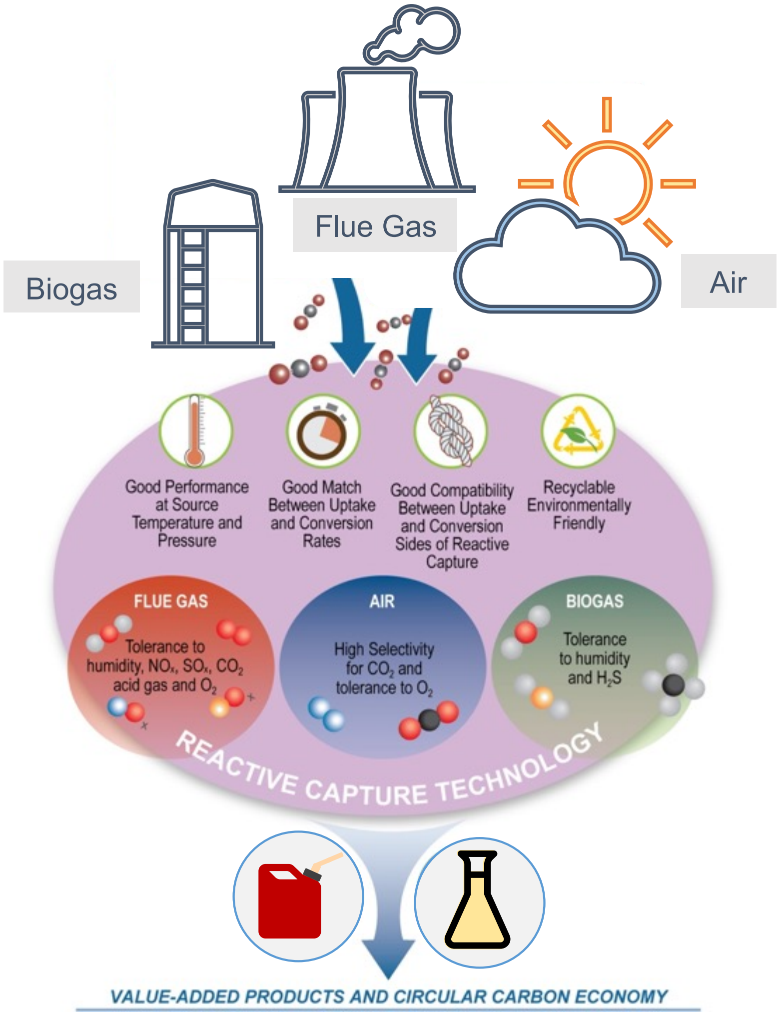

Figure 5.5 A schematic illustration of an ideal RC systems.

5.9 References

1. P.R. Shukla, J.S., E. Calvo Buendia, V. masson-Delmotte, H.-O. Pörtner, D. C. Roberts, P. Zhai, R. Slade, S. Connors, R. van Diemen, M. ferrat, E. Haughey,

S. Luz, S. Neogi, M. Pathak, J. Petzold, J. Portugal pereira, P. Vyas, E. Huntley, K. Kissick, M. Belkacemi, J. Miley, (eds.) 2019; **IPCC, 2019: Climate Change adn Land: an IPCC special report on cliate change, desertification, land degradation, sustaibable land management, food security, and greenhouse gas fluexes in terrestrial ecosystems**. (In press).

2. Lindsey, R. 2020; **Climate Change: Atmospheric Carbon Dioxide**. (NOAA Climate.gov).
3. Kätelhön, A., Meys, R., Deutz, S., Suh, S., and Bardow, A. **Climate change mitigation potential of carbon capture and utilization in the chemical industry**. Proceedings of the National Academy of Sciences. 2019; **116:** 11187.
4. John Gale, J.B., Zhenlin Chen, Amit Garg, Dario Gomez, Hans-Holger Rogner, Dale Simbeck, Robert WilliamsFerenc Toth, Detlef van Vuuren 2005; **Sources of CO_2**. J.F.H. Ismail El Gizouli, ed. (IPCC).
5. Grim, R.G., Huang, Z., Guarnieri, M.T., Ferrell, J.R., Tao, L., and Schaidle, J.A. **Transforming the carbon economy: challenges and opportunities in the convergence of low-cost electricity and reductive CO2 utilization**. Energy & Environmental Science. 2020; **13:** 472-494.
6. Hu, L., Song, Y., Ge, J., Zhu, J., and Jiao, S. **Capture and electrochemical conversion of CO_2 to ultrathin graphite sheets in $CaCl_2$-based melts**. Journal of Materials Chemistry A. 2015; **3:** 21211-21218.

7. Ren, J., Li, F.-F., Lau, J., González-Urbina, L., and Licht, S. **One-Pot Synthesis of Carbon Nanofibers from CO_2**. Nano Letters. 2015; **15:** 6142-6148.

8. Keith, D.W., Holmes, G., St. Angelo, D., and Heidel, K. **A Process for Capturing CO_2 from the Atmosphere**. Joule. 2018; **2:** 1573-1594.

9. Lees, E.W., Goldman, M., Fink, A.G., Dvorak, D.J., Salvatore, D.A., Zhang, Z., Loo, N.W.X., and Berlinguette, C.P. **Electrodes Designed for Converting Bicarbonate into CO**. ACS Energy Letters. 2020; **5:** 2165-2173.

10. Sen, R., Goeppert, A., Kar, S., and Prakash, G.K.S. **Hydroxide Based Integrated CO_2 Capture from Air and Conversion to Methanol**. Journal of the American Chemical Society. 2020; **142:** 4544-4549.

11. Kar, S., Goeppert, A., Galvan, V., Chowdhury, R., Olah, J., and Prakash, G.K.S. **A Carbon-Neutral CO_2 Capture, Conversion, and Utilization Cycle with Low-Temperature Regeneration of Sodium Hydroxide**. Journal of the American Chemical Society. 2018; **140:** 16873-16876.

12. Kothandaraman, J., Goeppert, A., Czaun, M., Olah, G.A., and Prakash, G.K.S. **Conversion of CO_2 from Air into Methanol Using a Polyamine and a Homogeneous Ruthenium Catalyst**. Journal of the American Chemical Society. 2016; **138:** 778-781.

13. Kar, S., Sen, R., Goeppert, A., and Prakash, G.K.S. **Integrative CO_2 Capture and Hydrogenation to Methanol with Reusable Catalyst and Amine:**

Toward a Carbon Neutral Methanol Economy. Journal of the American Chemical Society. 2018; **140:** 1580-1583.

14. Garbarino, G., Bellotti, D., Riani, P., Magistri, L., and Busca, G. **Methanation of carbon dioxide on Ru/Al_2O_3 and Ni/Al_2O_3 catalysts at atmospheric pressure: Catalysts activation, behaviour and stability**. International Journal of Hydrogen Energy. 2015; **40:** 9171-9182.

15. Duyar, M.S., Treviño, M.A.A., and Farrauto, R.J. **Dual function materials for CO_2 capture and conversion using renewable H_2**. Applied Catalysis B: Environmental. 2015; **168-169:** 370-376.

16. Xie, Y., Wang, T.-T., Liu, X.-H., Zou, K., and Deng, W.-Q. **Capture and conversion of CO_2 at ambient conditions by a conjugated microporous polymer**. Nature Communications. 2013; **4:** 1960.

17. Wang, J., Sng, W., Yi, G., and Zhang, Y. **Imidazolium salt-modified porous hypercrosslinked polymers for synergistic CO_2 capture and conversion**. Chemical Communications. 2015; **51:** 12076-12079.

18. Talapaneni, S.N., Buyukcakir, O., Je, S.H., Srinivasan, S., Seo, Y., Polychronopoulou, K., and Coskun, A. **Nanoporous Polymers Incorporating Sterically Confined N-Heterocyclic Carbenes for Simultaneous CO_2 Capture and Conversion at Ambient Pressure**. Chemistry of Materials. 2015; **27:** 6818-6826.

19. Buyukcakir, O., Je, S.H., Choi, D.S., Talapaneni, S.N., Seo, Y., Jung, Y., Polychronopoulou, K., and Coskun, A. **Porous cationic polymers: the impact**

of counteranions and charges on CO2 capture and conversion. Chemical Communications. 2016; **52:** 934-937.

20. Buyukcakir, O., Je, S.H., Talapaneni, S.N., Kim, D., and Coskun, A. **Charged Covalent Triazine Frameworks for CO_2 Capture and Conversion**. ACS Applied Materials & Interfaces. 2017; **9:** 7209-7216.

21. Ji, G., Yang, Z., Zhang, H., Zhao, Y., Yu, B., Ma, Z., and Liu, Z. **Hierarchically Mesoporous o-Hydroxyazobenzene Polymers: Synthesis and Their Applications in CO_2 Capture and Conversion**. Angewandte Chemie International Edition. 2016; **55:** 9685-9689.

22. Liang, L., Liu, C., Jiang, F., Chen, Q., Zhang, L., Xue, H., Jiang, H.-L., Qian, J., Yuan, D., and Hong, M. **Carbon dioxide capture and conversion by an acid-base resistant metal-organic framework**. Nature Communications. 2017; **8:** 1233.

23. Zhang, G., Wei, G., Liu, Z., Oliver, S.R.J., and Fei, H. **A Robust Sulfonate-Based Metal–Organic Framework with Permanent Porosity for Efficient CO_2 Capture and Conversion**. Chemistry of Materials. 2016; **28:** 6276-6281.

24. Liu, L., Wang, S.-M., Han, Z.-B., Ding, M., Yuan, D.-Q., and Jiang, H.-L. **Exceptionally Robust In-Based Metal–Organic Framework for Highly Efficient Carbon Dioxide Capture and Conversion**. Inorganic Chemistry. 2016; **55:** 3558-3565.

25. Ding, M., and Jiang, H.-L. **Incorporation of Imidazolium-Based Poly(ionic liquid)s into a Metal–Organic Framework for CO_2 Capture and Conversion**. ACS Catalysis. 2018; **8:** 3194-3201.

26. Al-Mamoori, A., Rownaghi, A.A., and Rezaei, F. **Combined Capture and Utilization of CO_2 for Syngas Production over Dual-Function Materials**. ACS Sustainable Chemistry & Engineering. 2018; **6:** 13551-13561.

27. Kim, S.M., Abdala, P.M., Broda, M., Hosseini, D., Copéret, C., and Müller, C. **Integrated CO_2 Capture and Conversion as an Efficient Process for Fuels from Greenhouse Gases**. ACS Catalysis. 2018; **8:** 2815-2823.

28. Sun, H., Wang, J., Zhao, J., Shen, B., Shi, J., Huang, J., and Wu, C. **Dual functional catalytic materials of Ni over Ce-modified CaO sorbents for integrated CO_2 capture and conversion**. Applied Catalysis B: Environmental. 2019; **244:** 63-75.

29. Bermejo-López, A., Pereda-Ayo, B., González-Marcos, J.A., and González-Velasco, J.R. **Ni loading effects on dual function materials for capture and in-situ conversion of CO_2 to CH_4 using CaO or Na_2CO_3**. Journal of CO_2 Utilization. 2019; **34:** 576-587.

30. Arellano-Treviño, M.A., He, Z., Libby, M.C., and Farrauto, R.J. **Catalysts and adsorbents for CO_2 capture and conversion with dual function materials: Limitations of Ni-containing DFMs for flue gas applications**. Journal of CO_2 Utilization. 2019; **31:** 143-151.

31. Omodolor, I.S., Otor, H.O., Andonegui, J.A., Allen, B.J., and Alba-Rubio, A.C. **Dual-Function Materials for CO_2 Capture and Conversion: A Review**. Industrial & Engineering Chemistry Research. 2020; **59:** 17612-17631.

32. Kothandaraman, J., Goeppert, A., Czaun, M., Olah, G.A., and Surya Prakash, G.K. **CO_2 capture by amines in aqueous media and its subsequent conversion to formate with reusable ruthenium and iron catalysts**. Green Chemistry. 2016; **18:** 5831-5838.

33. Li, Y.-N., He, L.-N., Liu, A.-H., Lang, X.-D., Yang, Z.-Z., Yu, B., and Luan, C.-R. **In situ hydrogenation of captured CO_2 to formate with polyethyleneimine and Rh/monophosphine system**. Green Chemistry. 2013; **15:** 2825-2829.

34. Kothandaraman, J., and Heldebrant, D.J. **Towards environmentally benign capture and conversion: heterogeneous metal catalyzed CO_2 hydrogenation in CO_2 capture solvents**. Green Chemistry. 2020; **22:** 828-834.

35. Kar, S., Goeppert, A., and Prakash, G.K.S. **Combined CO_2 Capture and Hydrogenation to Methanol: Amine Immobilization Enables Easy Recycling of Active Elements**. ChemSusChem. 2019; **12:** 3172-3177.

36. McNamara, N.D., and Hicks, J.C. **CO_2 Capture and Conversion with a Multifunctional Polyethyleneimine-Tethered Iminophosphine Iridium Catalyst/Adsorbent**. ChemSusChem. 2014; **7:** 1114-1124.

37. Liu, X.-H., Ma, J.-G., Niu, Z., Yang, G.-M., and Cheng, P. **An Efficient Nanoscale Heterogeneous Catalyst for the Capture and Conversion of Carbon Dioxide at Ambient Pressure**. Angewandte Chemie International Edition. 2015; **54:** 988-991.

38. Kracke, F., Deutzmann, J.S., Gu, W., and Spormann, A.M. **In situ electrochemical H_2 production for efficient and stable power-to-gas electromethanogenesis**. Green Chemistry. 2020; **22:** 6194-6203.

39. van Eerten-Jansen, M.C.A.A., Jansen, N.C., Plugge, C.M., de Wilde, V., Buisman, C.J.N., and ter Heijne, A. **Analysis of the mechanisms of bioelectrochemical methane production by mixed cultures**. Journal of Chemical Technology & Biotechnology. 2015; **90:** 963-970.

40. Liu, D., Roca-Puigros, M., Geppert, F., Caizán-Juanarena, L., Na Ayudthaya, S.P., Buisman, C., and ter Heijne, A. **Granular Carbon-Based Electrodes as Cathodes in Methane-Producing Bioelectrochemical Systems**. Frontiers in Bioengineering and Biotechnology. 2018; **6**.

41. Schiel-Bengelsdorf, B., and Dürre, P. **Pathway engineering and synthetic biology using acetogens**. FEBS Letters. 2012; **586:** 2191-2198.

42. Sleat, R., Mah, R.A., and Robinson, R. **Acetoanaerobium noterae gen. nov., sp. nov.: an Anaerobic Bacterium That Forms Acetate from H_2 and CO_2**. International Journal of Systematic and Evolutionary Microbiology. 1985; **35:** 10-15.

43. Balch, W.E.S., S. Tanner, Ralph S. Wolfe, R. S. **Acetobacterium, a New Genus of Hydrogen-Oxidizing, Carbon Dioxide-Reducing, Anaerobic Bacteria**. International Journal of Systematic and Evolutionary Microbiology. 1977; **27:** 355-361.

44. Wiegel, J., Braun, M., and Gottschalk, G. **Clostridium thermoautotrophicum species novum, a thermophile producing acetate from molecular hydrogen and carbon dioxide**. Current Microbiology. 1981; **5:** 255-260.

45. Kane, M.D., and Breznak, J.A. **Acetonema longum gen.nov.sp.nov., an H_2/CO_2 acetogenic bacterium from the termite, Pterotermes occidentis**. Archives of Microbiology. 1991; **156:** 91-98.

46. Küsel, K., Karnholz, A., Trinkwalter, T., Devereux, R., Acker, G., and Drake, H.L. **Physiological Ecology of *Clostridium glycolicum* RD-1, an Aerotolerant Acetogen Isolated from Sea Grass Roots**. Applied and Environmental Microbiology. 2001; **67:** 4734.

47. Greening, R.C., and Leedle, J.A.Z. **Enrichment and isolation of Acetitomaculum ruminis, gen. nov., sp. nov.: acetogenic bacteria from the bovine rumen**. Archives of Microbiology. 1989; **151:** 399-406.

48. Bernalier, A., Willems, A., Leclerc, M., Rochet, V., and Collins, M.D. **Ruminococcus hydrogenotrophicus sp. nov., a new H_2/CO_2-utilizing acetogenic bacterium isolated from human feces**. Archives of Microbiology. 1996; **166:** 176-183.

49. Xu, S., Fu, B., Zhang, L., and Liu, H. **Bioconversion of H2/CO2 by acetogen enriched cultures for acetate and ethanol production: the impact of pH**. World Journal of Microbiology and Biotechnology. 2015; **31:** 941-950.

50. Cheng, S., Xing, D., Call, D.F., and Logan, B.E. **Direct Biological Conversion of Electrical Current into Methane by Electromethanogenesis**. Environmental Science & Technology. 2009; **43:** 3953-3958.

51. Douglas, A., Muralidharan, N., Carter, R., and Pint, C.L. **Sustainable Capture and Conversion of Carbon Dioxide into Valuable Multiwalled Carbon Nanotubes Using Metal Scrap Materials**. ACS Sustainable Chemistry & Engineering. 2017; **5:** 7104-7110.

52. Wang, S., Schrunk, E.T., Mahajan, H., Farrauto, and Robert, J. **The Role of Ruthenium in CO2 Capture and Catalytic Conversion to Fuel by Dual Function Materials (DFM)**. Catalysts. 2017; **7**.

53. Lee, J.H., Lee, H.J., Lim, S.Y., Kim, B.G., and Choi, J.W. **Combined CO2-philicity and Ordered Mesoporosity for Highly Selective CO2 Capture at High Temperatures**. Journal of the American Chemical Society. 2015; **137:** 7210-7216.

54. Yang, Z.-Z., Zhang, H., Yu, B., Zhao, Y., Ji, G., and Liu, Z. **A Tröger's base-derived microporous organic polymer: design and applications in CO_2/H_2 capture and hydrogenation of CO_2 to formic acid**. Chemical Communications. 2015; **51:** 1271-1274.

55. Yin, H., Mao, X., Tang, D., Xiao, W., Xing, L., Zhu, H., Wang, D., and Sadoway, D.R. **Capture and electrochemical conversion of CO_2 to value-added carbon and oxygen by molten salt electrolysis**. Energy & Environmental Science. 2013; **6:** 1538-1545.

56. Dincer, I., and Acar, C. **Review and evaluation of hydrogen production methods for better sustainability**. International Journal of Hydrogen Energy. 2015; **40:** 11094-11111.

57. Qiao, W.-Z., Xu, H., Cheng, P., and Zhao, B. **3d-4f Heterometal–Organic Frameworks for Efficient Capture and Conversion of CO_2**. Crystal Growth & Design. 2017; **17:** 3128-3133.

58. Darensbourg, D.J., Mackiewicz, R.M., Phelps, A.L., and Billodeaux, D.R. **Copolymerization of CO_2 and Epoxides Catalyzed by Metal Salen Complexes**. Accounts of Chemical Research. 2004; **37:** 836-844.

59. Otake, K., Kinoshita, H., Kikuchi, T., and Suzuki, R.O. **CO_2 gas decomposition to carbon by electro-reduction in molten salts**. Electrochimica Acta. 2013; **100:** 293-299.

60. Ijije, H.V., Lawrence, R.C., and Chen, G.Z. **Carbon electrodeposition in molten salts: electrode reactions and applications**. RSC Advances. 2014; **4:** 35808-35817.

61. Wu, H., Li, Z., Ji, D., Liu, Y., Li, L., Yuan, D., Zhang, Z., Ren, J., Lefler, M., Wang, B., et al. **One-pot synthesis of nanostructured carbon materials from**

carbon dioxide via electrolysis in molten carbonate salts. Carbon. 2016; **106:** 208-217.

62. Ren, J., Lau, J., Lefler, M., and Licht, S. **The Minimum Electrolytic Energy Needed To Convert Carbon Dioxide to Carbon by Electrolysis in Carbonate Melts**. The Journal of Physical Chemistry C. 2015; **119:** 23342-23349.

63. Tian, S., Yan, F., Zhang, Z., and Jiang, J. **Calcium-looping reforming of methane realizes in situ CO_2 utilization with improved energy efficiency**. Science Advances. 2019; **5:** eaav5077.

64. Fu, Q., Kuramochi, Y., Fukushima, N., Maeda, H., Sato, K., and Kobayashi, H. **Bioelectrochemical Analyses of the Development of a Thermophilic Biocathode Catalyzing Electromethanogenesis**. Environmental Science & Technology. 2015; **49:** 1225-1232.

65. Kobayashi, H., Nagashima, A., Kouyama, M., Fu, Q., Ikarashi, M., Maeda, H., and Sato, K. **High-pressure thermophilic electromethanogenic system producing methane at 5 MPa, 55°C**. Journal of Bioscience and Bioengineering. 2017; **124:** 327-332.

66. Beese-Vasbender, P.F., Grote, J.-P., Garrelfs, J., Stratmann, M., and Mayrhofer, K.J.J. **Selective microbial electrosynthesis of methane by a pure culture of a marine lithoautotrophic archaeon**. Bioelectrochemistry. 2015; **102:** 50-55.

67. Hara, M., Onaka, Y., Kobayashi, H., Fu, Q., Kawaguchi, H., Vilcaez, J., and Sato, K. **Mechanism of Electromethanogenic Reduction of CO_2 by a Thermophilic Methanogen**. Energy Procedia. 2013; **37:** 7021-7028.

68. Jiang, Y., Su, M., Zhang, Y., Zhan, G., Tao, Y., and Li, D. **Bioelectrochemical systems for simultaneously production of methane and acetate from carbon dioxide at relatively high rate**. International Journal of Hydrogen Energy. 2013; **38:** 3497-3502.

69. Baek, G., Kim, J., Lee, S., and Lee, C. **Development of biocathode during repeated cycles of bioelectrochemical conversion of carbon dioxide to methane**. Bioresource Technology. 2017; **241:** 1201-1207.

70. Last, G.V.S., Mary T 2011; **Identification and Selection of Major Carbon Dioxide Stream Compositions**. (Pacific Northwest National Lab (PNNL)).